UNIVERSIDADE DE BRASÍLIA – UNB

CAMPUS UNB GAMA: FACULDADE DE CIÊNCIAS E TECNOLOGIA EM ENGENHARIA

PROGRAMA DE PÓS-GRADUAÇÃO EM ENGENHARIA BIOMÉDICA

3D BIOPRINTING AND PHOTOACTIVATED NANOEMULSIONS IN BIOENGINEERING: APPLICATIONS IN DIABETES AND ONCOLOGY

LUCAS MEYER SYLLOS

ADVISOR: DR. MARCELLA LEMOS BRETTAS CARNEIRO

CO-ADVISOR: DR. HALIMA ALEM-MARCHAND

UNIVERSIDADE DE BRASÍLIA – UNB

CAMPUS UNB GAMA: FACULDADE DE CIÊNCIAS E TECNOLOGIA EM ENGENHARIA

Programa de Pós-Graduação em ENGENHARIA BIOMÉDICA

3D BIOPRINTING AND PHOTOACTIVATED NANOEMULSIONS IN BIOENGINEERING: APPLICATIONS IN DIABETES AND ONCOLOGY

LUCAS MEYER SYLLOS

ADVISOR: MARCELLA LEMOS BRETAS CARNEIRO

CO-ADVISOR: DR. HALIMA ALEM-MARCHAND

MASTER'S DISSERTATION IN

BIOMEDICAL ENGINEERING

PUBLISHED: 205A/2025

BRASÍLIA/DF, AUGUST 2025

UNIVERSIDADE DE BRASÍLIA - UNB
CAMPUS UNB GAMA: FACULDADE DE CIÊNCIAS E TECNOLOGIA EM ENGENHARIA
PROGRAMA DE PÓS-GRADUAÇÃO

3D BIOPRINTING AND PHOTOACTIVATED NANOEMULSIONS IN BIOENGINEERING: APPLICATIONS IN DIABETES AND ONCOLOGY

LUCAS MEYER SYLLOS

MASTER THESIS SUBMITTED TO THE BIOMEDICAL ENGINEERING GRADUATE PROGRAM, AS A PARTIAL FULFILLMENT OF THE REQUIREMENTS FOR THE DEGREE OF MASTER IN BIOMEDICAL ENGINEERING

MEMBERS COMITEE:

DR. MARCELLA LEMOS BRETAS CARNEIRO
(ADVISOR)

DR. FÁBIO VIEGAS CAIXETA
(INTERNAL EXAMINER)

DR. GLÉCIA VIRGOLINA DA SILVA LUZ
(INTERNAL EXAMINER)

DR. FILLIPE VIEIRA ROCHA
(EXTERNAL EXAMINER)

BRASÍLIA/DF, AUGUST DE 2025

CATALOG CARD

SYLLOS, LUCAS

3D Bioprinting and Photoactivated Nanoemulsions in Bioengineering: Applications in Diabetes and Oncology / Lucas Meyer Syllos; Advisor Dr Marcella Lemos Brettas Carneiro; Co-Advisor Dr Halima Alem-Marchand; Brasília, 2025. 96p.

Master's Dissertation in Biomedical Engineering, Campus UnB Gama: Faculty of Sciences and Technology in Engineering, Graduate Program in Biomedical Engineering.

1. Wound Dressings	2. Phototherapy
3. 3D Bioprinting	4. Translational Science
I. FCTE/UnB	II. Title

REFERENCE

Syllos, Lucas (2025). 3D Bioprinting and Photoactivated Nanoemulsions in Bioengineering: Applications in Diabetes and Oncology. Master's Dissertation in Biomedical Engineering, Published 08/2025, Campus UnB Gama: Faculty of Sciences and Technology in Engineering, University of Brasília, Brasília, DF, 83p.

COPYRIGH

241106793@unb.br

Brasília, DF – Brasil

Acknowledgments

First and foremost, I would like to thank my family: my parents, Nilson de Mello Syllos and Danielle Aparecida Meyer, for always supporting me, encouraging me to pursue my goals, and believing in my abilities; and my sister, Ana Luisa Meyer Syllos, the most important person on earth to me—you are my foundation, and I will continue to give you more reasons to be proud.

I am also deeply grateful to my advisors: Dr. Marcella Lemos Brettas Carneiro, for giving me my very first opportunity in the world of research, being an incredibly humane, sensitive, and determined mentor; and Dr. Halima Alem-Marchand, for trusting me and offering me the chance to discover the world, helping to strengthen my love for science. You are my role models, and I will strive to make you proud.

I owe eternal gratitude to Dr. Suélia de Siqueira Rodrigues Fleury Rosa, whose inspiring story, work, and adventurous spirit in science captivated me. Together with the entire LCBNano team, of which I had the honor and privilege to be a part, I would like to say that you shaped me as a researcher, molding both my character and my intellect into one guided by altruism, determination, and commitment to others.

I also extend my thanks to the esteemed members of my examination committee, Professors Fábio Viegas Caixeta and Fillipe Vieira Rocha, for kindly accepting to be part of this work as evaluators and for contributing to my journey in such an inspiring and thoughtful way.

I firmly believe that access to education—both formal and informal—is a right, not a privilege, and that no exam or process should strip us of this right. I believe in the power of public universities to provide intellectual freedom and social belonging to all, just as these rights have been granted to me. I believe that all those who, by birth or by choice, become Brazilians must be guaranteed the inheritance of technology, dignity, and the right to meaningful work and rest.

I am grateful for what has been given to me, for what I have achieved, and for what I will still accomplish. I am thankful for the strength to stand, and for that very reason I will remain standing, committed to the effort of building a popular future

ABSTRACT

This dissertation presents two complementary approaches in bioengineering aimed at advancing strategies in translational science applied to complex pathologies that share critical features of dysregulated immune responses and persistent inflammation: pancreatic ductal adenocarcinoma (PDAC) and diabetic foot ulcers (DFUs). PDAC remains one of the deadliest cancers globally, with limited treatment efficacy, while DFUs are among the most debilitating complications of diabetes, often leading to amputations and high costs for healthcare systems.
To address the need for more predictive models and effective treatments, we developed (i) a reproducible 3D bioprinted triculture model of PDAC, and (ii) photoactivated nanoemulsions containing curcumin and annatto oil for wound therapy. The PDAC model incorporated a triculture composed of human pancreatic cancer epithelial cells (PANC-1), fibroblasts (MeWo), and macrophages (THP-1) differentiated with Phorbol 12-myristate 13-acetate (PMA) in a gelatin–alginate-based bioink, using extrusion-based 3D bioprinting. Cell viability was assessed over a five-day period through live/dead staining, confocal microscopy, and quantitative image analysis using ImageJ software. The construct exhibited cell aggregation and sustained viability, representing a promising candidate for future integration into dynamic systems such as organ-on-a-chip (OOC) platforms. In addition, nanoemulsions containing annatto oil, sunflower oil, Cremophor® RH 40, and curcumin were tested on RAW 264.7 murine macrophages. Cytotoxicity was evaluated using the colorimetric MTT assay; nitric oxide levels were quantified using the Griess assay; and Interleukin 10 (IL-10) and Tumor Necrosis Factor alpha (TNF-α) were quantified using an Enzyme-Linked Immunosorbent Assay (ELISA). After irradiation with blue Light-Emitting Diode (LED) light, several formulations—especially those combining curcumin or annatto oil—significantly modulated inflammatory mediators TNF-α, IL-10, and nitric oxide. An increase in IL-10 release and a decrease in TNF-α and nitric oxide production were observed, demonstrating that the applied therapy plays an important role in inflammation reduction. Altogether, these findings highlight the potential of integrated cellular models and photoresponsive nanomaterials for advancing personalized therapeutic platforms and improving the preclinical assessment of complex diseases.

Keywords: translational research; biomedical technologies; biofabrication; lab-on-a-chip system; wound healing; immunomodulation; phototherapy; phytotherapeutics; tumor.

BIOIMPRESSÃO 3D E NANOEMULSÕES FOTOATIVADAS EM BIOENGENHARIA:

APLICAÇÕES EM DIABETES E ONCOLOGIA

RESUMO

Esta dissertação apresenta duas abordagens complementares em bioengenharia voltadas para o avanço de estratégias em ciência translacional aplicadas a patologias complexas que compartilham características críticas de respostas imunes desreguladas e inflamação persistente: o adenocarcinoma ductal pancreático (PDAC) e as úlceras do pé diabético (UPD). O PDAC continua sendo um dos cânceres mais letais globalmente, com eficácia limitada dos tratamentos, enquanto as UPDs estão entre as complicações mais debilitantes do diabetes, frequentemente levando a amputações e altos custos para os sistemas de saúde. Para atender à necessidade de modelos mais preditivos e tratamentos eficazes, desenvolvemos (i) um modelo tricelular de PDAC bioimpresso em 3D, reprodutível, e (ii) nanoemulsões fotoativadas contendo curcumina e óleo de urucum para terapia de feridas. O modelo de PDAC incorporou uma tricultura composta por células epiteliais humanas de câncer pancreático (PANC-1), fibroblastos (MeWo) e macrófagos (THP-1) diferenciados com Forbol 12-miristato 13-acetato (PMA) em uma biotinta à base de gelatina e alginato, utilizando bioimpressão 3D por extrusão. A viabilidade celular foi avaliada ao longo de cinco dias por coloração de células vivas/mortas, microscopia confocal e análise quantitativa de imagens utilizando o software ImageJ. O construto apresentou agregação celular e viabilidade sustentada, sendo um candidato promissor para futura integração em sistemas dinâmicos como plataformas organ-on-a-chip (OOC). Além disso, nanoemulsões contendo óleo de urucum, óleo de girassol, cremophor® RH 40 e curcumina foram testadas em macrófagos murinos da linhagem RAW 264.7. A citotoxicidade foi avaliada por meio do ensaio colorimétrico (MTT), os níveis de óxido nítrico foram quantificados pelo ensaio de Griess e a quantificação de Interleucina 10 (IL-10) e fator de necrose tumoral alfa (TNF-α) foi realizada por meio de Ensaio de Imunoabsorção Enzimática Ligado a uma Enzima (ELISA). Após irradiação com diodo emissor de luz (LED) azul, várias formulações — especialmente aquelas combinando curcumina ou óleo de urucum — modularam significativamente mediadores da inflamação TNF- α, IL-10 e óxido de nítrico. Observou-se um aumento da liberação de IL-10 e redução na produção de TNF-α e de óxido nítrico, demonstrando que a terapia adotada tem um importante papel na redução da inflamação. Em conjunto, esses achados ressaltam o potencial de modelos celulares integrados e de nanomateriais fotoresponsivos para o avanço de plataformas terapêuticas personalizadas e melhoria na avaliação pré-clínica de doenças complexas.

Palavras-chave: pesquisa translacional; tecnologias biomédicas; biofabricação; Sistema organ-on-a-chip; cicatrização de feridas; imunomodução; fototerapia; fitoterápicos; tumor.

SUMMARY

1 THEORETICAL BACKGROUND 1

1.1 Translational Science 1

1.2 Three-Dimensional (3D) Cell Cultures: The Next Step in Preclinical Development 2

1.3 3D Bioprinted Models 6

1.4 Organ-On-A-Chip 10

1.4.1 Concept 11

1.4.2 Components 11

1.4.3 Applications and Challenges 12

1.5 PDAC and DFU: Shared Features 14

1.5.1 DFU – Pathogenesis and Burden 15

1.5.2 PDAC – Pathogenesis and Microenvironment 17

1.6 Therapeutic Approaches and Emerging Technologies 18

1.6.1 RAPHA® System and Translational Strategies 19

1.7 Objectives 24

1.7.1 General 24

1.7.2 Specifics 24

2 PAPPER 1 26

2.1 Introduction 27

2.2 Materials and Methods 29

2.2.1 Nanoemulsions 29

2.2.2 Cell Culture 30

2.2.3 Cytotoxicity Assay (MTT) 30

2.2.4 Nitric Oxide Quantification (Griess Assay) 31

2.2.5 Inflammatory Stimulation and Cytokine Quantification (ELISA) 32

2.2.6 Statistical Analysis 33

2.3 Results 33

2.3.1 Nanoemulsion Characterization 33

2.3.2 Cytotoxicity Assay (MTT) 34

2.3.3 Nitric Oxide Quantification (Griess Assay) 38
2.3.4 Cytokine Profiling: TNF-α and IL-10 Quantification (ELISA) 47

4.4 Conclusion 57
4.5 References 58

3 PAPPER 2 63
3.1 Introduction 64
3.2 Materials and Methods 65
3.2.1 Reagents and Cell Lines 65
3.2.2 Cell Culture 65
3.2.3 THP-1 Differentiation 66
3.2.4 Tumor Mass Design 66
3.2.5 Bioink Preparation and Bioprinting 67
3.2.6 Cell Viability Assay 68

3.3 Results and Discussion 69
3.3.1 THP-1 Differentiation Efficiency 69
3.3.2 Bioprinting Performance 70
3.3.3 Cell Viability 71

3.4 Conclusion 73
3.5 References 73

4 PERSPECTIVES FOR TRANSLATIONAL INTEGRATION: FROM TUMOR MODELS TO CHRONIC INFLAMMATORY WOUNDS 76
5 CONCLUSION 77
6 REFERENCES 77

LIST OF TABLES

Table 1.1. Key Differences Between 2D and 3D Cell Culture Models. 5
Table 1.2. Types and description of the main hydrogel polymers used for 3D Bioprinting. 7
Table 1.3. Types and description of the main methods used for manufacturing 3D Bioprinting models. 9
Table 1.4. Comparative Overview of Bioink Formulations for Tumor Bioprinting and Potential Alternatives to Enhance Structural Stability in Macrophage-Containing Constructs 23
Table 2. Physicochemical parameters of nanoemulsions determined by DLS. 34
Table 3.1. Parameters for the bioprinting process. 67
Table 3.2. Parameters of confocal observation during the Live/Dead assay. 69

LIST OF FIGURES

Figure 1.1. Overview of the drug development process: (i) drug discovery, (ii) preclinical development, (iii) clinical development, and (iv) regulatory approval. Figure created by the author using Canva.com (July 2025). Source: the author. 1
Figure 1.2.1. 2D cell culture systems: Petri dish and a culture flask containing adherent and non-adherent cells in monolayer configuration. Schematic representation created by the author using Canva.com with support from ChatGPT (July 2025). Source: the author. 3
Figure 1.2.2. Multicellular spatial organization in 3D culture mimicking native tissue architecture. Distinct cell types are arranged in a multilayered configuration, forming a tissue-like structure that better replicates the in vivo environment. This setup enables realistic diffusion of nutrients, oxygen, and therapeutic agents, contributing to more accurate modeling of physiological and pathological processes. Schematic representation created by the author using Canva.com with support from ChatGPT (July 2025). Source: the author. 4
Figure 1.3. Key components of the 3D bioprinting process: (i) viable cells, (ii) CAD-based blueprint, and (iii) bioink containing biological materials and cells. These elements are combined using automated extrusion systems to fabricate physiologically relevant tissue constructs. Schematic representation created by the author using Canva.com (July 2025). Source: the author. 6
Figure 1.4. Schematic representation of the Organ-on-a-Chip (OoAC) concept. PDMS-based microfluidic chips are perfused with nutrient- and oxygen-rich culture medium, maintaining tissue-specific organ models such as lung, liver, and kidney. Metabolic waste and CO_2 are eliminated through controlled outflow channels. These platforms simulate physiological microenvironments in real time, enabling applications in disease modeling, pharmacokinetics, and drug toxicity screening. Schematic representation created by the author with support from ChatGPT (July 2025). Source: the author. 12
Figure 1.5.1. Comparative cytokine dynamics in normal wound healing versus diabetic foot ulcers (DFUs). Left: In physiological wound healing, balanced immune signaling favors resolution of inflammation, characterized by higher IL-10 levels and subsequent induction of TGF-β and VEGF, which promote angiogenesis and tissue repair, while downregulating iNOS, IL-6, IL-1β, and TNF-α. Right: In DFUs, chronic hyperglycemia sustains a pro-inflammatory state dominated by persistent TNF-α, IL-1β, IL-6, and iNOS activity, impairing angiogenesis and delaying wound closure. Schematic representation created by the author using Canva.com (July 2025). Source: the author . 16
Figure 1.6. Conceptual schematic of the proposed photoactivated therapeutic strategy: a nanoemulsion containing curcumin (a bioactive compound derived from *Curcuma longa*) and annatto oil (extracted from *Bixa orellana* seeds) is envisioned to be applied over a natural latex biofilm (NLB) and activated by blue LED irradiation. This platform is designed to promote anti-inflammatory effects and support tissue repair in chronic wounds such as diabetic foot ulcers. Schematic representation created by the author using Canva.com (July 2025). Source: the author. 21
Figure 2.1. Blue LED irradiation used in the project experiment. (A) Experimental setup for 96-well plate irradiation, with light source positioned 5 cm above the samples, delivering a 1-minute pulse of blue light (λ = 470 nm, fluence up to 14 J/cm (B) HTM® Fluence device employed as a photodynamic therapy platform for photoactivation of curcumin- and annatto-based nanoemulsions. The equipment was acquired specifically for in vitro and in vivo assays of the projects at the University of Brasília (UnB). Note: this equipment is not part of the original Rapha® system patented by UnB. 31
Figure 2.2. Cytotoxicity profile of nanoemulsions (NeC, NeOl, NeB) in RAW 264.7 macrophages. Cell viability was evaluated using the MTT assay after 24 h of treatment with increasing concentrations (0.2 to 9.8 μg/mL), adjusted for curcumin concentration. Data are expressed as mean

± standard deviation from three independent experiments performed in quadruplicate. The bar graph illustrates a dose-dependent decrease in viability for NeC and NeOl, while NeB maintained higher biocompatibility. 36
Figure 2.3 Cytotoxicity profile of the respective free components—curcumin (C), annatto oil (Ol), and sunflower oil (B)—in RAW 264.7 macrophages. Cell viability was evaluated using the MTT assay after 24 h of treatment with increasing concentrations (0.2 to 9.8 µg/mL), adjusted for curcumin concentration. Free curcumin showed the most significant reduction in viability, while sunflower oil preserved viability above 100% across all concentrations tested. 37
Figure 2.4. Effect of curcumin (C) and curcumin nanoemulsion (NeC) on nitrite (NO_2^-) production by RAW 264.7 macrophages under non-irradiated conditions. Data are presented as mean ± SD (n = 3). Statistical significance: *p < 0.05, **p < 0.005, ***p < 0.001, ****p < 0.0001; ns = not significant. 39
Figure 2.5. Effect of curcumin (C) and curcumin nanoemulsion (NeC) on nitrite (NO_2^-) production by RAW 264.7 macrophages under irradiated conditions. Data are presented as mean ± SD (n = 3). Statistical significance: *p < 0.05, **p < 0.005, ***p < 0.001, ****p < 0.0001; ns = not significant. 40
Figure 2.6. Effect of annatto oil (Ol) and annatto nanoemulsion (NeOl) on nitrite (NO_2^-) production by RAW 264.7 macrophages under non-irradiated conditions. Data are presented as mean ± SD (n = 3). Statistical significance: *p < 0.05, **p < 0.005, ***p < 0.001, ****p < 0.0001; ns = not significant. 41
Figure 2.7. Effect of annatto oil (Ol) and annatto nanoemulsion (NeOl) on nitrite (NO_2^-) production by RAW 264.7 macrophages under irradiated conditions. Data are presented as mean ± SD (n = 3). Statistical significance: *p < 0.05, **p < 0.005, ***p < 0.001, ****p < 0.0001; ns = not significant. 42
Figure 2.8. Cell viability (%) of RAW 264.7 macrophages treated with curcumin (C) or curcumin nanoemulsion (NeC), under irradiated and non-irradiated conditions. No significant cytotoxicity was observed between matched groups. Concentrations expressed in µg/mL of pure curcumin. Statistical analysis: two-way ANOVA followed by Sidak's multiple comparisons test (GraphPad Prism 8.0.1); p > 0.05. 45
Figure 2.9. Cell viability (%) of RAW 264.7 macrophages treated with annatto oil (Ol) or annatto nanoemulsion (NeOl), under irradiated and non-irradiated conditions. No significant cytotoxicity was observed between matched groups. Concentrations expressed in µg/mL of pure curcumin. Statistical analysis: two-way ANOVA followed by Sidak's multiple comparisons test (GraphPad Prism 8.0.1); p > 0.05. 46
Figure 2.10. TNF-α levels (pg/mL) in RAW 264.7 macrophages after 24 h of treatment with curcumin (C) or curcumin nanoemulsion (NeC), under non-irradiated conditions. Data are presented as mean ± SD (n = 3). Statistical analysis: one-way ANOVA followed by Tukey's post hoc test; ****p < 0.0001. 48
Figure 2.11. TNF-α levels (pg/mL) in RAW 264.7 macrophages after 24 h of treatment with curcumin (C) or curcumin nanoemulsion (NeC), under irradiated conditions. Data are presented as mean ± SD (n = 3). Statistical analysis: one-way ANOVA followed by Tukey's post hoc test; ****p < 0.0001. 49
Figure 2.12. TNF-α levels (pg/mL) in RAW 264.7 macrophages after 24 h of treatment with annatto oil (Ol) or annatto nanoemulsion (NeOl), under non-irradiated conditions. Data are presented as mean ± SD (n = 3). Statistical analysis: one-way ANOVA followed by Tukey's post hoc test; ****p < 0.0001. 50
Figure 2.13. TNF-α levels (pg/mL) in RAW 264.7 macrophages after 24 h of treatment with annatto oil (Ol) or annatto nanoemulsion (NeOl), under irradiated conditions. Data are presented as mean ± SD (n = 3). Statistical analysis: one-way ANOVA followed by Tukey's post hoc test; ****p < 0.0001. 51

Figure 2.14. IL-10 levels (pg/mL) in RAW 264.7 macrophages after 24 h of treatment with curcumin (C) or curcumin nanoemulsion (NeC), under non-irradiated conditions. Data are presented as mean ± SD (n = 3). Statistical analysis: one-way ANOVA followed by Tukey's post hoc test; ****p < 0.0001. 52
Figure 2.15. IL-10 levels (pg/mL) in RAW 264.7 macrophages after 24 h of treatment with curcumin (C) or curcumin nanoemulsion (NeC), under irradiated conditions. Data are presented as mean ± SD (n = 3). Statistical analysis: one-way ANOVA followed by Tukey's post hoc test; ****p < 0.0001. 53
Figure 2.16. IL-10 levels (pg/mL) in RAW 264.7 macrophages after 24 h of treatment with annatto oil (Ol) or annatto nanoemulsion (NeOl), under non-irradiated conditions. Data are presented as mean ± SD (n = 3). Statistical analysis: one-way ANOVA followed by Tukey's post hoc test; ****p < 0.0001..... 54
Figure 2.17. IL IL-10 levels (pg/mL) in RAW 264.7 macrophages after 24 h of treatment with annatto oil (Ol) or annatto nanoemulsion (NeOl), under irradiated conditions. Data are presented as mean ± SD (n = 3). Statistical analysis: one-way ANOVA followed by Tukey's post hoc test; ****p < 0.0001. 55
Figure 3.1. Schematic representation of the bioprinting process for the triculture tumor model. Cells were trypsinized and embedded in a 2% (w/v) sodium alginate + 15% (w/v) gelatin hydrogel to form the bioink. Cylindrical tumor constructs (6 mm diameter, 1.5 mm height) were then printed, crosslinked with 100 mM $CaCl_2$ for 10 minutes, supplemented with complete culture medium, and incubated at 37 °C in 5% CO_2 until further experiments. 68
Figure 3.2. Percentage of THP-1 cells differentiated into M0-like macrophages after 48 h of PMA stimulation across 10 replicates (mean ± SD). 70
Figure 3. Representative Live/Dead confocal microscopy images of 3D bioprinted triculture constructs from day 1 to day 5 of culture (green: live cells; red: dead cells), alongside quantitative analysis of cell viability (%), presented as mean ± SD (n = 4)..... 72

LIST OF NOMENCLATURE AND ABBREVIATIONS

PDAC	Pancreatic Ductal Adenocarcinoma
DFU	Diabetic Foot Ulcers
PANC-1	Human Pancreatic Cancer Epithelial Cells
MEWO	Cancer-Associated Fibroblasts
THP-1	Human Monocyte Leukemia-Derived Macrophages
PMA	Phorbol 12-Myristate 13-Acetate
OOC	Organ-On-A-Chip
RAW 264.7	RAW 264.7 Murine Macrophage Cell Line
IL-10	Interleukin 10
TNF-α	Tumor Necrosis Factor Alpha
ELISA	Enzyme-Linked Immunosorbent Assay
LED	Light-Emitting Diode
2D	Two-Dimensional
3D	Three-Dimensional
ECM	Extracellular Matrix
TGF	Transforming Growth Factors
FGF	Fibroblast Growth Factors
PEG	Poly(Ethylene Glycol)
PLG	Poly-L-Glutamate
PNIPAM	Poly(N-Isopropylacrylamide)
PLC	Poly(ε-Caprolactone)
SCDOS	Stem Cell-Derived Organoids
PCCDOS	Patient Cancer Cell-Derived Organoids

PSCS	Pluripotent Stem Cells
ASCS	Adult Stem Cells
CAD	Computer-Aided Design
TME	Tumor Microenvironment
SLA	Stereolithography
2PP	Two-Photon Polymerization
DMEM	Dulbecco's Modified Eagle Medium
FBS	Fetal Bovine Serum
DM	Diabetes Mellitus
BPHS	Brazil's Public Health System
BF	Before Christ
NLB	Natural Latex Biomembranes
DLS	Dynamic Light Scattering
LPS	Lipopolysaccharide
NO_2^-	Nitrite
INOS	Inducible Nitric Oxide Synthase
NEC	Nanoemulsion Containing Curcumin and Annatto Oil
NEOL	Nanoemulsion Containing Annatto Oil
NEB	Nanoemulsion Without Bioactive Compounds

1 THEORETICAL BACKGROUND

1.1 TRANSLATIONAL SCIENCE

Translational science, also known as translational medicine, refers to the process of converting basic scientific discoveries into clinical applications. It bridges fundamental biological research and clinical application, and in the drug development context, drives the progression from target discovery to clinical trials and approval [1].

Drug development within this context is a lengthy and high-cost process, often estimated to require 10–15 years and between $800 million and $2 billion to really delivery a new therapeutic on market. As shown in Figure 1.1. It generally involves four main phases: (I) drug discovery, (II) preclinical development, (III) clinical development, and (IV) regulatory approval.

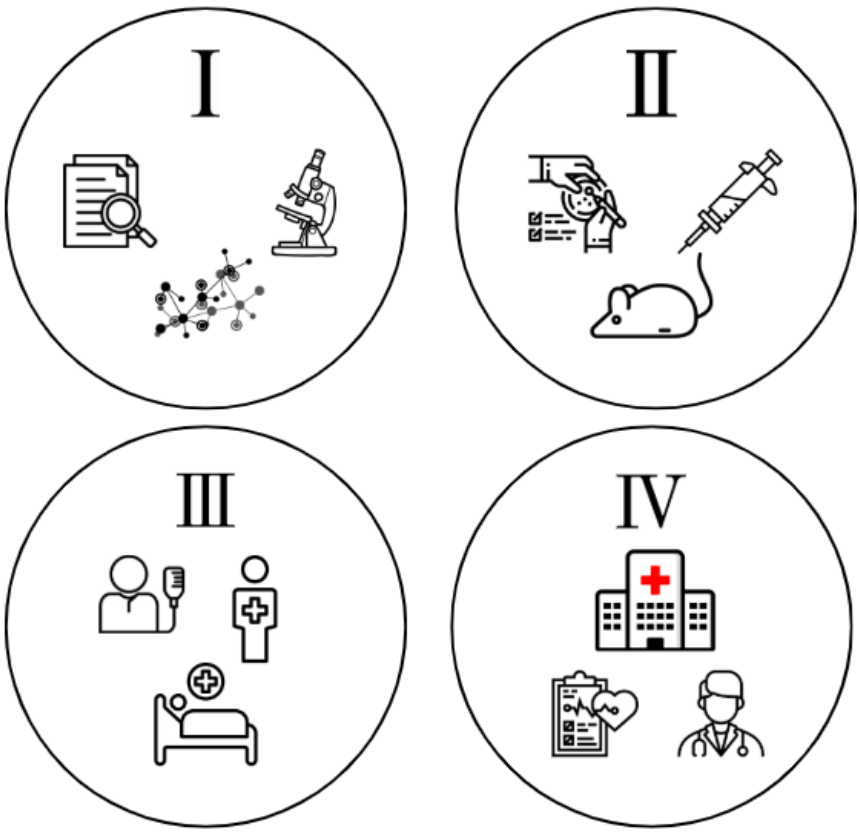

Figure 1.1. Overview of the drug development process: (i) drug discovery, (ii) preclinical development, (iii) clinical development, and (iv) regulatory approval. Figure created by the author using Canva.com (July 2025). Source: the author.

During preclinical development, *in vitro* cell-based assays are essential for evaluating drug absorption, distribution, metabolism, excretion, and toxicity. In this stage, two-dimensional (2D) cell cultures have historically played a dominant role, offering a defined and cost-effective platform for studying drug behavior and mechanisms of action in a controlled environment [2].

However, the predictive power of 2D cultures is limited due to their inability to replicate the complexity of *in vivo* tissues. Consequently, many compounds that show promising results in 2D systems fail during later clinical trials - especially in phases II and III, largely due to lack of efficacy or safety issues that were not detected earlier [2,3].

These limitations have led to growing interest in three-dimensional (3D) culture systems, which better mimic tissue architecture and physiology, improving the translational relevance of preclinical findings [4]. As emphasized by Joseph et al. (2018), integrating physiologically relevant 3D models into preclinical testing is critical to increasing success rates in the drug development pipeline [2].

Recent advancements in biomaterials, biofabrication, and microfluidics have paved the way for organ-on-a-chip (OoaC) technologies, which aim to emulate the structural and functional complexity of human organs *in vitro*. By incorporating dynamic interactions between tissues and systemic responses, these systems offer an advanced alternative to conventional models, particularly in preclinical drug evaluation [1,4].

In the following sections, we dissect the range of preclinical models—from conventional *in vitro* and *in vivo* approaches to the emergence of organ-on-a-chip technologies, highlighting their respective strengths and limitations in translational research.

1.2 Three-Dimensional (3D) Cell Cultures: The Next Step in Preclinical Development

Two-dimensional (2D) cell culture, also known as “flat culture”, has been a reference method in biology for decades and remains a fundamental preclinical stage in drug development. Its simplicity [5], low cost [6], and reproducibility [7] explain its widespread use across research fields, from stem cells to cancer and pharmacology. In 2D systems, adherent cells grow as monolayers on rigid supports, while non-adherent cells remain in suspension, both under relatively homogeneous conditions of oxygen and nutrients (Figure 1.2.1) [3,8,9]. However, this flat configuration imposes limitations: cells adopt an artificial morphology,

intercellular interactions are restricted [10], and gradients of oxygen and nutrients typical of tissues are absent. As a result, 2D cultures fail to replicate key aspects of the in vivo microenvironment, such as necrotic cores in solid tumors [11] or inflammatory signaling central to tumor–immune interactions [12,13].

Figure 1.2.1. 2D cell culture systems: Petri dish and a culture flask containing adherent and non-adherent cells in monolayer configuration. Schematic representation created by the author using Canva.com with support from ChatGPT (July 2025). Source: the author.

Animal models remain the gold standard for preclinical validation, particularly in cancer research [2]. They allow tumor growth and therapeutic testing in a systemic context [7], but their low throughput, long duration, high costs, and ethical issues significantly hinder drug development [2]. Moreover, interspecies differences limit translatability: approximately 40% of drugs showing efficacy in animals fail in clinical trials [14,15].

To overcome these limitations, three-dimensional (3D) culture techniques have emerged as a promising alternative, bridging the gap between 2D systems and animal models [3]. By enabling the formation of multilayered structures, 3D systems reproduce spatial organization, cell–cell and cell–ECM interactions, and gradients of nutrients and oxygen that shape tissue behavior [16,17]. Importantly, these models allow more accurate assessment of drug penetration and therapeutic resistance, often underestimated in 2D systems [18]. In addition,

gene and protein expression profiles in 3D differ significantly from those of monolayers, reflecting more physiologically relevant signaling and metabolic activity [12]. Figure 1.2.2 illustrates the concept of 3D multicellular organization, highlighting the integration of distinct cell populations and the resulting layered architecture that emulates native tissue structure and diffusion behavior.

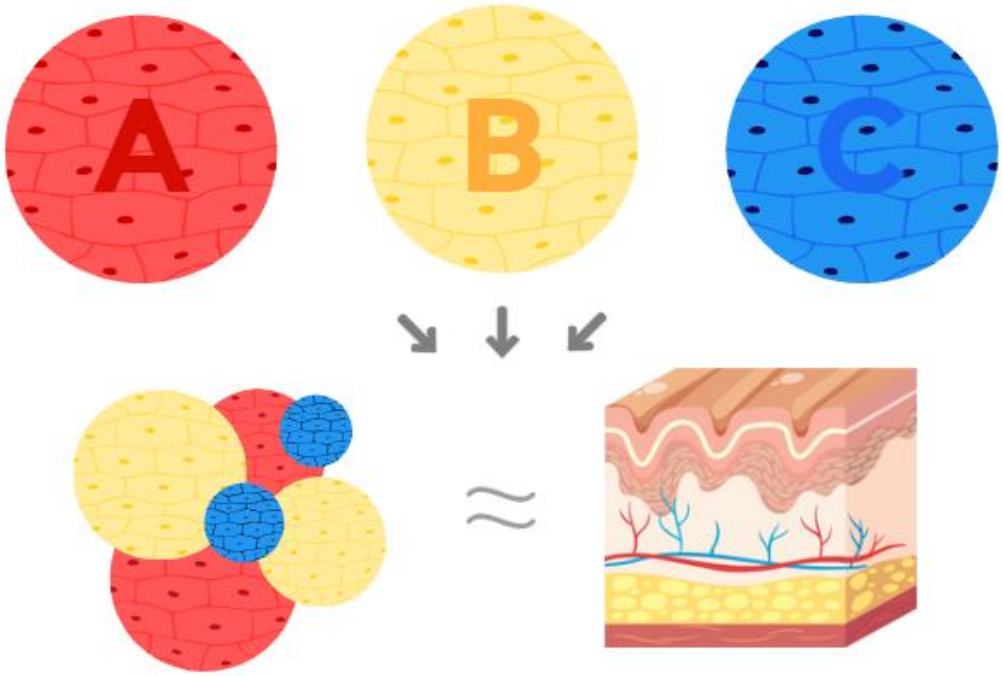

Figure 1.2.2. Multicellular spatial organization in 3D culture mimicking native tissue architecture. Distinct cell types are arranged in a multilayered configuration, forming a tissue-like structure that better replicates the in vivo environment. This setup enables realistic diffusion of nutrients, oxygen, and therapeutic agents, contributing to more accurate modeling of physiological and pathological processes. Schematic representation created by the author using Canva.com with support from ChatGPT (July 2025). Source: the author.

The growing interest in these approaches is evident in the increasing number of publications citing “3D cell culture” since the early 2000s, demonstrating their consolidation as translational tools (Figure 1.2.3). Compared to conventional systems, 3D models reduce time and cost in the development of new therapies and improve their predictive value for clinical outcomes [19].

To better illustrate the specific distinctions between these systems, Table 1.1 summarizes the key differences between 2D and 3D cell culture models, highlighting how three-dimensional configurations more closely reproduce in vivo conditions while overcoming several limitations of traditional monolayer approaches.

Table 1.1. Key Differences Between 2D and 3D Cell Culture Models.

Characteristics	2D Culture	3D Culture
Cellular architecture	Cells grow as a monolayer (adherent cells) or remain suspended in the medium (non-adherent cells); spatial organization is minimal.	Multicellular aggregates, spheroids, or scaffold-based structures; spatially organized and tissue-like architecture.
Microenvironment	Relatively uniform exposure to nutrients and oxygen; lacks the diffusion gradients typical of native tissues.	Gradients of oxygen, nutrients, and metabolites simulate in vivo-like tissue environments.
Cell-cell and cell-ECM interactions	Limited: adherent cells primarily contact the substrate; non-adherent cells may form loose aggregates, but with minimal matrix interaction.	Extensive interactions: cells engage in natural cell–cell and cell–ECM contacts within a 3D matrix.
Gene/protein expression	Expression profiles often diverge from *in vivo* tissues; may reflect artificial proliferation and metabolic patterns.	More physiologically relevant gene and protein expression, resembling those found in native tissues or tumors.
Drug penetration and response	Uniform drug exposure may overestimate drug efficacy and underestimate resistance mechanisms.	Drug diffusion barriers replicate tumor-like resistance; they better predict in vivo therapeutic response.
Cell morphology	Flattened and polarized in adherent cultures; rounded morphology in suspension cultures.	Cells retain native morphology; diverse and tissue-specific structural characteristics emerge.
Reproducibility	High standardized protocols and abundant historical data across various cell lines.	Moderate to high; improving standardization but dependent on system complexity.
Cost and scalability	Low cost and technically simple; suitable for high-throughput applications.	Higher cost and technical complexity; scalability depends on the method used (e.g., spheroids vs. organoids).
Applications	Suitable for studies in cell biology, drug screening, and toxicity testing; it includes cancer, immunology, and stem cell research.	High; replicates histological and molecular aspects of animal or human tissues, supporting better translational outcomes
Limitations	Poor mimicry of native tissue architecture and physiology; lacks gradients, structural cues, and ECM interactions.	Greater physiological relevance but requires more complex handling and validation.
Similarity to *in vivo*	Low; structural and functional features differ significantly from in vivo tissue.	High; replicates histological and molecular aspects of animal or human tissues, supporting better translational outcomes.

1.3 3D BIOPRINTED MODELS

Although 2D cultures and conventional 3D models provide valuable insights into tumor biology, they fall short in replicating the spatial complexity of native tissues. When it comes to developing tumor models for research and personalized medicine, 3D bioprinting represents the next step. This reproducible biofabrication method enables the layer-by-layer construction of biological structures onto substrates or culture dishes containing medium to support cell adhesion, proliferation, and sustained growth with high spatial precision and controllability, thereby closely mimicking their native counterparts [20,21].

Using automated dispensing systems, 3D bioprinting precisely positions heterogeneous cells, biomaterials, and bioactive molecules, which broadens its application in functional tissue generation in vitro and provides in vivo-like microenvironmental cues [20,21]. This automated process relies on three primary components: (i) viable cells, (ii) Computer-Aided-Design (CAD)-based structural blueprints, and (iii) bioinks that provide ECM-like contacts and mechanical support. Together, these elements enable the fabrication of constructs that replicate ECM dynamics, aiding investigations into cancer progression and mechanisms of drug resistance [21-23]. This workflow is illustrated in Figure 1.3, which summarizes the essential components of the 3D bioprinting process.

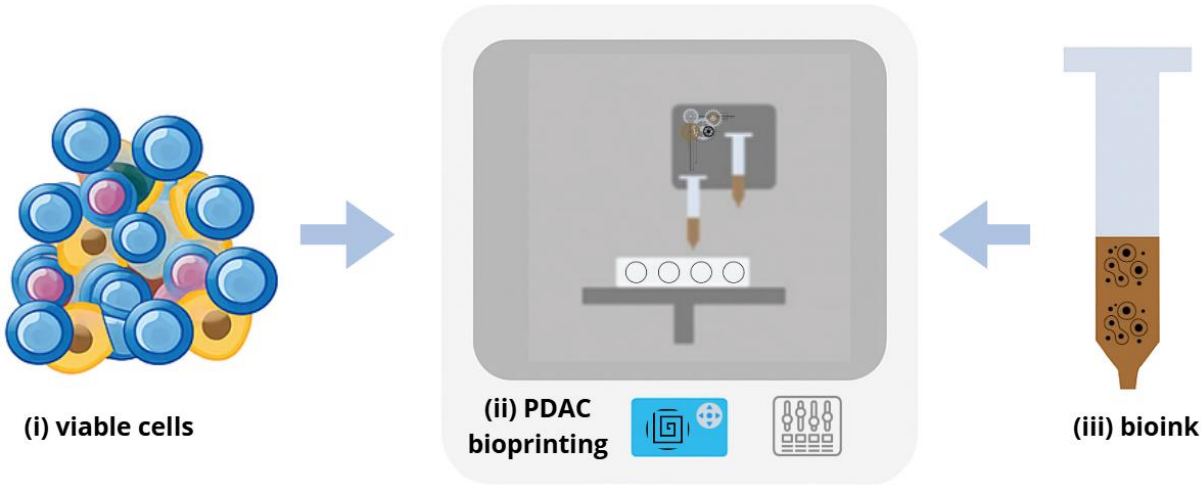

Figure 1.3. Key components of the 3D bioprinting process: (i) viable cells, (ii) CAD-based blueprint, and (iii) bioink containing biological materials and cells. These elements are combined using automated extrusion systems to fabricate physiologically relevant tissue constructs. Schematic representation created by the author using Canva.com (July 2025). Source: the author.

The bioink is a fundamental element of 3D bioprinting. It is typically composed of hydrogels, living cells, and other essential bioactive agents that simulate the extracellular matrix (ECM), providing both mechanical support and biochemical cues for cellular survival, proliferation, and differentiation [21,23,24]. Bioinks must balance printability (mechanical stability and structural fidelity) with biological relevance (biostability and biocompatibility). Depending on their origin, they are classified as natural, synthetic, or hybrid polymers. Their characteristics, advantages, and limitations are summarized in Table 1.2.

Table 1.2. Types and Description of the Main hydrogel Polymers Used for 3D Bioprinting.

Polymer Type	Definition	Examples	Advantages	Disadvantages
Natural	Derived from natural sources such as plants, animals, or microorganisms. Biocompatible and biodegradable.	Collagen, Alginate, Gelatin, Hyaluronic Acid	High biocompatibility, supports cell growth and differentiation, naturally biodegradable.	Poor mechanical strength, inconsistent properties, rapid degradation in some environments.
Synthetic	Man-made polymers designed for controlled mechanical properties such as strength, degradation rate, and printability.	Polyethylene Glycol (PEG), Polycaprolactone (PCL), Polylactic Acid (PLA)	Good mechanical properties, controlled degradation, customizable for specific applications.	Limited biocompatibility, requires surface modifications, may have toxic degradation byproducts.
Hybrid	Combination of natural and synthetic polymers to leverage the advantages of both types, enhancing mechanical and biological properties.	Gelatin-Methacryloyl (GelMA), Poly(lactic-co-glycolic acid) (PLGA), Composite Hydrogels	Combines biocompatibility of natural polymers with mechanical strength of synthetic polymers, offering better structural integrity and bioactivity.	Complex synthesis and processing, potential compatibility issues between polymer components.

A crucial aspect of 3D bioprinting for tumor modeling is the integration of the bioink composition and crosslinking strategy, a chemical or physical process that promotes the formation of bonds between the polymer chains of a hydrogel to accurately mimic the tumor microenvironment (TME). Crosslinking can be chemical (e.g., UV light or enzymatic catalysis) or physical (e.g., temperature or ionic bonding) and must be selected based on mechanical stability requirements and the sensitivity of the encapsulated cells. Additionally, the selection of specific cell types is critical to replicate the cellular heterogeneity of the TME [8].

Various bioprinting techniques have been developed to accommodate different applications, especially in tissue engineering [9]. Each technique has distinct operational principles, advantages, and limitations that directly influence the choice of method depending on the type of tissue to be replicated, the desired resolution, and the required cell viability. Among the main approaches are inkjet bioprinting, extrusion-based bioprinting, stereolithography (SLA), two-photon polymerization (2PP), and laser-assisted bioprinting [5].

These methods vary in terms of precision, speed, compatibility with different bioinks, supported cell density, and the complexity of the structures they can produce. Table 1.3 summarizes the main characteristics of each method.

Table 1.3. Types and Description of the Main Methods Used for Manufacturing 3D Bioprinting Models.

Method	Definition	Advantages	Disadvantages
Inkjet Bioprinting	Deposits bioink droplets via thermal, piezoelectric, or electromagnetic forces.	High speed, low cost; suitable for cartilage, bone, skin, and vasculature.	Low precision, nozzle clogging, limited to low viscosity bioinks and cell densities.
Extrusion-Based Bioprinting	Extrudes continuous bioink filaments using mechanical/pneumatic pressure.	Compatible with high-viscosity materials and physiologically relevant cell densities; ideal for dense tissues.	Reduced cell viability, potential cellular deformation.
Stereolithography (SLA)	UV/laser-induced photopolymerization of resin for 3D structuring.	High complexity, <25 μm resolution, rapid fabrication.	Limited material options, UV exposure risks, and lengthy post-processing.
Two-Photon Polymerization	SLA variant achieving sub-diffraction resolution (<100 nm) via two-photon absorption.	Ideal for microfluidics and in vitro microenvironments.	Slow fabrication, unsuitable for large constructs, and low polymer biocompatibility.
Laser-Assisted Bioprinting	Laser pulses vaporize bioink from a ribbon, depositing it onto a substrate.	High resolution (~10 μm), high cell density (>10^8 cells/mL), excellent viability.	Time-consuming ribbon preparation, low throughput.

Li et al. [6] emphasized that, to ensure adequate oxygen and nutrient delivery, efficient waste removal, and faithful replication of the physiological conditions of native organs, the presence of a functional vascular network is indispensable. Moreover, the effectiveness of such a bioartificial vascular system depends largely on how closely it mimics natural vascular physiology [7]. In the context of vascular 3D printing, it is essential to consider the structural and functional differences among various types of blood vessels when designing an extracorporeal vascular network. Ensuring that 3D-printed bioartificial organs receive a sufficient blood supply is crucial for maintaining a stable microenvironment that supports long-term cell survival and functionality [6].

These foundational principles of vascular integration are equally critical for the development of organ-on-a-chip (OoAC) systems, where the recreation of dynamic, perfusable networks is essential to mimicking physiological conditions *in vitro*. The following section will explore how these microengineered platforms leverage such biofabrication strategies to model complex tissue environments and systemic interactions.

1.4 ORGAN-ON-A-CHIP

Although 3D cell culture models such as spheroids and organoids represent asignificant progress toward physiologically relevant *in vitro* systems, they still fall short of replicating the full complexity of the *in vivo* microenvironments. One of their major limitations is the inability to simulate the dynamic mechanical and biochemical cues that are naturally present in living tissues and organs, such as blood flow, respiratory movements, peristalsis, and tumor-induced mechanical stress [12].

These constraints reduce their predictive accuracy in both drug development and disease modeling. To overcome these challenges, microfluidic-based systems have emerged as a promising solution. These technologies aim to better replicate the dynamic conditions of human physiology, thereby improving the accuracy of preclinical models [12].

Recreating physiologically accurate cellular microenvironments that truly resemble complex in vivo architectures is a key aspect in the development of advanced *in vitro* organotypic tissue constructs [10]. Among others, organ-on-a-chip technology has been

increasingly used in recent years to create improved models for organs and tissues in human health and disease, because of its ability to provide spatio-temporal control over soluble cues, biophysical signals, and biomechanical forces necessary to maintain proper organotypic functions [7,11].

1.4.1 Concept

Recent innovations in biomaterials, bioengineering, and additive manufacturing have paved the way for the emergence of innovative platforms such as bioprinted tissues, lab-on-a-chip systems, and, more recently, organ-on-chip technologies [4]. These approaches are designed to replicate not only the architecture but also the dynamic functions of human organs, tissues, and pathological conditions in a controlled *in vitro* environment [10].

Organ-on-a-chip systems stand out for their ability to recreate complex human tissue architectures and physiological functions outside the body. By integrating relevant cell types within biomimetic microenvironments, these platforms offer a powerful means to study human biology and disease processes with unprecedented precision. Their potential to generate representative *ex vivo* models holds great promise for deepening our understanding of organ-level functions and accelerating the development of next-generation therapeutics [13].

1.4.2 Components

The structural basis of most Organ-on-a-Chip systems is polydimethylsiloxane (PDMS), a silicon-based organic polymer widely adopted for its mechanical flexibility, gas permeability, optical transparency, and excellent biocompatibility [12]. Soft lithography — pioneered by the Whitesides group — enables precise fabrication [25]. The resulting chips consist of compact networks of microchannels that allow for precise spatial patterning of cells and enable the control of physicochemical parameters such as fluid flow, shear stress, oxygen levels, pressure, and pH, thereby creating finely tuned microenvironments that simulate *in vivo* conditions [12].

A defining component of these systems is the microfluidic network itself, which regulates the continuous supply of culture media and the removal of metabolic waste [5]. Microfluidics allows precise control of ultrasmall fluid volumes (nanoliters to attoliters) within microscale channels (tens to hundreds of micrometers in dimension) [14]. This

allows the miniaturization of complex biological systems while maximizing control and minimizing the use of costly reagents and limited biological samples [12]. Combined with ECM mimics and tissue-specific cells, these microengineered devices offer scalable and reproducible models that are transforming biomedical research through their ability to simulate micro-scale biological interactions with high precision [1]. Figure 1.4 illustrates the Organ-on-a-Chip concept, highlighting PDMS-based microdevices perfused with culture medium and populated with tissue-specific organ models.

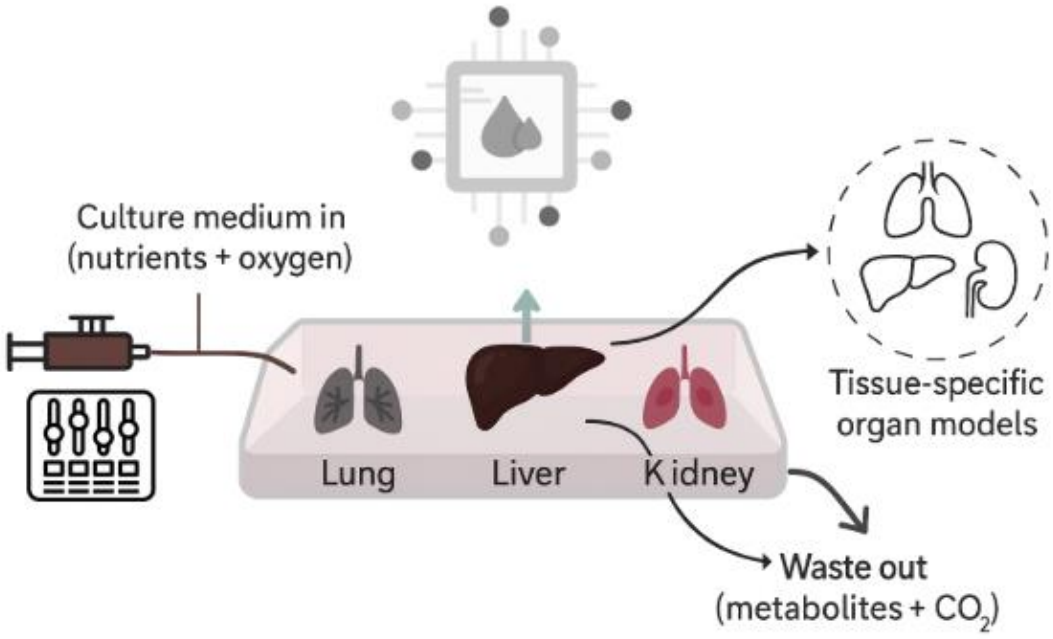

Figure 1.4. Schematic representation of the Organ-on-a-Chip (OoAC) concept. PDMS-based microfluidic chips are perfused with nutrient- and oxygen-rich culture medium, maintaining tissue-specific organ models such as lung, liver, and kidney. Metabolic waste and CO_2 are eliminated through controlled outflow channels. These platforms simulate physiological microenvironments in real time, enabling applications in disease modeling, pharmacokinetics, and drug toxicity screening. Schematic representation created by the author with support from ChatGPT (July 2025). Source: the author.

1.4.3 Applications and Challenges

Organ-on-a-chip (OOC) platforms provide superior physiological fidelity compared to traditional *in vitro* and animal models. One of their main advantages lies in the improved ability to predict human responses to drugs, which can reduce dependence on animal testing while enhancing clinical success rates. Additionally, OOC platforms can integrate real-time sensors and mathematical models to generate functional, quantitative data, allowing

continuous monitoring of drug efficacy and toxicity [15]. These features allow long-term modeling of disease mechanisms and therapeutic responses, spanning days to months [16,17].

For example, Mun et al. developed a pancreas-on-a-chip system to co-culture patient-derived pancreatic ductal epithelial cells (PDECs) with insulin-producing islet cells, enabling the investigation of cell-cell interactions relevant to cystic fibrosis. Their results demonstrated that defective CFTR activity impaired insulin secretion by islet cells, highlighting the potential of organ-on-a-chip platforms to model human disease mechanisms and assess therapeutic strategies in a physiologically relevant *in vitro* environment [18].

Glieberman et al. developed a thermoplastic-based *Islet-on-a-Chip* platform that automates islet loading, synchronized glucose stimulation, and real-time insulin detection using an on-chip immunoassay. By mimicking physiological perfusion and employing scalable materials compatible with commercial fabrication, the device enables continuous, precise, and high-throughput analysis of β cell function. Their results demonstrate the platform's potential to streamline diabetes research and therapeutic development by overcoming limitations of traditional insulin secretion assays [19].

Although microfluidic systems and organ-on-a-chip platforms have progressed in modeling intricate cellular constructs, a persistent hurdle is the precise spatial organization of cells into layered 2D/3D configurations required to replicate human tissue heterogeneity. While traditional 2D cell patterning methods (e.g. microcontact printing, laminar flow) are established, their integration into organ-on-a-chip designs remains underdeveloped [5].

Recent years have seen the emergence of innovative microfluidic methods for patterning proteins, cells, and 3D cellular assemblies. These include established approaches like microcontact printing and laminar flow patterning, as well as newer strategies utilizing dynamic actuators, textured surfaces, and microengineered structures to manipulate hydrogel-based cell cultures [26]. However, conventional fabrication methods (e.g., lithography, gel confinement) remain constrained in their ability to replicate tissues with intricate 3D architectures [27,28].

Bioprinting offers a promising solution, allowing spatially precise one-step fabrication of multicomponent constructs. By integrating 3D bioprinting with organ-on-chip

platforms, researchers can enhance in vitro organoid models through the incorporation of physiologically relevant structures within tailored extracellular matrices [4]. Therefore, the convergence of bioprinting and microfluidics represents a powerful strategy for advancing next-generation disease models. This integration opens new avenues for creating more predictive in vitro systems capable of recapitulating complex microenvironments, setting the stage for their application to challenging pathological contexts that will be explored in the following sections.

1.5 PDAC AND DFU: SHARED FEATURES

Despite their distinct clinical manifestations, pancreatic ductal adenocarcinoma (PDAC) and diabetic foot ulcers (DFUs) share fundamental pathophysiological mechanisms rooted in chronic, dysregulated inflammation. In both diseases, the inflammatory response is not merely a secondary consequence but rather a key driver of disease progression and therapeutic resistance [29,30,31].

A hallmark of this dysregulation is immune imbalance, particularly macrophage dysfunction. In PDAC, the tumor microenvironment is enriched with immunosuppressive cells such as M2-polarized macrophages and cancer-associated fibroblasts, which promote tumor progression and resistance to therapy [32,33]. Similarly, in DFU, the persistent predominance of pro-inflammatory M1 macrophages prevents the necessary transition to M2 reparative phenotypes, thereby impairing wound healing [34,35]. This imbalance illustrates how both conditions are governed by maladaptive immune responses that perpetuate tissue damage rather than resolution.

Both PDAC and DFU are further characterized by persistent, dysregulated inflammatory signaling, involving elevated levels of pro-inflammatory cytokines such as TNF-α and IL-6, along with activation of canonical inflammatory pathways including NF-κB [33,34]. These molecular drivers establish a hostile microenvironment: in PDAC, they sustain tumor growth, angiogenesis, and therapeutic resistance, while in DFU they maintain chronic wounds in a non-healing state. Adding to this convergence, diabetes itself represents a key risk factor for PDAC. Epidemiological studies indicate that individuals with type 2 diabetes mellitus (T2DM) exhibit a 1.5- to 2-fold increased risk of developing

PDAC, particularly when diabetes onset occurs within the preceding 2–3 years [36,29]. Proposed mechanisms include the combined effects of chronic hyperglycemia, obesity, and insulin resistance, which promote systemic inflammation and metabolic alterations that can facilitate pancreatic carcinogenesis [29,37].

Together, these parallels underscore the urgent need for advanced preclinical models that faithfully replicate the complexity of inflammatory microenvironments in both cancer and chronic wounds. Conventional in vitro approaches often fail to capture the immunological and stromal dimensions that critically influence drug response. By contrast, innovative platforms—such as 3D bioprinted tumor models and organ-on-a-chip systems—offer the possibility of evaluating therapeutic efficacy under realistic immunological influences. These technologies hold promise for addressing diseases like PDAC and DFU, where persistent inflammation and immune dysregulation remain central barriers to effective treatment [4,21,38]

1.5.1 DFU – Pathogenesis and Burden

DFUs represent one of the most debilitating complications of diabetes mellitus, affecting 15–25% of diabetic patients during their lifetime and standing as a leading cause of non-traumatic lower-limb amputations worldwide [30]. Their clinical burden is particularly pronounced in low- and middle-income countries, where limited access to specialized care exacerbates the risk of infection, chronic disability, and premature mortality [31]. Beyond their clinical impact, DFUs impose a significant economic burden. In Brazil alone, they account for nearly US$264 million annually in hospitalizations—half of which are due to amputations—and an additional US$333 million in outpatient care, highlighting their status as a major public health challenge [39,40]

At the mechanistic level, DFUs arise from the convergence of chronic hyperglycemia, peripheral neuropathy, and impaired vascularization, which collectively compromise tissue repair. Persistent hyperglycemia sustains an inflammatory milieu through the generation of advanced glycation end-products (AGEs), activation of NF-κB pathways, and excessive production of reactive oxygen species (ROS), further impairing cellular repair capacity [34].

A defining feature of DFUs is immune dysregulation, particularly macrophage dysfunction. Unlike physiological wound healing, which requires a timely transition from

pro-inflammatory M1 to reparative M2 macrophages, DFUs remain locked in a persistent M1-dominant state. This imbalance maintains elevated levels of pro-inflammatory cytokines such as TNF-α, IL-1β, and IL-6, while failing to activate anti-inflammatory mediators like IL-10, ultimately preventing progression to the proliferative and remodeling phases of healing [34,35]. As illustrated in Figure 1.5.1, physiological wound closure is driven by IL-10, which stimulates TGF-β and VEGF production, promoting angiogenesis and inhibiting iNOS, IL-6, and IL-1β activity. In contrast, DFUs are characterized by sustained TNF-α production, which amplifies IL-1β, IL-6, and iNOS expression, perpetuating chronic inflammation and delayed repair [41].

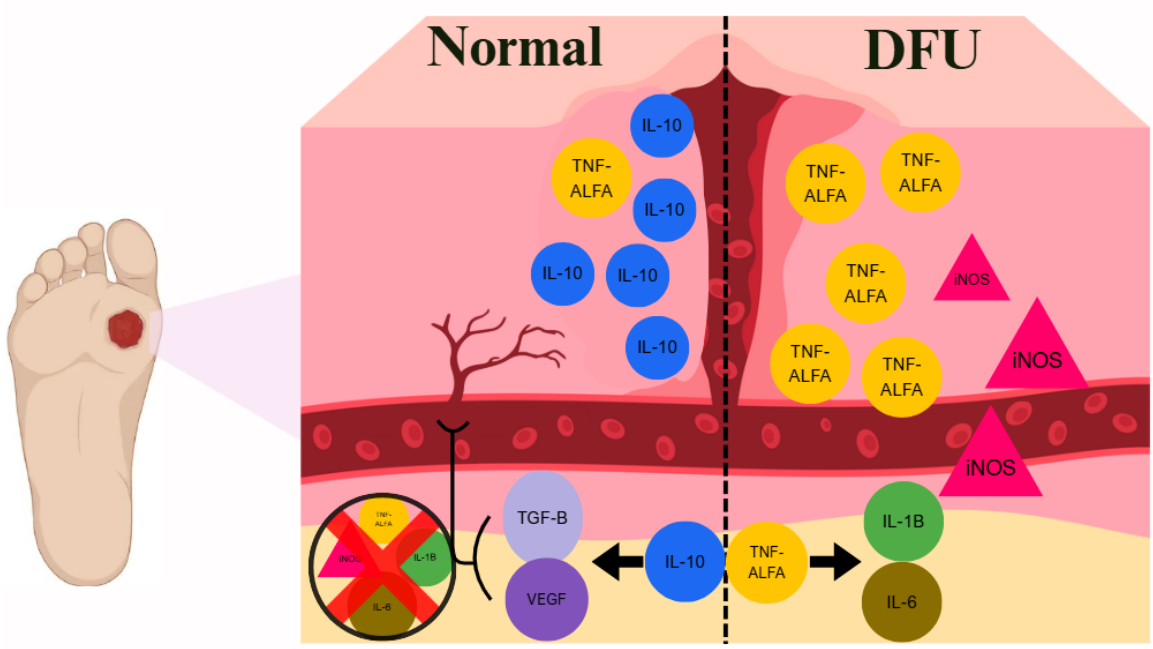

Figure 1.5.1. Comparative cytokine dynamics in normal wound healing versus diabetic foot ulcers (DFUs). Left: In physiological wound healing, balanced immune signaling favors resolution of inflammation, characterized by higher IL-10 levels and subsequent induction of TGF-β and VEGF, which promote angiogenesis and tissue repair, while downregulating iNOS, IL-6, IL-1β, and TNF-α. Right: In DFUs, chronic hyperglycemia sustains a pro-inflammatory state dominated by persistent TNF-α, IL-1β, IL-6, and iNOS activity, impairing angiogenesis and delaying wound closure. Schematic representation created by the author using Canva.com (July 2025). Source: the author

These immune defects are compounded by vascular insufficiency and neuropathy, which reduce tissue oxygenation, impair angiogenesis, and diminish the local delivery of nutrients and growth factors essential for tissue repair [30]. As a result, DFUs become chronic, non-healing wounds highly susceptible to microbial colonization and infection, contributing to the high incidence of amputations.

Given these complexities, DFUs are now recognized as multifactorial inflammatory disorders rather than isolated mechanical lesions. Their pathogenesis underscores the urgent need for advanced in vitro models that faithfully capture the interactions between immune cells, stromal elements, and microbial factors. In this context, 3D bioprinting and organ-on-a-chip platforms emerge as promising tools for reproducing the chronic inflammatory microenvironment of DFU. These systems could enable mechanistic studies of immune dysfunction, testing of novel bioactive compounds, and the design of personalized therapies tailored to the unique immunological profile of each patient [4,21,38,42].

1.5.2 PDAC – Pathogenesis and Microenvironment

PDAC represents 90% of malignant pancreatic tumors, being a highly aggressive, lethal malignancy due to the lack of early diagnosis and limited response to treatments [43]. Metastatic dissemination typically occurs through lymphatic and neural invasion, a process driven by the epithelial–mesenchymal transition (EMT) phenotype adopted by pancreatic cancer cells [33]. In addition to genetic predisposition, fatty infiltration of the pancreas has been associated with the development of pancreatic intraepithelial neoplasia (PanINs), precursor lesions that follow a sequential accumulation of genetic mutations and evolve into invasive carcinoma [37]. Among these mutations, KRAS (detected in ~90% of cases), CDKN2A, TP53 (50–70%), and SMAD4 (60–90%) represent central drivers of malignant transformation, deregulating cell cycle control, apoptosis, and tumor suppression [29].

Beyond its genetic hallmarks, the defining challenge of PDAC lies in its tumor microenvironment (TME). PDAC tumors are characterized by an abundant desmoplastic stroma composed of cancer-associated fibroblasts (CAFs), dense ECM, and poor vascularization. This stromal barrier not only restricts drug penetration but also provides biochemical and mechanical cues that actively sustain tumor growth and invasion. At the immunological level, the TME is enriched with immunosuppressive cell populations, including regulatory T cells, myeloid-derived suppressor cells, and M2-like macrophages, which collectively inhibit cytotoxic T lymphocyte function and blunt anti-tumor immunity. This immune evasion, combined with the physical barrier of the stroma, contributes directly to therapy resistance and the dismal prognosis of PDAC [44,45].

The interplay between tumor cells, stromal elements, and infiltrating immune populations generates a highly complex and hostile ecosystem that remains difficult to model in preclinical settings. Conventional two-dimensional cultures fail to replicate the spatial heterogeneity and stromal dominance of PDAC, while animal models only partially capture its immunosuppressive landscape. Consequently, despite decades of research, PDAC continues to exhibit one of the lowest five-year survival rates among solid tumors, underscoring the urgent need for innovative in vitro models that faithfully reproduce its pathophysiological complexity [33].

1.6 THERAPEUTIC APPROACHES AND EMERGING TECHNOLOGIES

The management of chronic diseases such as diabetic foot ulcers (DFUs) and pancreatic ductal adenocarcinoma (PDAC) relies heavily on conventional approaches that, despite decades of refinement, remain insufficient to address the biological complexity of these conditions [29,46].

In DFUs, traditional strategies focus on controlling infection, promoting tissue repair, and preventing recurrence. Standard protocols include debridement to remove necrotic tissue and disrupt biofilms, systemic antimicrobials, topical agents, and advanced dressings designed to balance moisture, absorb exudate, or provide antimicrobial activity. Examples include hydrocolloids, calcium alginate, and silver-based dressings, widely employed within the Brazilian Public Health System [46]. Despite their benefits, these interventions face major limitations such as poor tissue penetration, the rise of antimicrobial resistance, and limited effectiveness in preventing systemic infections. Even with adjunctive modalities like low-level laser therapy (LLLT) or light-emitting diodes (LEDs), which stimulate cellular metabolism and angiogenesis, recurrence remains high and amputation rates persistently elevated, underscoring the need for more effective and accessible therapies [47–50].

Similarly, in PDAC, surgical resection remains the only potentially curative treatment. However, the late presentation of most patients means that only a small minority are eligible for surgery, and even among those resected, recurrence rates are high. Adjuvant chemotherapy, particularly modified FOLFIRINOX (mFOLFIRINOX), has improved

survival compared to gemcitabine monotherapy, and neoadjuvant regimens are increasingly used to enhance surgical outcomes [74]. Radiotherapy may provide local control, but systemic resistance and rapid progression limit its long-term benefits. Immunotherapies, which have transformed the treatment of many malignancies, have shown little success in PDAC due to its profoundly immunosuppressive tumor microenvironment, characterized by desmoplastic stroma and inhibitory immune cell populations [32,33]. Although novel agents such as CD40 agonists and cancer vaccines are under investigation, clinical translation has so far been modest.

The limited efficacy of these classical treatments, combined with the persistently poor outcomes, highlights the urgent need for innovative approaches in both DFU and PDAC. For DFUs, translational advances have introduced biomaterials such as alginate–bioglass composites and the application of phototherapy as non-invasive adjuncts to stimulate repair [47–49]. For PDAC, preclinical research has increasingly focused on three-dimensional (3D) tumor models to improve the predictive power of drug screening, as more than 90% of candidate molecules still fail in clinical trials despite promising preclinical results [51–53]. Among these, 3D bioprinting has emerged as a powerful strategy, enabling the fabrication of structured, reproducible models that incorporate tumor cells, fibroblasts, and immune components to better recapitulate the tumor microenvironment [38,54].

In this translational context, the RAPHA® system represents an innovative therapeutic platform specifically designed for DFU management, combining biomaterials and light-based therapies to modulate chronic inflammation and stimulate tissue regeneration. By integrating phototherapy with novel nanobiotechnological approaches—such as photoactivated nanoemulsions containing curcumin and annatto oil—RAPHA® extends beyond traditional wound care to address the complex pathophysiology of chronic ulcers. At the same time, the application of 3D bioprinted models in PDAC research provides a complementary avenue to overcome therapeutic resistance, offering physiologically relevant platforms for testing innovative treatments. Together, these strategies exemplify how translational technologies can bridge fundamental pathophysiology with therapeutic innovation, forming the conceptual basis for the studies developed in this dissertation.

1.6.1 RAPHA® System and Translational Strategies

The RAPHA® System (Tissue Neoformation System) is an innovative therapeutic platform developed by the Biomedical Engineering Department at the University of Brasília (UnB/FCTE) for the treatment of diabetic foot ulcers (DFUs). The system combines natural latex biomembranes (NLBs) with LED phototherapy, integrating bioactive and photobiomodulatory components into a cost-effective device suitable for home use. It was designed to enhance wound healing, particularly in patients with limited access to advanced clinical care [55].

The therapeutic rationale behind RAPHA® is based on the individual properties of its components. Natural latex, derived from *Hevea brasiliensis*, is widely recognized for its biocompatibility, angiogenic potential, and ability to promote tissue regeneration [56]. Processed into biomembranes through centrifugation and vulcanization, these membranes provide an extracellular matrix-like structure and stimulate fibroblast proliferation and neovascularization—features that are crucial in chronic wound healing, especially in ischemic tissues [57]. Complementing the biomembrane, the phototherapy unit of RAPHA® contains thirty high-intensity LEDs emitting in the 480–650 nm range, delivering 25 J/cm² [56]. Studies report that this wavelength range enhances collagen synthesis, neovascularization, and cellular metabolism, while reducing inflammation and bacterial load [58].

Clinical trials supported by the Brazilian Ministry of Health (2017–2019) confirmed the efficacy of RAPHA®, showing a mean contraction rate of 41% for RAPHA®-treated ulcers, compared to 22% in the standard SUS protocol [59]. Additional outcomes included reductions in oxidative stress and improvements in patient-reported quality of life. Importantly, the system's simplicity enables decentralization of care, with significant implications for public health economics [60].

Despite its clinical effectiveness, RAPHA® still presents an open question regarding its direct anti-inflammatory effects, which motivates ongoing investigations into synergistic integration with nanobiotechnology. Building upon this platform, our group has advanced toward multifunctional formulations, such as curcumin- and papain-loaded natural latex membranes combined with red LED phototherapy (patent BR132021001940), which achieved wound contraction rates of up to 99% in preclinical diabetic models [61].

These findings support the rationale for incorporating nanoemulsions with phytoactive compounds, further enhanced by photoactivation.

In this study, we specifically investigated a nanoemulsion containing curcumin (*Curcuma longa*) and annatto oil (*Bixa orellana*), activated by blue LED light. Curcumin is well documented for its anti-inflammatory, antioxidant, and regenerative effects [62,63], while annatto oil, rich in bixin and tocotrienols, promotes wound contraction, re-epithelialization, and modulation of oxidative stress [64–66]. Co-encapsulation within a photoresponsive nanobiotechnological platform offers a promising strategy to potentiate the RAPHA® approach and expand its translational applicability to chronic inflammatory wounds. This conceptual advance is illustrated in Figure 1.6.

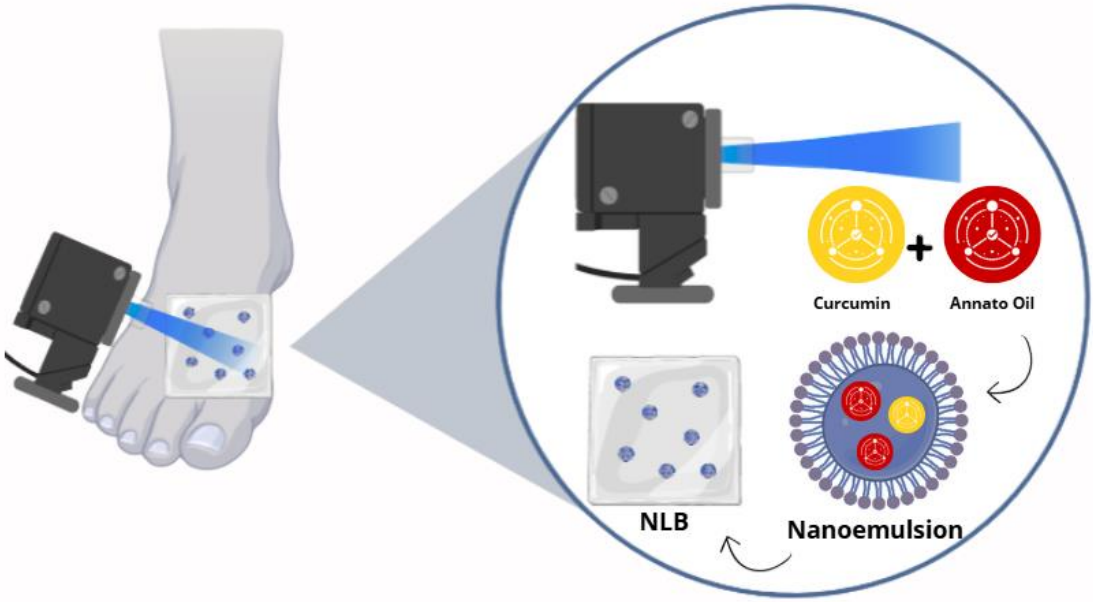

Figure 1.6. Conceptual schematic of the proposed photoactivated therapeutic strategy: a nanoemulsion containing curcumin (a bioactive compound derived from *Curcuma longa*) and annatto oil (extracted from *Bixa orellana* seeds) is envisioned to be applied over a natural latex biofilm (NLB) and activated by blue LED irradiation. This platform is designed to promote anti-inflammatory effects and support tissue repair in chronic wounds such as diabetic foot ulcers. Schematic representation created by the author using Canva.com (July 2025). Source: the author.

The translational reasoning underlying RAPHA® also resonates with the challenges in oncology, particularly in pancreatic ductal adenocarcinoma (PDAC). Just as DFU therapy demands integrated solutions to overcome chronic inflammation and impaired healing, PDAC therapy requires physiologically relevant preclinical models to address its stromal and immunosuppressive complexity.

In this context, 3D bioprinting emerges as a complementary technological frontier, capable of reconstructing the tumor microenvironment with stromal and immune elements using tailored bioinks. These bioinks—summarized in Table 1.4— are not merely carriers of cells; they constitute dynamic matrices that integrate hydrogels, extracellular matrix (ECM)-derived components, and bioactive molecules to recreate tissue-specific biochemical and mechanical cues. Such formulations directly influence cell viability, proliferation, and phenotype, thereby determining the physiological fidelity of the printed constructs. Importantly, tailoring bioinks allows fine-tuning of viscoelasticity and degradability to match the native pancreatic stroma, while enabling co-culture of multiple cell types in spatially defined patterns [67].

Table 1.4. Comparative Overview of Bioink Formulations for Tumor Bioprinting and Potential Alternatives to Enhance Structural Stability in Bioprinted Constructs

Composition	Type	Crossslinkg	Advantages	Reference
10–20% GelMA + Eosin Y (0.01–0.1 mM) + TEA (0.1–1% w/v) + NVP (37–370 nM)	Soft printable bioink, visible light crosslinkable hydrogel	Visible light(400-500nm), 10 min exposure, SLA 3D Bioprinting	Tunable stiffness, supports cell adhesion and proliferation, suitable for patterned cell-laden constructs	[133]
4.0% gelatin, 0.75% alginate, 1.4% carboxymethylated cellulose nanocrystals (CCNC)	Shear-thinning hydrogel for meniscal bioprinting	Ionic (Ca^{2+} crosslinking of alginate); potential for enzymatic or chemical crosslinking (e.g., glutaraldehyde)	High printability, >98% cell viability, promotes collagen II expression, maintains chondrocyte phenotype, stable for >6 months in culture	[134]
15% oxidized alginate (5% oxidation)	Natural polysaccharide	Ionic crosslinking with divalent cations (e.g., Ca^{2+} or Sr^{2+}); pre-printing oxidation tuning	High printability and scaffold integrity; promotes spreading phenotype; supports enhanced osteogenesis and chondrogenesis; mimics native ECM properties; improved degradability	[135]
Hybrid: GelMA + PLGA + Composite Hydrogels	Natural-synthetic composite bioink	Varies depending on component (e.g., UV + thermal)	Combines biocompatibility and mechanical strength for improved structure and bioactivity	[136]
3% (w/v) decellularized adipose tissue (DAT) hydrogel solubilized in 0.5 M acetic acid with 10% w/w pepsin (to tissue weight)	Natural ECM-based hydrogel	Thermal gelation (30 min at 37 °C)	Shear-thinning, high-throughput printable bioink; supports cell viability, cancer morphology, gene expression (Oct4, Sox2, MMP2, MMP9); mimics tumor microenvironment; effective for THP-1 containment	[137]

Legend: 21PT = HER2+ human breast cancer cells; ADMSC = Adipose-derived mesenchymal stem cells; DAT = Decellularized adipose tissue; MDA-MB-231 = Triple-negative breast cancer cell line.

Together, the RAPHA® platform and 3D bioprinting models illustrate how bioengineering strategies bridge innovation and clinical need, providing the foundation for the experimental chapters that follow.

1.7 OBJECTIVES

1.7.1 General

This dissertation aimed to explore translational bioengineering strategies by integrating two complementary approaches: (i) the evaluation of photoactivated nanoemulsions containing curcumin and annatto oil as potential anti-inflammatory agents for chronic wound healing, particularly in the context of diabetic foot ulcers (DFUs); and (ii) the development and characterization of a three-dimensional (3D) bioprinted model of pancreatic ductal adenocarcinoma (PDAC), incorporating tumor, stromal, and immune components to better replicate the tumor microenvironment.

1.7.2 Specifics

- To determine the cytocompatibility of nanoemulsion formulations through MTT assay in RAW 264.7 macrophages;
- To evaluate the anti-inflammatory potential of the nanoemulsions by quantifying nitric oxide (NO_2^-) production via the Griess assay;
- To assess the immunomodulatory activity of the formulations by measuring TNF-α and IL-10 levels using ELISA, under both irradiated and non-irradiated conditions;
- To generate a 3D triculture PDAC construct using extrusion-based bioprinting with Panc-1, MeWo, and THP-1-derived macrophages;
- To evaluate the structural integrity and reproducibility of the printed constructs;
- To assess cell viability over a 5-day period using confocal imaging and Live/Dead assays;
- To explore the feasibility of using this model for future drug screening applications and integration with microfluidic platforms.

This chapter presents a scientific article for submission to a journal in the Engineering IV area (CAPES). This study evaluates nanoemulsions containing curcumin and annatto oil as potential anti-inflammatory agents for photodynamic therapy in chronic wounds. The research includes cytocompatibility assessment and immunomodulatory analyses under both irradiated and non-irradiated conditions.

2 PAPER 1

Blue Light-Enhanced Nanoformulations: Curcumin and Annatto Oil as Photodynamic Agents in Inflammation Modulation

Lucas Meyer Syllos[1,4], Gabriella de Oliveira Silva[2,4], Mosar Corrêa Rodrigues[2,4], Luísa Coutinho Coelho[3], Anamélia Lorenzetti Bocca[3], Graziella Anselmo Joanitti[2,4], Marcella Lemos Brettas Carneiro[1,2,4]*.

[1] Postgraduate Program in Biomedical Engineering, University of Brasília, Brazil.

[2] Postgraduate Program in Nanoscience and Nanobiotechnology, University of Brasília, Brazil.

[3] Laboratory of Applied Immunology, Department of Cellular Biology, Institute of Biological Sciences, University of Brasília, Brazil.

[4] Laboratory of Bioactive Compounds and Nanobiotechnology (LBCNano), University of Brasilia.

*Corresponding author: marbretas@unb.br

Abstract

Chronic wounds such as diabetic foot ulcers remain a major clinical challenge due to persistent inflammation and impaired healing. This study presents the evaluation of photoactivated nanoemulsions containing curcumin and annatto oil for potential application in photodynamic therapy. The formulations were characterized by dynamic light scattering (DLS), confirming nanometric size distribution and stability. Cytotoxicity was assessed using MTT assays in RAW 264.7 macrophages, revealing no significant reduction in viability at concentrations up to 2.4 µg/mL for all tested nanoemulsions, even under blue light-emitting diode (LED) irradiation. To investigate anti-inflammatory potential, nitric oxide production was quantified via the Griess assay after lipopolysaccharide (LPS) stimulation. A significant reduction in nitrite (NO_2^-) levels was observed in macrophages treated with curcumin- and annatto-loaded nanoemulsions, particularly under irradiated conditions, suggesting partial inhibition of inducible nitric oxide synthase (iNOS) signaling. ELISA assays revealed a marked reduction in TNF-α secretion and an increase in IL-10 release when cells were treated with curcumin- and annatto-loaded nanoemulsions under blue LED irradiation, compared to their non-

irradiated counterparts. These findings indicate that, in addition to reducing NO_2^- production, the formulations promoted a shift toward an anti-inflammatory profile under photoactivation, supporting their potential as multifunctional adjunct therapies in chronic wounds. This work lays the groundwork for future exploration of multifunctional nanocarriers integrated into the RAPHA® platform.

Keywords: nanoparticles; diabetic foot ulcer (DFU); wound healing, herbal bioactives; wound dressings; *in vitro* assays; immunomodulation; photobiomodulation; translational science.

2.1 INTRODUCTION

Diabetes mellitus (DM) is a chronic metabolic disease characterized by persistent hyperglycemia and associated with a wide range of complications [1], among which diabetic foot ulcers (DFUs) represent one of the most debilitating [2]. DFUs are chronic wounds that affect 19–34% of diabetic patients, with recurrence rates of 40% within one year and over 65% within three years. In Brazil, where over 12 million individuals live with diabetes, approximately 25% develop lower limb ulcers, which account for 85% of non-traumatic amputations and generate more than R$498 million in outpatient care costs annually. In addition to high morbidity and mortality, DFUs impose a disproportionate economic burden on public health systems. A 2015 study in Paraná revealed that actual hospitalization costs for diabetic amputations were 3.6 times higher than Brazilian Unified Health System (BUHS) reimbursements, while inadequate post-healing care contributes to reulceration in over 50% of cases [3]. These data highlight the need for novel, accessible, and more effective therapies for chronic wound management in diabetic populations.

The impaired healing process in DFUs is primarily driven by chronic hyperglycemia, which promotes a cascade of pathological mechanisms that hinder normal tissue repair. Sustained high glucose levels lead to endothelial dysfunction, reduced angiogenesis, persistent oxidative stress, and dysregulated immune responses. In particular, the overproduction of reactive oxygen species (ROS) overwhelms antioxidant defenses, resulting in cellular damage that interferes with all phases of wound healing [4]. This hostile microenvironment favors a chronic pro-inflammatory state, with macrophages locked in the M1 phenotype, secreting cytokines such as TNF-α and IL-6, and impairing progression to the reparative M2 phase. Combined with neuropathy, reduced vascular perfusion, and frequent bacterial colonization, these factors result in wounds that remain in

a prolonged inflammatory phase, fail to re-epithelialize, and frequently become chronic and infected [5].

Despite the range of conventional treatments available for DFUs—such as surgical debridement, topical antibiotics, and advanced dressings —clinical outcomes remain suboptimal [6], especially within the context of public health systems like BUHS. The most frequently used treatments, including hydrocolloids, essential fatty acids, silver sulfadiazine, and calcium alginate dressings, often fail to promote satisfactory wound resolution, particularly in refractory or infected ulcers [7]. Additionally, these approaches do not effectively address the underlying pathophysiological mechanisms, such as chronic inflammation and oxidative stress [8]. This therapeutic gap, combined with high recurrence rates, prolonged healing time, and elevated treatment costs, has led to the development of alternative strategies aimed at modulating the inflammatory response and enhancing tissue regeneration. One such innovation is the Rapha® Therapeutic System, developed at the University of Brasília (UnB), which combines a natural latex biomembrane (NLB) with low-level light therapy (LED) to stimulate healing in chronic wounds [3,9,10].

The Rapha® Therapeutic System consists of two synergistic components: a NLB, derived from *Hevea brasiliensis*, and a LED phototherapy device emitting visible light in the 480–650 nm range [11,12]. The latex film promotes tissue regeneration by enhancing fibroblast proliferation and collagen deposition, while the photobiomodulatory effect of the LED stimulates angiogenesis, reduces inflammation, and increases bactericidal activity [3,9,13]. This combinatorial approach has shown superior clinical outcomes compared to the gold-standard wound care protocols used in the BUHS. Clinical trials conducted between 2017 and 2019 demonstrated that Rapha® treatment significantly increased wound contraction (41% vs. 22%) and improved patient quality of life by enabling at-home use, reducing clinical visits, and lowering long-term healthcare costs [5]. To further potentiate its therapeutic effectiveness, the system could be benefit from the integration of nanobiotechnology and phytocompounds, such as curcumin and annatto oil, which offer additional anti-inflammatory, antioxidant, and possibly antimicrobial properties [14-18].

Nanoemulsions are colloidal dispersions with droplet sizes typically below 200 nm that can be produced by high-energy methods such as emulsification and ultrasonication. Their reduced size improves the solubility and stability of poorly water-soluble bioactives

like curcumin, while facilitating interaction with biological barriers and enabling photoactivation strategies [19,20]. Despite these advantages, nanoemulsions still raise concerns regarding non-specific toxicity, stability, and reproducibility, as well as potential organ bioaccumulation. In vivo and translational studies remain limited, highlighting the need for further safety evaluation before clinical application [21]

This knowledge gap motivated further innovation through the integration of nanobiotechnology and bioactive phytocompounds, aiming to enhance the system's anti-inflammatory and antioxidant performance in diabetic wounds. In the clinical study published by Gomes et al. (2025), a latex-based biomembrane incorporating curcumin-loaded liposomes was successfully applied to chronic wounds, including diabetic foot ulcers. The treatment promoted improved granulation tissue formation and wound contraction rates up to 90%, representing a 70% increase compared to conventional public healthcare treatments [22]. Despite these promising clinical results, the study did not quantify the anti-inflammatory response elicited by the formulation, nor access its antimicrobial activity, leaving critical mechanistic aspects of the therapy unexplored.

In this work, we propose an alternative nanoemulsion formulation combining curcumin with annatto oil (*Bixa orellana*), a natural source of bixin and norbixin with well-documented antioxidant, anti-inflammatory, and wound healing properties [17,23]. The objective is to evaluate the cytotoxicity and immune modulation capacity of this phytotherapeutic nanoemulsion using *in vitro* assays, advancing the scientific basis for next-generation therapies targeting chronic wounds in diabetic patients.

Thus, the present study aimed to develop and characterize a nanoemulsion containing curcumin and annatto oil and evaluate its cytotoxicity and inflammatory modulation in RAW 264.7 macrophages. The goal was to investigate whether this combination could serve as a safe and bioactive platform for chronic wound care by evaluating cytotoxicity, cytokine modulation, and nitric oxide release—key parameters involved in the inflammatory process of diabetic foot ulcers.

2.2 MATERIALS AND METHODS

2.2.1 Nanoemulsions

The nanoemulsions evaluated in this study were developed and kindly provided by Gabriella de Oliveira Silva, a member of our research team. The formulations were designed as part of a broader research initiative currently under development.

Three types of oil-based nanoemulsions were used: one containing curcumin and annatto oil (NeC), one with annatto oil only (NeOl), and a control formulation without bioactive compounds (NeB). The preparation method was based on high-energy emulsification followed by ultrasonication, ensuring droplet sizes within the nanometric range and physical stability of the formulations. All formulations were produced under controlled conditions and stored at 4 °C until further analysis.

Their physicochemical characterization, including average droplet size, polydispersity index (PDI), and zeta potential, was performed using dynamic light scattering (ZetaSizer® Nano ZS90, Malvern, UK) at room temperature, with detection angle set to 90°. Before measurement, samples were diluted in distilled water (1:50, v/v) to ensure optimal light transmission, and three technical replicates were used to calculate the Z-average values.

2.2.2 Cell Culture

RAW 264.7 murine macrophages (ATCC® TIB-71™) were cultured in Dulbecco's Modified Eagle Medium (DMEM, high glucose) supplemented with 10% fetal bovine serum (FBS), 1% penicillin-streptomycin, and 1% sodium pyruvate. Cells were maintained under standard conditions of 37 °C, 5% CO_2, and 95% relative humidity in 75 cm^2 culture flasks and subculture using a sterile cell scraper upon reaching 80–90% confluence. All experiments were conducted using cells between passages 5 and 15. For *in vitro* assays, cells were seeded in 96-well plates at a density of 5×10^3 cells/well and incubated for 24 hours before treatment.

2.2.3 Cytotoxicity Assay (MTT)

Cell viability was assessed using the MTT assay (3-(4,5-dimethylthiazol-2-yl)-2,5-diphenyltetrazolium bromide) adapted from standard protocols [24]. After 24 h of incubation for cell adhesion, treatments were applied with the nanoemulsions NeC, NeOl, and NeB, using seven serial dilutions starting at 9.8 µg/mL, calculated based on the curcumin content in the NeC formulation. Equivalent dilutions were applied to NeOl and

NeB to maintain comparative concentration profiles. Vehicle controls containing 1% DMSO, 1% ethanol, and cell-only control were also included.

After 24 h of treatment, 150 µL of MTT solution (5 mg/mL in complete DMEM) were added to each well, followed by incubation for 2 h at 37 °C. The supernatant was then carefully removed, and the resulting formazan crystals were solubilized in 150 µL of DMSO. Absorbance was measured at 595 nm using a microplate reader. Cell viability was calculated as a percentage relative to the untreated control. All conditions were performed in technical quadruplicates, and the experiment was repeated in three independent biological assays.

2.2.4 Nitric Oxide Quantification (Griess Assay)

Nitric oxide (NO) production was indirectly quantified by measuring nitrite (NO_2^-) levels in the culture supernatant using the Griess reagent. After 24 h of treatment with nanoemulsions and/or LPS, culture plates were divided into irradiated and non-irradiated groups. For the irradiated condition, cells were exposed to a 1-minute pulse of blue LED light (λ = 470 nm) positioned 5 cm above the plate, with an estimated energy fluence of up to 14 J/cm² (Figure 2.1).

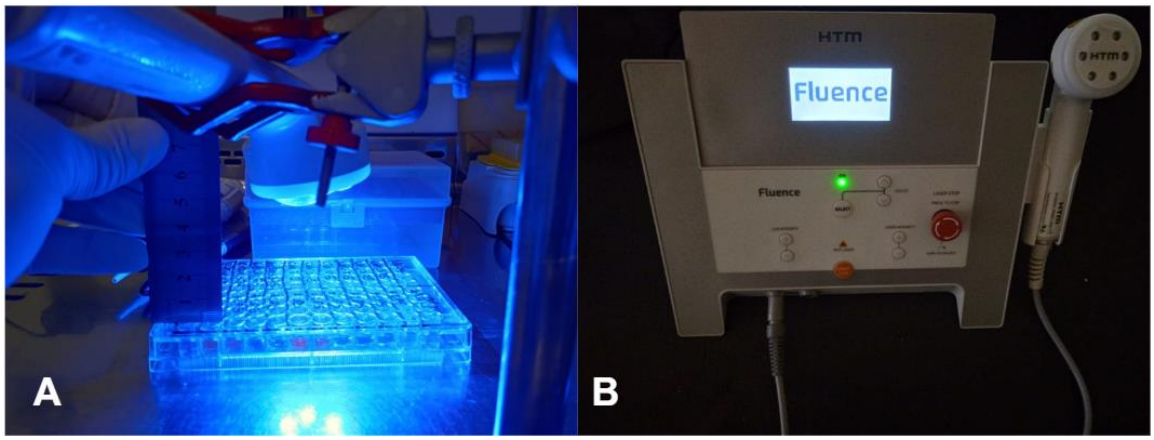

Figure 2.1. Blue LED irradiation used in the project experiment. (A) Experimental setup for 96-well plate irradiation, with light source positioned 5 cm above the samples, delivering a 1-minute pulse of blue light (λ = 470 nm, fluence up to 14 J/cm (B) HTM® Fluence device employed as a photodynamic therapy platform for photoactivation of curcumin- and annatto-based nanoemulsions. The equipment was acquired specifically for in vitro and in vivo assays of the projects at the University of Brasília (UnB). Note: this equipment is not part of the original Rapha® system patented by UnB.

After irradiation, supernatants of both plates (irradiated and non-irradiated) were collected and transferred to labeled microtubes. The assay was performed in 96-well plates, where 50 µL of each sample were loaded in duplicate. The Griess reagent was prepared by mixing equal volumes of two stock solutions: (A) 1% sulfanilamide in 5% H_3PO_4 (prepared by dissolving 250 mg of sulfanilamide in 1.25 mL of 5% phosphoric acid and 23.75 mL of distilled water), and (B) 0.1% N-(1-naphthyl) ethylenediamine dihydrochloride (NEED) in distilled water (25 mg in 25 mL). Reagent A and B were combined 1:1 immediately before use.

Then, 100 µL of the freshly prepared Griess reagent were added to each well containing 50 µL of supernatant. Plates were incubated for 5–10 minutes at room temperature, protected from light. Absorbance was measured within 30 minutes at 540 nm using a microplate reader. To generate a standard curve, sodium nitrite ($NaNO_2$) was used at concentrations ranging from 1.56 µM to 100 µM (serial 2-fold dilutions from 100 µM), prepared in the same culture medium used in the cell experiments. The nitrite concentrations in the experimental samples were interpolated based on the standard curve. This method is well established for quantifying NO release in RAW 264.7 macrophages under inflammatory stimulation, particularly in studies using curcumin and its derivatives [14,25].

2.2.5 Inflammatory Stimulation and Cytokine Quantification (ELISA)

To evaluate the anti-inflammatory potential of the nanoemulsions, RAW 264.7 macrophages were plated at a density of 6×10^4 cells/well in 96-well plates and incubated for 24 h to allow adherence and recovery. After this period, the culture medium was replaced with 480 µL of fresh DMEM containing the nanoemulsions (NeC, NeOl, or NeB) at a non-cytotoxic concentration previously established by MTT assay. For functional assays, three concentrations were selected: 0.3 µg/mL (low reference), 2.4 µg/mL, and 4.9 µg/mL of curcumin equivalent for NeC, applied correspondingly to all groups. The maximum concentration of 9.8 µg/mL was evaluated only in the cytotoxicity screening. After 1 h of pre-treatment, 20 µL of a working solution of lipopolysaccharide (LPS) at 25 µg/mL were added to each well to induce an inflammatory response (final concentration: 1 µg/mL LPS per well). For the negative control (basal inflammation), 20 µL of PBS were added instead of LPS. Cells were then incubated for 24 h at 37 °C and

5% CO_2. After stimulation, supernatants were carefully collected to avoid disturbing adherent cells, transferred to labeled microtubes, and stored at –20 °C until analysis.

Quantification of cytokine levels was performed using commercial sandwich ELISA kits following the manufacturers' protocols [26]. The cytokines analyzed were TNF-α and IL-10, chosen to represent key pro- and anti-inflammatory pathways in macrophage activation [27,28]. Each plate included a full standard curve, blanks, and internal positive controls. Absorbance was read at 450 nm using a microplate spectrophotometer (e.g., Synergy HT or equivalent). Cytokine concentrations were calculated from standard curves using four-parameter logistic regression, and results were expressed in pg/mL. All treatments were performed in quadruplicate, and experiments were repeated in three independent assays.

2.2.6 Statistical Analysis

All statistical analyses were performed using GraphPad Prism version 8.0.1 (GraphPad Software, San Diego, CA). One-way ANOVA followed by Tukey's multiple comparisons test was used for Griess assay and ELISA, and two-way ANOVA followed by Sidak's multiple comparisons test was used for MTT assay under irradiated and non-irradiated conditions. Results are presented as mean ± standard deviation (SD), $p < 0.05$ was considered statistically significant.

2.3 RESULTS

2.3.1 Nanoemulsion Characterization

The three nanoemulsion formulations—NeC, NeOl, and NeB—were successfully prepared using a high-energy emulsification method involving ethanol evaporation followed by ultrasonication. The emulsification process consisted of film hydration, coarse emulsion formation, and ultrasonication (previously described at session 2.1), delivering a total energy of 1,260,000 J to achieve nanoscale droplet dispersion. This combination of high-energy emulsification and ultrasonication is commonly employed for lipophilic compounds such as curcumin and annatto oil, as it facilitates the formation of kinetically stable dispersions with enhanced bioactive encapsulation efficiency [19].

Dynamic light scattering (DLS) was used to evaluate the average droplet size, polydispersity index (PDI), and zeta potential of each diluted formulation. The results are summarized in Table 2. NeC exhibited an average droplet size of 105.81 ± 51.72 nm and a PDI of 0.52 ± 0.16, indicating a relatively broad size distribution. NeOl, in contrast, displayed the largest droplet diameter (309.80 ± 15.39 nm) but with improved homogeneity (PDI = 0.26 ± 0.32). NeB showed a smaller and more monodisperse profile, with a droplet size of 135.30 ± 5.76 nm and a low PDI of 0.18 ± 0.03. Zeta potential analysis was also performed to assess the colloidal stability of the formulations, yielding values between −31.9 ± 0.89 mV and −35.2 ± 0.43 mV. These values fall within the range typically associated with electrostatically stable nanoemulsions containing curcumin and vegetable oils, as previously reported in similar systems [29].

Table 2. Physicochemical parameters of nanoemulsions determined by DLS.

Formulation	Droplet Size (nm)	Polydispersity Index (PDI)	Zeta Potential (mV)
NeC	105.81 ± 51.72	0.52 ± 0.16	-35.2 ± 0.43
NeOl	309.80 ± 15.39	0.26 ± 0.32	-34.5 ± 0.54
NeB	135.30 ± 5.76	0.18 ± 0.03	-31.9 ± 0.89

The characterization confirms that all formulations achieved nanometric size ranges (<500 nm), suitable for biological interaction and cellular uptake in vitro [30]. The higher PDI observed for NeC suggests potential heterogeneity in droplet populations, indicating a need for further optimization to enhance formulation uniformity in future studies.

2.3.2 Cytotoxicity Assay (MTT)

Given that nanoemulsions represent colloidal carriers with potential for clinical application, it is essential to evaluate their cytocompatibility in immune cells. RAW 264.7 macrophages were selected as an in vitro model due to their central role in inflammatory signaling relevant to chronic wounds. The cytotoxic potential of the nanoemulsions (NeC, NeOl, NeB) and their respective free compound controls (C: curcumin; Ol: annatto oil; B: sunflower oil) was evaluated using the MTT assay in RAW 264.7 macrophages. The assay

was conducted after 24 hours of treatment using seven serial dilutions, ranging from 0.2 to 9.8 µg/mL, adjusted to reflect curcumin concentration in the NeC formulation. All conditions were tested in technical quadruplicates across three independent biological replicates

As illustrated in Figures 2.2 and 2.3, all formulations exhibited a dose-dependent effect on cell viability. At lower concentrations (0.2–2.4 µg/mL), none of the nanoemulsions (Figure 2.2) demonstrated cytotoxicity. However, from 2.4 µg/mL onward, a significant reduction in viability was observed, especially at 9.8 µg/mL, where NeC and NeOl reached 21.1% and 34.5%, respectively. NeB maintained better biocompatibility, with 63.1% viability at the same dose. Among the free compounds (Figure 2.3), curcumin (C) showed the highest cytotoxicity, reducing viability below 80% from 0.6 µg/mL and reaching ~16.8% at 9.8 µg/mL. Annatto oil (Ol) also exhibited a concentration-dependent reduction, though less pronounced. Sunflower oil (B), in contrast, preserved cell viability above 100% across all concentrations tested.

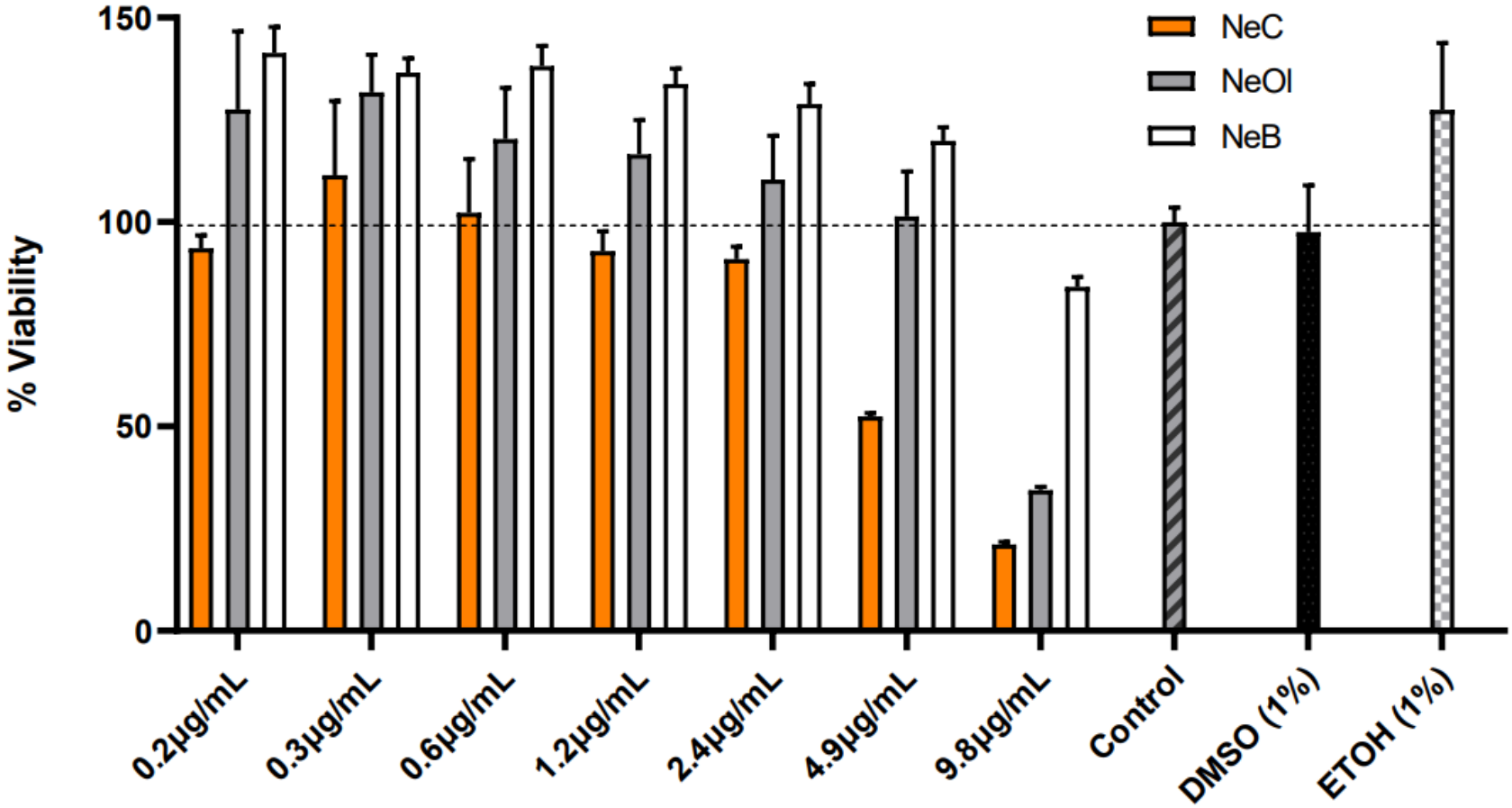

Figure 2.2. Cytotoxicity profile of nanoemulsions (NeC, NeOl, NeB) in RAW 264.7 macrophages. Cell viability was evaluated using the MTT assay after 24 h of treatment with increasing concentrations (0.2 to 9.8 µg/mL), adjusted for curcumin concentration. Data are expressed as mean ± standard deviation from three independent experiments performed in quadruplicate. The bar graph illustrates a dose-dependent decrease in viability for NeC and NeOl, while NeB maintained higher biocompatibility.

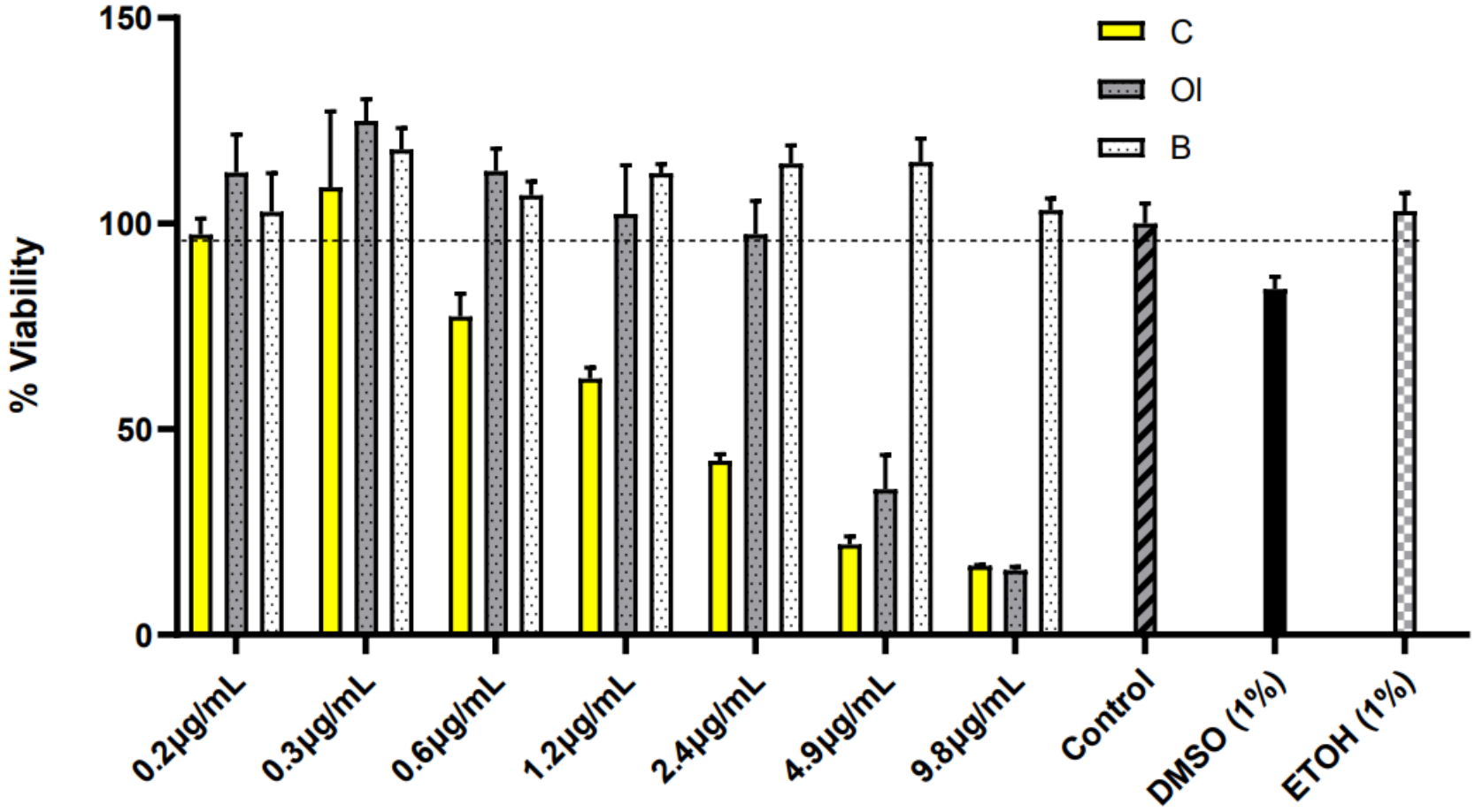

Figure 2.3 Cytotoxicity profile of the respective free components—curcumin (C), annatto oil (Ol), and sunflower oil (B)—in RAW 264.7 macrophages. Cell viability was evaluated using the MTT assay after 24 h of treatment with increasing concentrations (0.2 to 9.8 µg/mL), adjusted for curcumin concentration. Free curcumin showed the most significant reduction in viability, while sunflower oil preserved viability above 100% across all concentrations tested.

Among the free compound controls, free curcumin (C) exhibited the highest cytotoxicity, with viability decreasing below 80% as early as 0.6 μg/mL and reaching ~16.8% at 9.8 μg/mL. Free annatto oil (Ol) also showed a decline in viability in a dose-dependent manner, though less severe. In contrast, sunflower oil (B) maintained cell viability above 100% across all tested concentrations. It is noteworthy that some formulations, particularly those containing curcumin and annatto oil, as well as sunflower oil, presented absorbance values slightly above 100% cell viability in the MTT assay. Similar findings have been reported in pigmented or lipid-based formulations, where intrinsic coloration or light scattering may interfere with formazan absorbance, rather than reflecting true proliferative effects [31,32].

Based on these results, the concentrations of 2.4 μg/mL and 4.9 μg/mL were selected as the upper safe threshold for subsequent assays (Griess and ELISA), with 0.3 μg/mL used as a lower comparison point. These findings confirm that nanoencapsulation significantly reduces curcumin cytotoxicity and supports its biocompatibility and application in further anti-inflammatory assays.

2.3.3 Nitric Oxide Quantification (Griess Assay)

To investigate the potential anti-inflammatory effects of the nanoemulsions, nitric oxide (NO) production was indirectly assessed by measuring nitrite (NO_2^-) levels in RAW 264.7 macrophage supernatants after 24 h of treatment with or without LPS stimulation, in both non-irradiated and LED-irradiated conditions. Figures 2.4–2.7 present the results separately for curcumin- and annatto-based formulations under non-irradiated and irradiated conditions, allowing direct comparison between free compounds and their respective nanoemulsions.

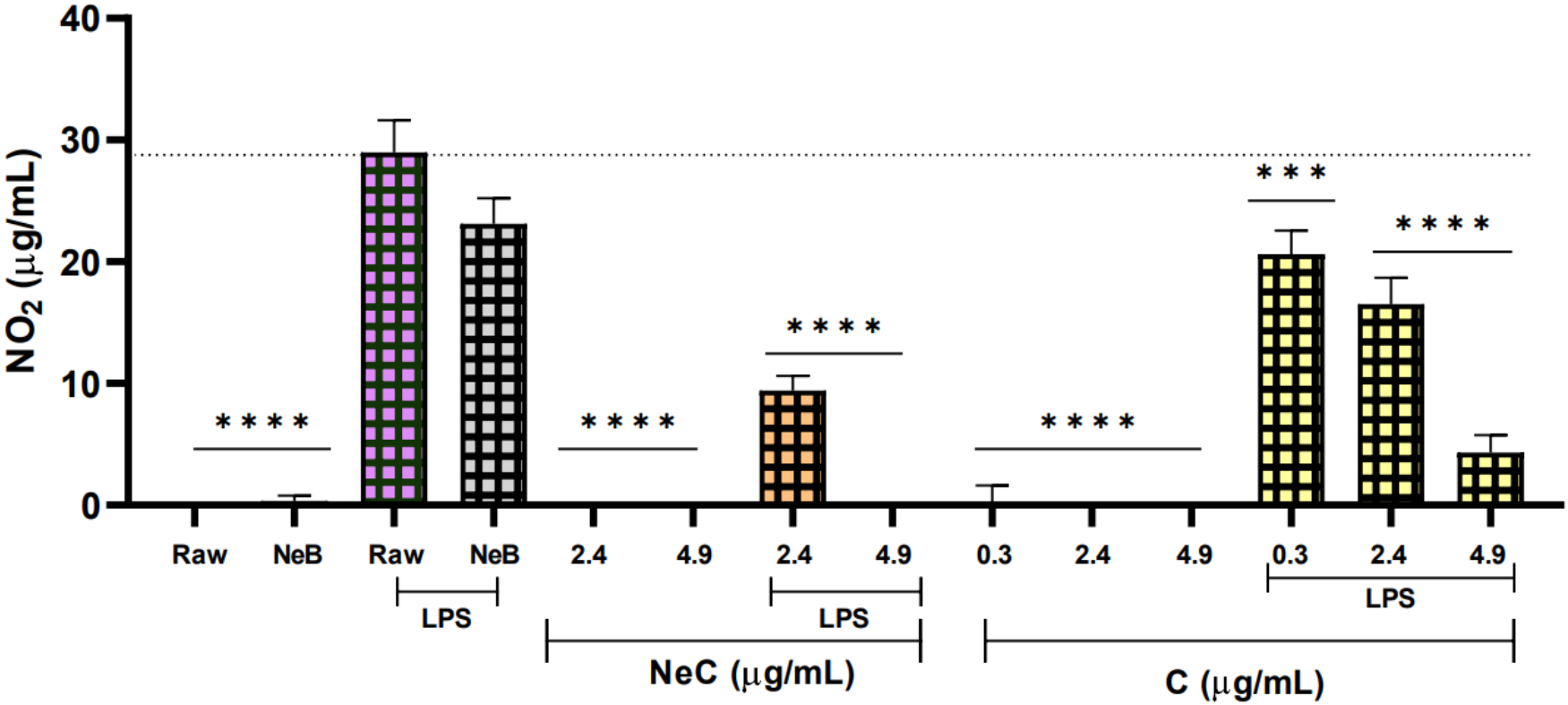

Figure 2.4. Effect of curcumin (C) and curcumin nanoemulsion (NeC) on nitrite (NO_2^-) production by RAW 264.7 macrophages under non-irradiated conditions. Data are presented as mean ± SD (n = 3). Statistical significance: *p < 0.05, **p < 0.005, ***p < 0.001, ****p < 0.0001; ns = not significant.

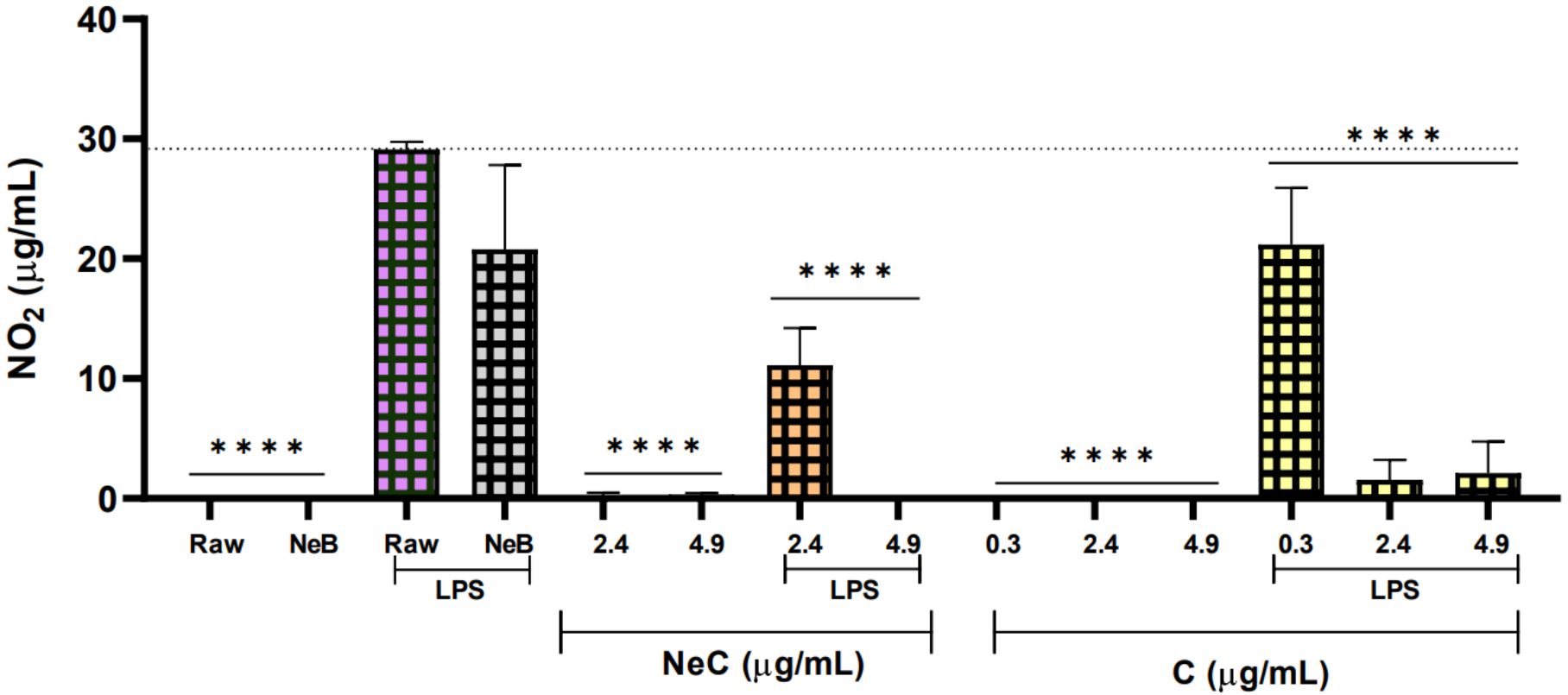

Figure 2.5. Effect of curcumin (C) and curcumin nanoemulsion (NeC) on nitrite (NO_2^-) production by RAW 264.7 macrophages under irradiated conditions. Data are presented as mean ± SD (n = 3). Statistical significance: *p < 0.05, **p < 0.005, ***p < 0.001, ****p < 0.0001; ns = not significant.

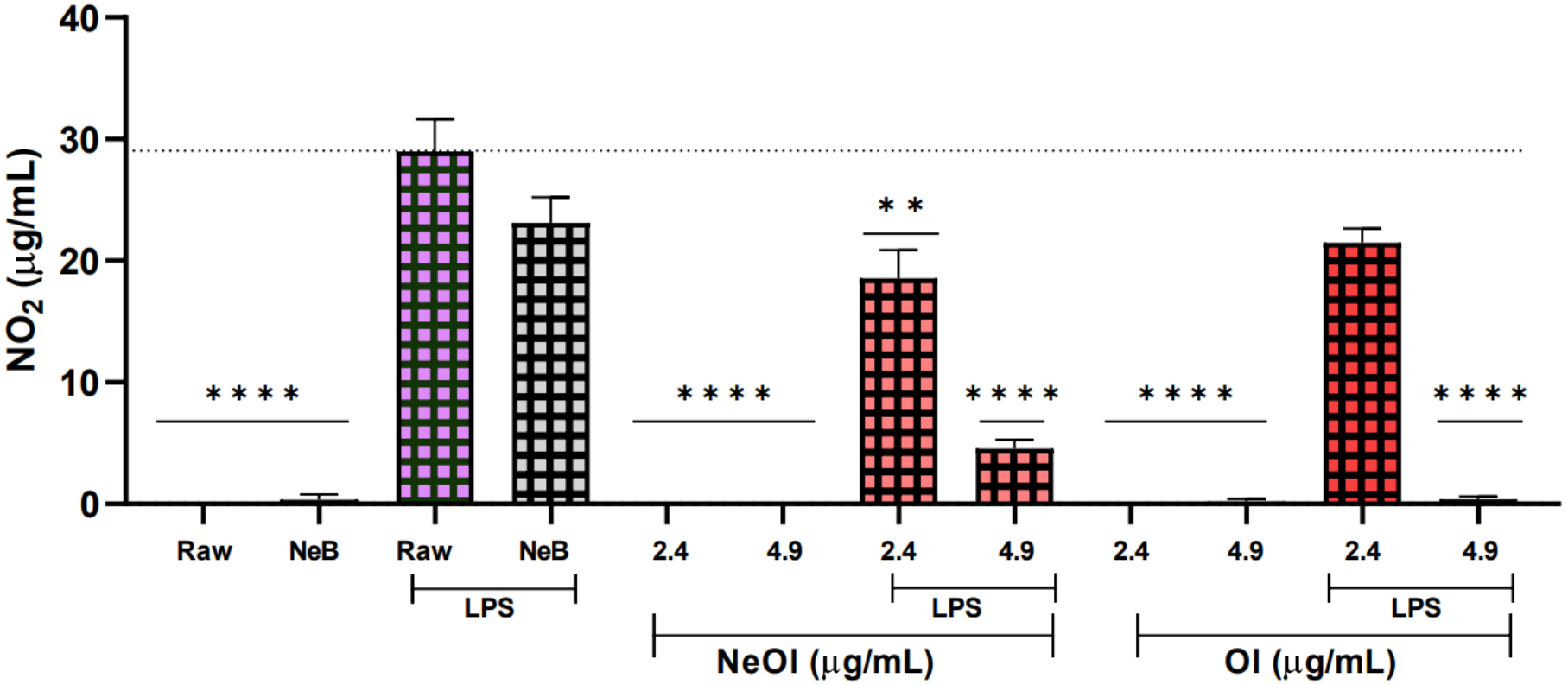

Figure 2.6. Effect of annatto oil (Ol) and annatto nanoemulsion (NeOl) on nitrite (NO_2^-) production by RAW 264.7 macrophages under non-irradiated conditions. Data are presented as mean ± SD (n = 3). Statistical significance: *p < 0.05, **p < 0.005, ***p < 0.001, ****p < 0.0001; ns = not significant.

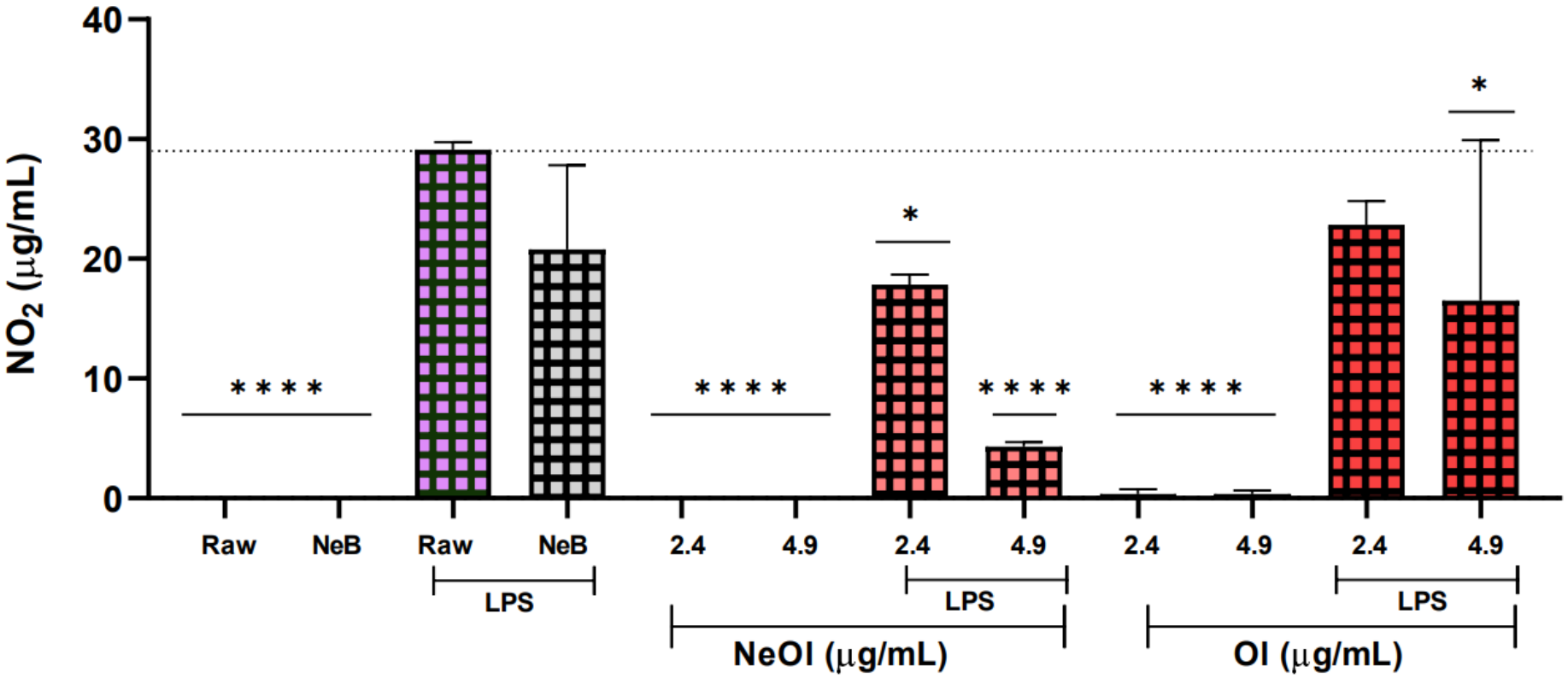

Figure 2.7. Effect of annatto oil (Ol) and annatto nanoemulsion (NeOl) on nitrite (NO_2^-) production by RAW 264.7 macrophages under irradiated conditions. Data are presented as mean ± SD (n = 3). Statistical significance: *p < 0.05, **p < 0.005, ***p < 0.001, ****p < 0.0001; ns = not significant.

As expected, stimulation with LPS induced a significant increase in nitrite production in untreated cells, confirming successful activation of the inflammatory pathway. The blank formulation (NeB) did not significantly alter nitrite levels when co-administered with LPS in either condition, demonstrating that the vehicle did not exert anti-inflammatory activity. In contrast, treatment with the curcumin-containing nanoemulsion (NeC) significantly reduced LPS-induced NO_2^- production at both concentrations tested (2.4 and 4.9 μg/mL of curcumin). This inhibitory effect was maintained in both irradiated and non-irradiated conditions, with nitrite levels close to baseline values, suggesting a potent suppressive effect of NeC on macrophage activation. Free curcumin (C) also reduced nitrite levels significantly at both concentrations tested. However, in irradiated conditions, its suppressive effect was less pronounced compared to NeC, particularly at the highest dose (4.9 μg/mL), where nitrite levels were noticeably higher than with the nanoformulation. These results indicate that nanoencapsulation enhances the anti-inflammatory activity of curcumin and may improve its responsiveness under photoactivation.

Regarding the annatto oil-based nanoemulsion (NeOl), a similar suppressive effect on NO_2^- production was observed (Figures 2.6 and 2.7). In both irradiated and non-irradiated conditions, NeOl significantly reduced LPS-induced nitrite levels in a dose-dependent manner, with stronger inhibition at the highest concentration tested (4.9 μg/mL). Free annatto oil (Ol) also decreased nitrite levels; however, its effect was milder and more variable, especially under irradiated conditions, where statistical significance was only observed at the highest dose. These results suggest that, as with curcumin, the nanoformulation of annatto oil improved the anti-inflammatory response, potentially enhancing bioavailability and cellular uptake. Notably, NeOl's inhibitory performance under irradiation was comparable to that of NeC, indicating promising potential for use in photoactivated therapies targeting chronic inflammation.

To ensure that the observed reductions in NO_2^- levels were not attributable to cytotoxic effects from the LED irradiation, a complementary MTT assay was performed to assess cell viability under all treatment conditions, including irradiated and non-irradiated samples. As shown in Figures 2.8 and 2.9, no significant differences in viability were observed between irradiated and non-irradiated groups across all treatment types and concentrations tested. These results confirm that the photobiomodulation protocol used

(blue LED, 1 min, post-treatment) did not compromise cell viability and therefore validates the subsequent immunomodulatory analyses.

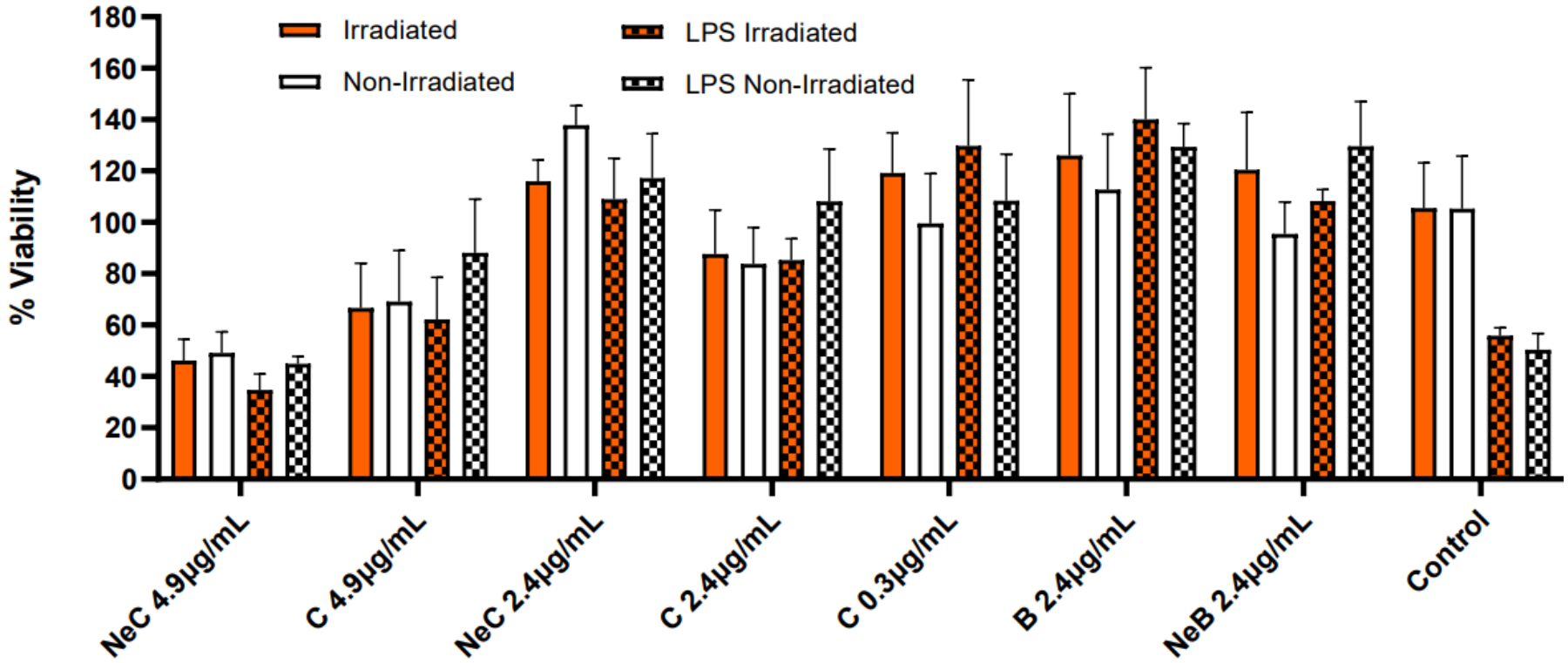

Figure 2.8. Cell viability (%) of RAW 264.7 macrophages treated with curcumin (C) or curcumin nanoemulsion (NeC), under irradiated and non-irradiated conditions. No significant cytotoxicity was observed between matched groups. Concentrations expressed in µg/mL of pure curcumin. Statistical analysis: two-way ANOVA followed by Sidak's multiple comparisons test (GraphPad Prism 8.0.1); $p > 0.05$.

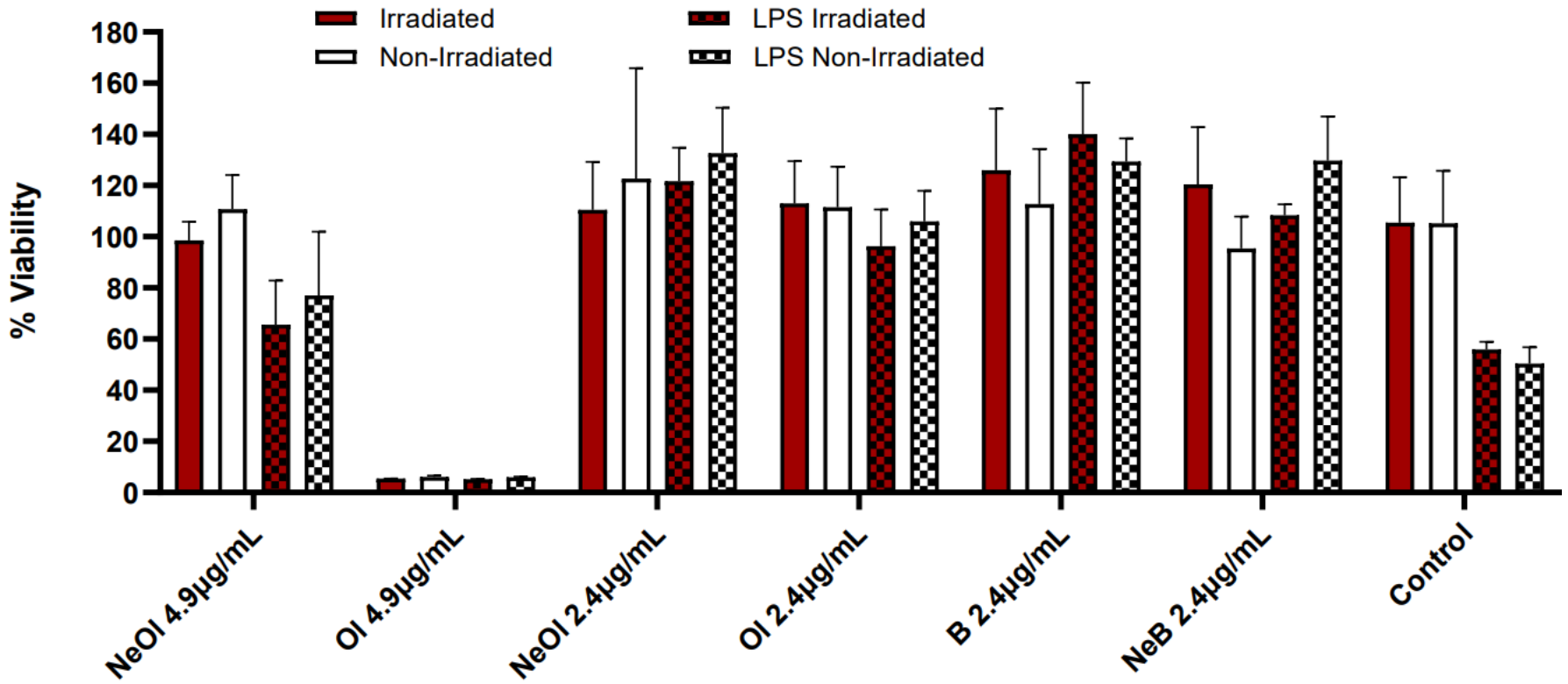

Figure 2.9. Cell viability (%) of RAW 264.7 macrophages treated with annatto oil (Ol) or annatto nanoemulsion (NeOl), under irradiated and non-irradiated conditions. No significant cytotoxicity was observed between matched groups. Concentrations expressed in µg/mL of pure curcumin. Statistical analysis: two-way ANOVA followed by Sidak's multiple comparisons test (GraphPad Prism 8.0.1); $p > 0.05$.

2.3.4 Cytokine Profiling: TNF-α and IL-10 Quantification (ELISA)

Following confirmation of non-cytotoxicity under photoactivation conditions (Figures 2.8 and 2.9), the immunomodulatory potential of the formulations was further investigated by quantifying pro- and anti-inflammatory cytokines in LPS-stimulated RAW 264.7 macrophages. TNF-α and IL-10 levels were assessed under both irradiated and non-irradiated conditions after 24 h of treatment with nanoencapsulated or free forms of curcumin and annatto oil (Figures 2.10-2.13 and 2.14-2.17).

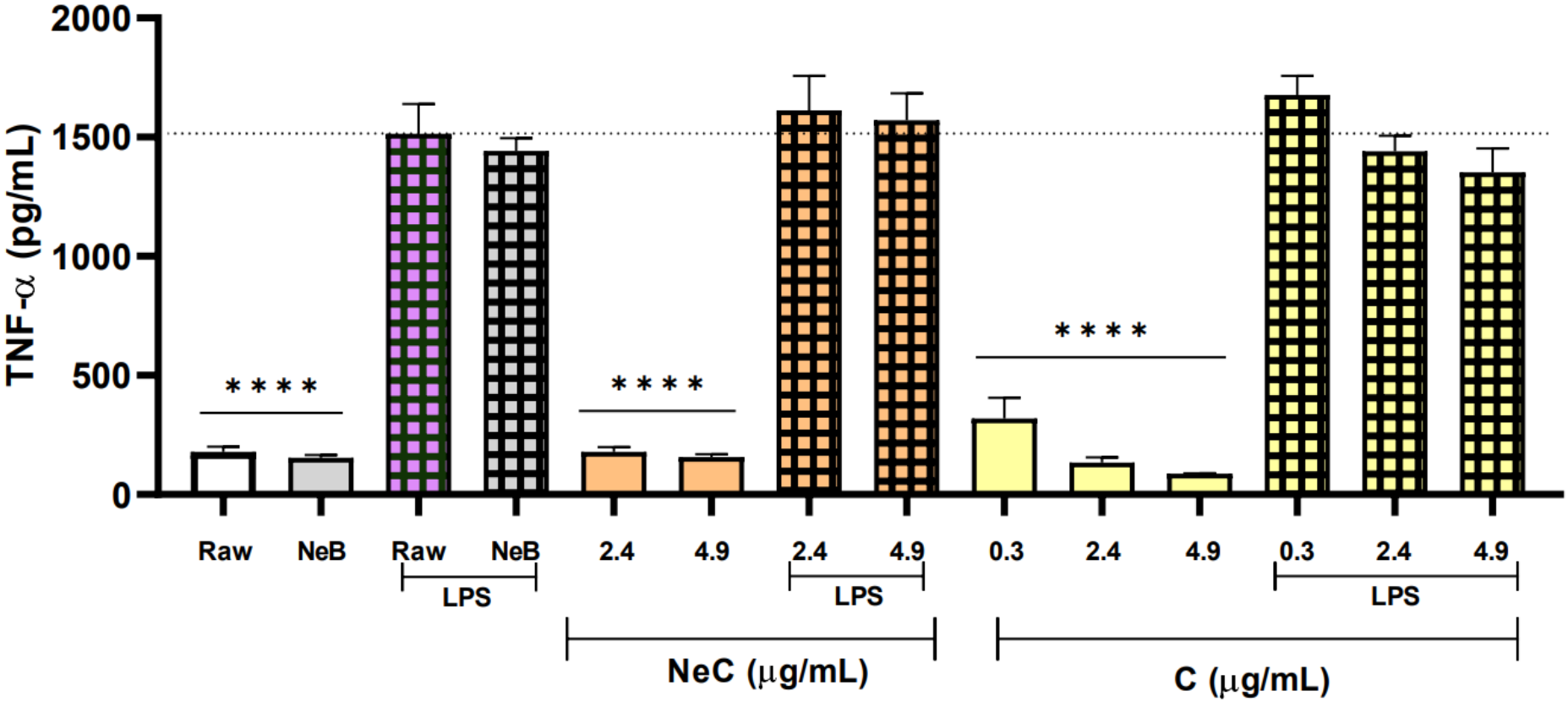

Figure 2.10. TNF-α levels (pg/mL) in RAW 264.7 macrophages after 24 h of treatment with curcumin (C) or curcumin nanoemulsion (NeC), under non-irradiated conditions. Data are presented as mean ± SD (n = 3). Statistical analysis: one-way ANOVA followed by Tukey's post hoc test; ****$p < 0.0001$.

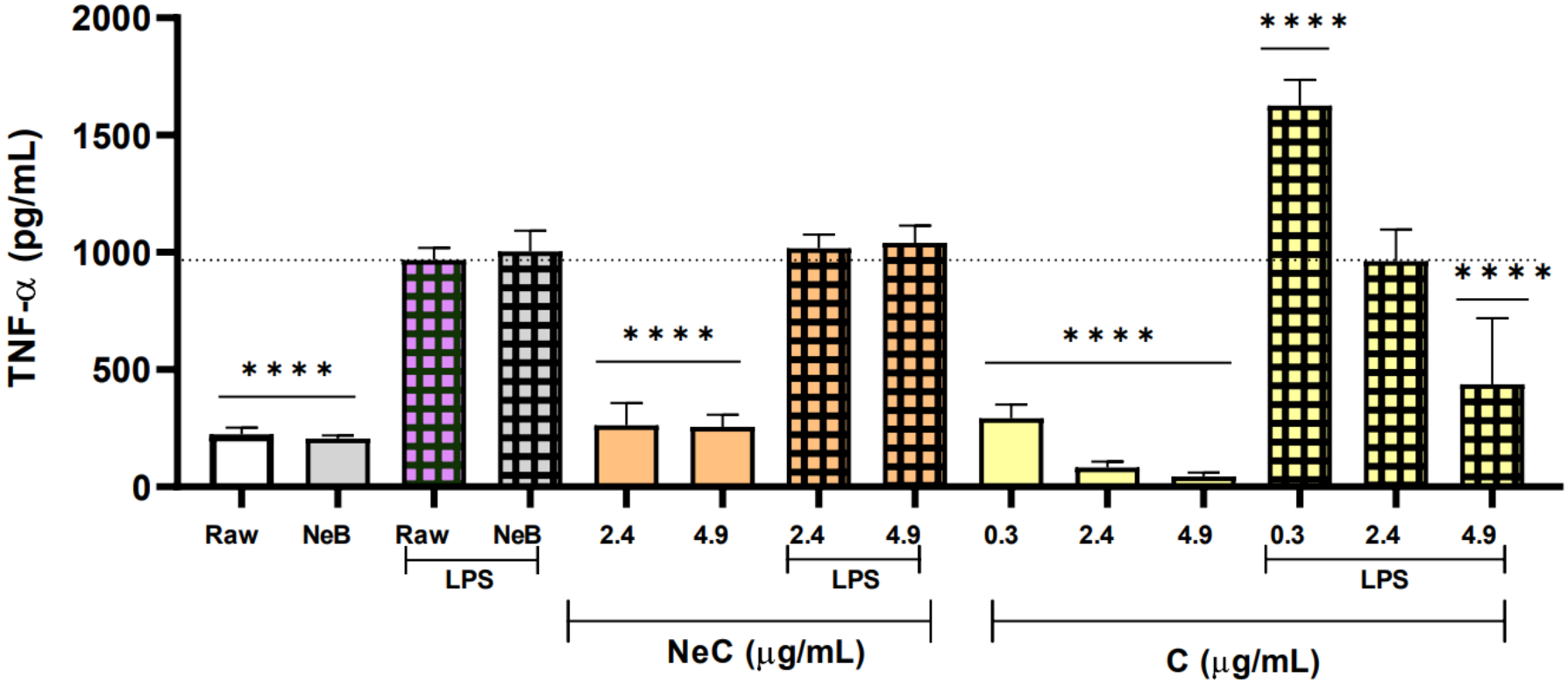

Figure 2.11. TNF-α levels (pg/mL) in RAW 264.7 macrophages after 24 h of treatment with curcumin (C) or curcumin nanoemulsion (NeC), under irradiated conditions. Data are presented as mean ± SD (n = 3). Statistical analysis: one-way ANOVA followed by Tukey's post hoc test; ****$p < 0.0001$.

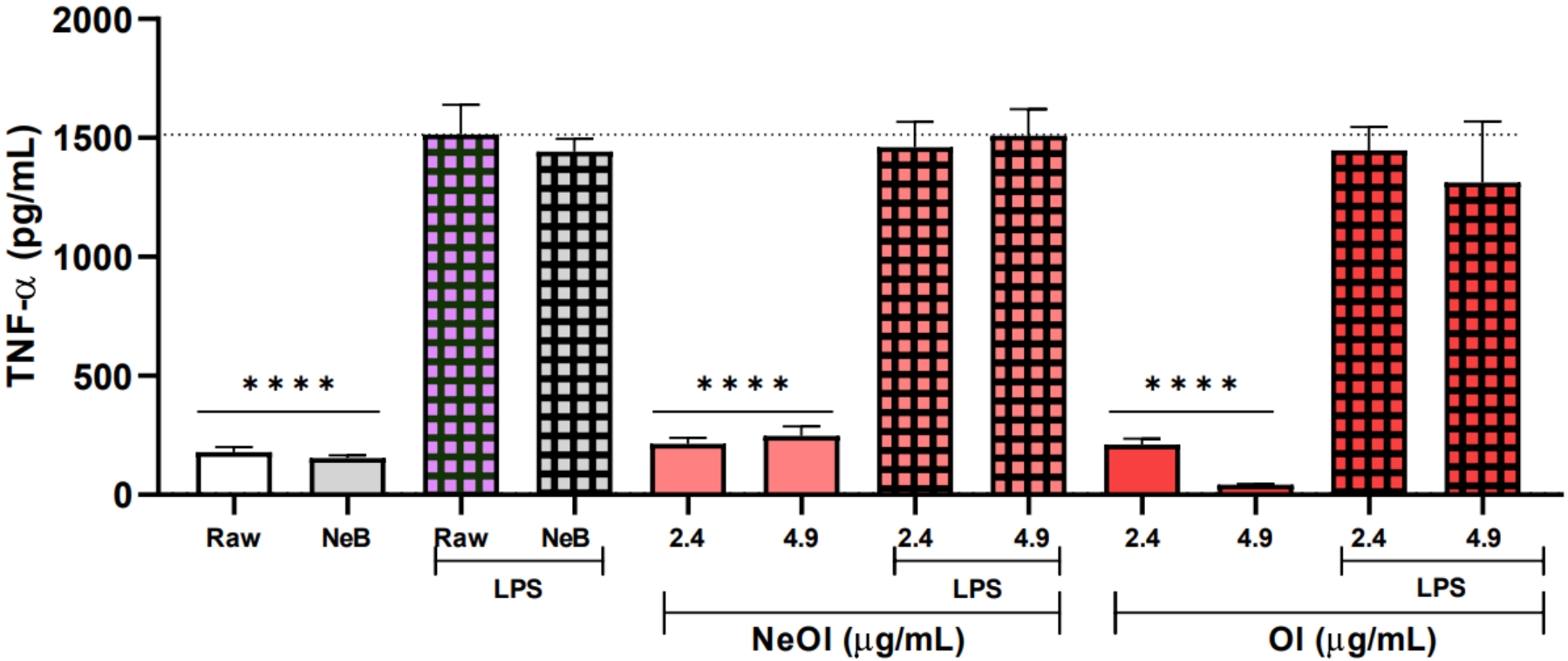

Figure 2.12. TNF-α levels (pg/mL) in RAW 264.7 macrophages after 24 h of treatment with annatto oil (Ol) or annatto nanoemulsion (NeOl), under non-irradiated conditions. Data are presented as mean ± SD (n = 3). Statistical analysis: one-way ANOVA followed by Tukey's post hoc test; ****$p < 0.0001$.

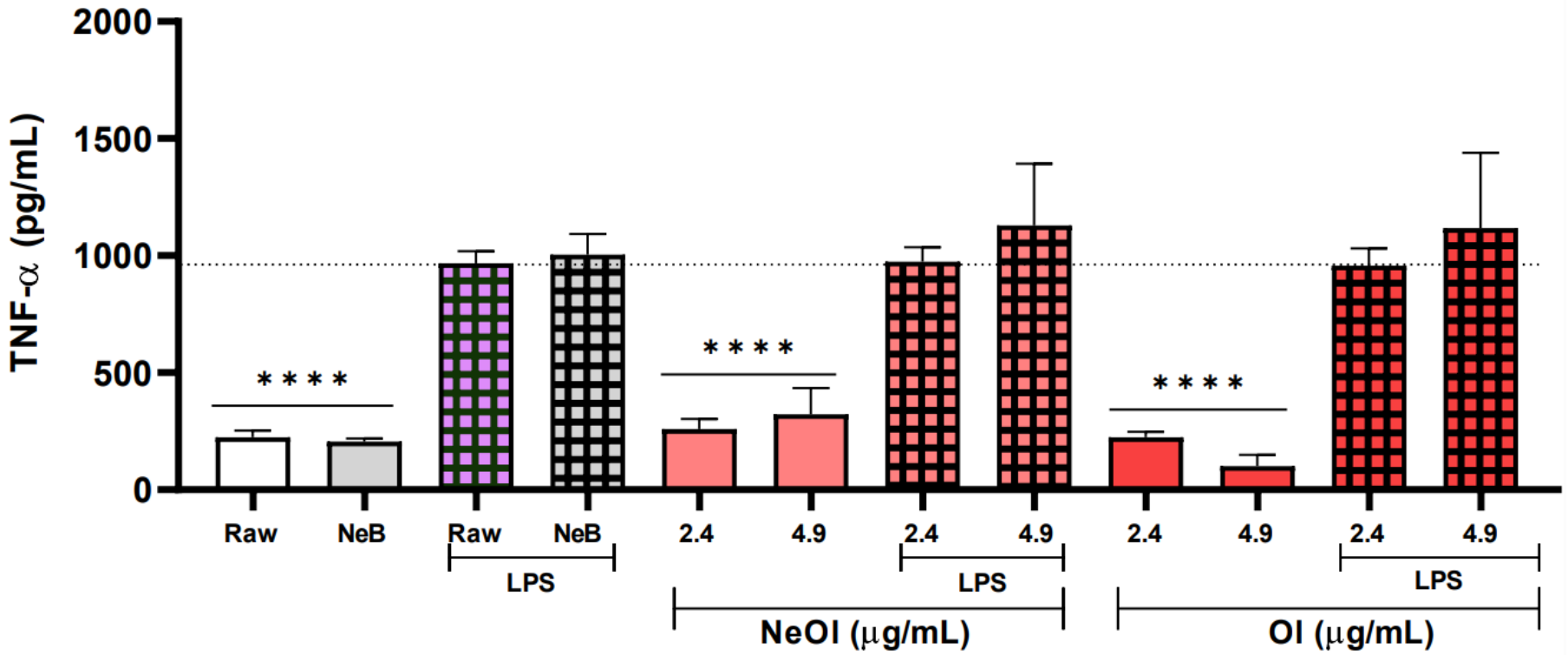

Figure 2.13. TNF-α levels (pg/mL) in RAW 264.7 macrophages after 24 h of treatment with annatto oil (Ol) or annatto nanoemulsion (NeOl), under irradiated conditions. Data are presented as mean ± SD (n = 3). Statistical analysis: one-way ANOVA followed by Tukey's post hoc test; ****$p < 0.0001$.

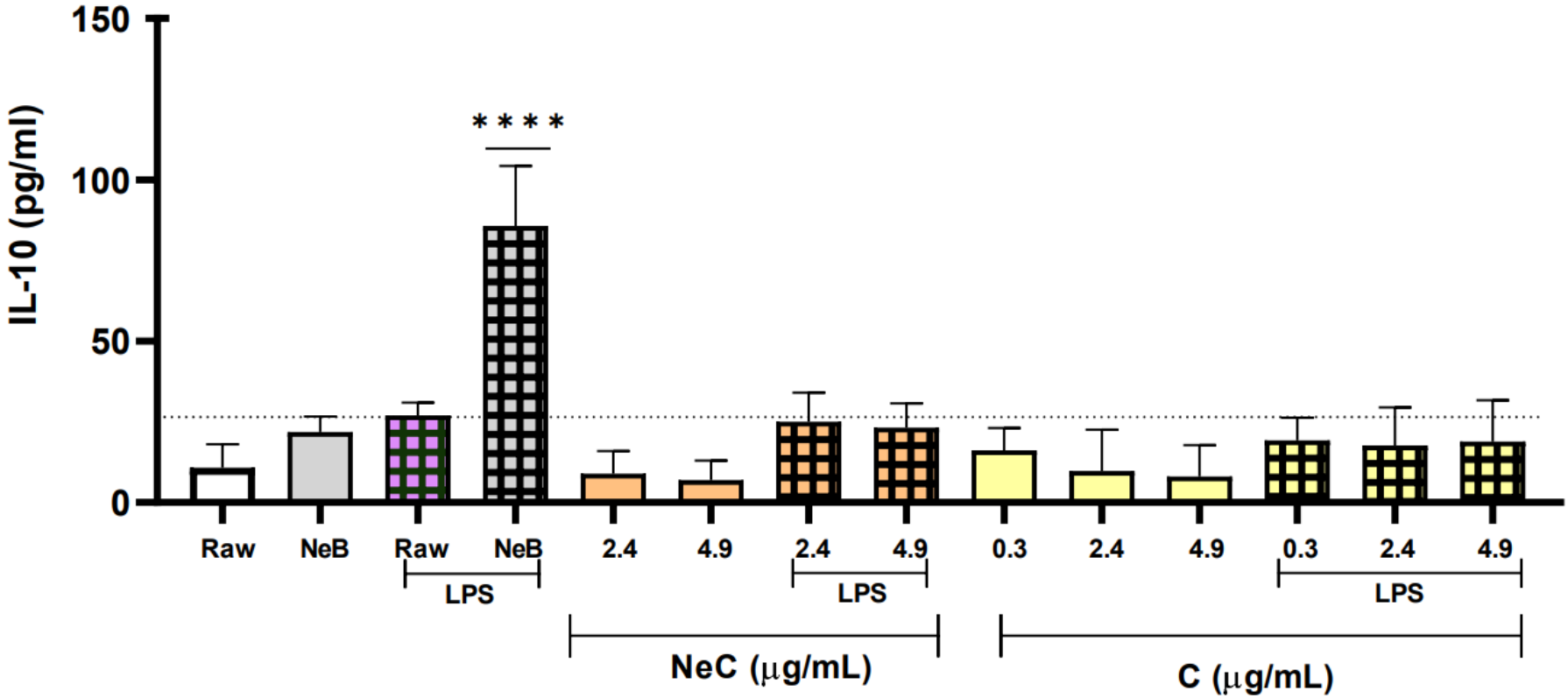

Figure 2.14. IL-10 levels (pg/mL) in RAW 264.7 macrophages after 24 h of treatment with curcumin (C) or curcumin nanoemulsion (NeC), under non-irradiated conditions. Data are presented as mean ± SD (n = 3). Statistical analysis: one-way ANOVA followed by Tukey's post hoc test; ****$p < 0.0001$.

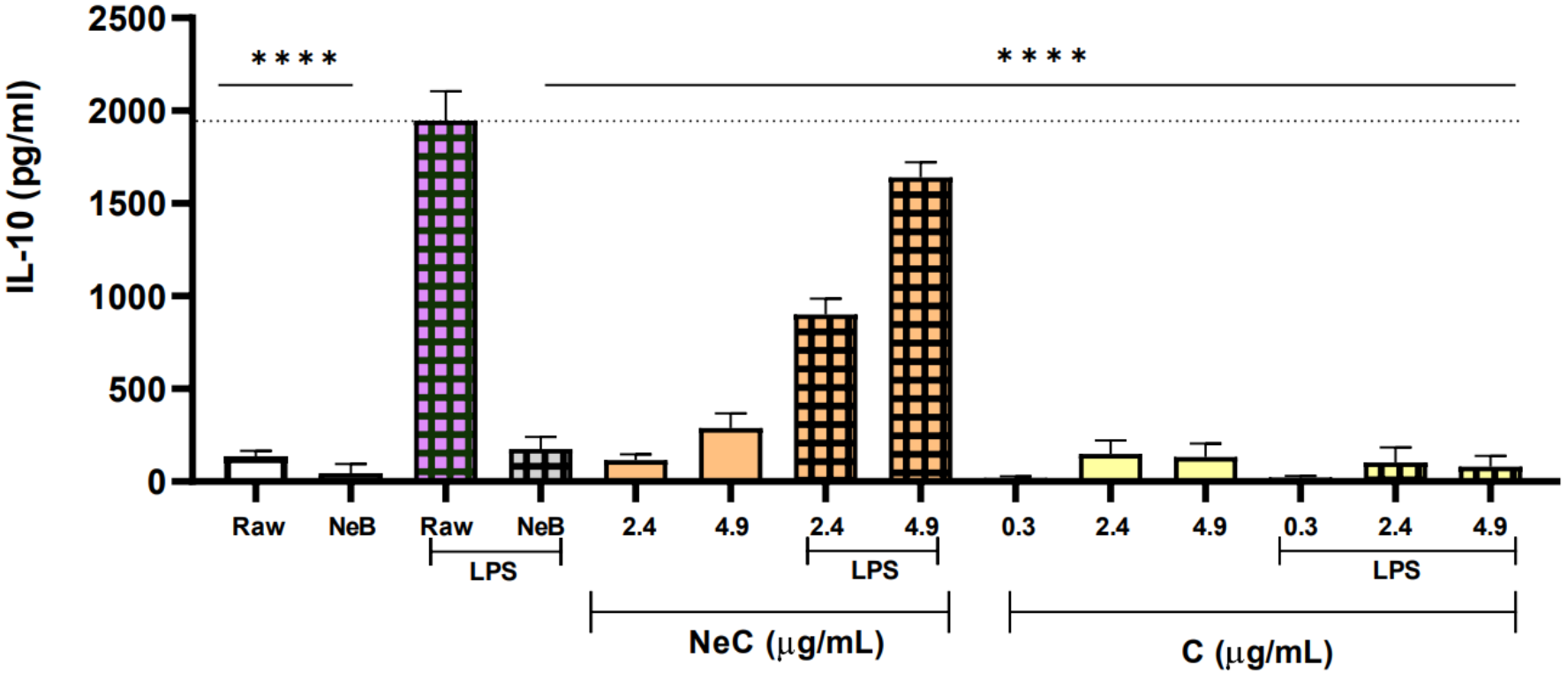

Figure 2.15. IL-10 levels (pg/mL) in RAW 264.7 macrophages after 24 h of treatment with curcumin (C) or curcumin nanoemulsion (NeC), under irradiated conditions. Data are presented as mean ± SD (n = 3). Statistical analysis: one-way ANOVA followed by Tukey's post hoc test; ****$p < 0.0001$.

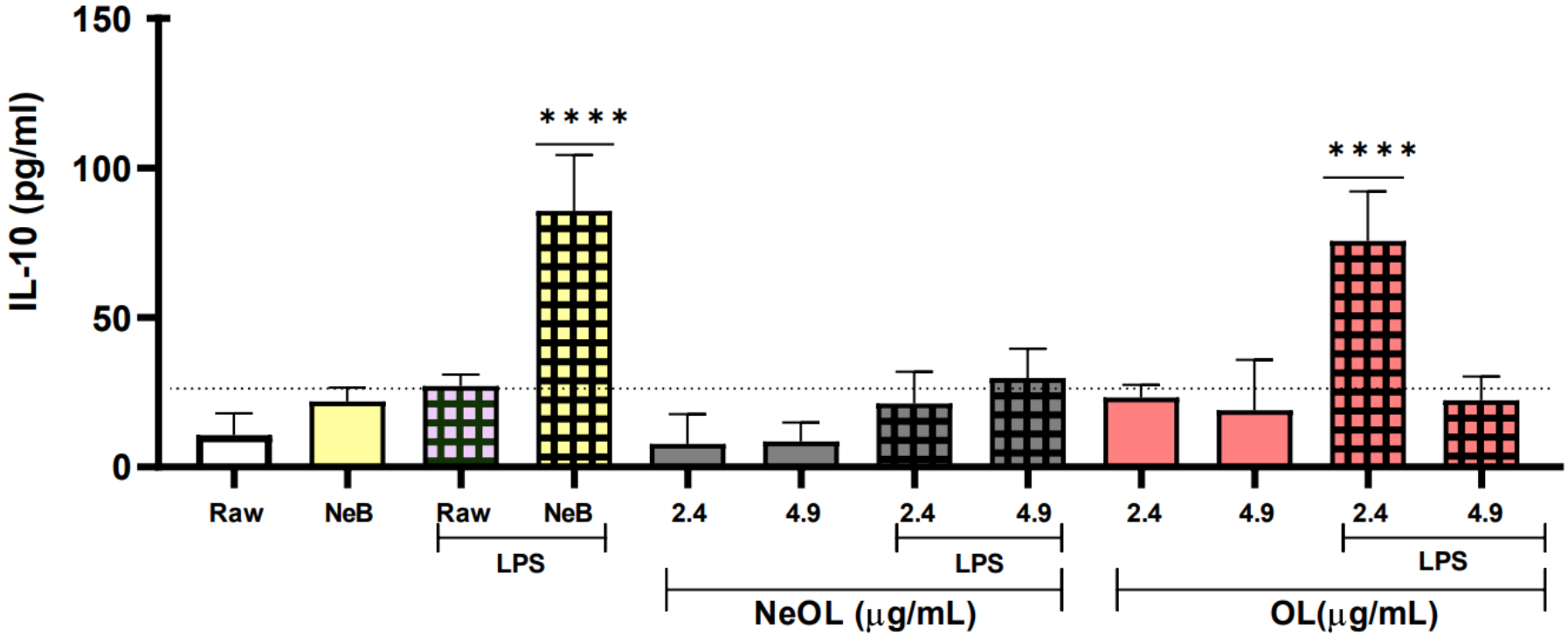

Figure 2.16. IL-10 levels (pg/mL) in RAW 264.7 macrophages after 24 h of treatment with annatto oil (Ol) or annatto nanoemulsion (NeOl), under non-irradiated conditions. Data are presented as mean ± SD (n = 3). Statistical analysis: one-way ANOVA followed by Tukey's post hoc test; ****$p < 0.0001$.

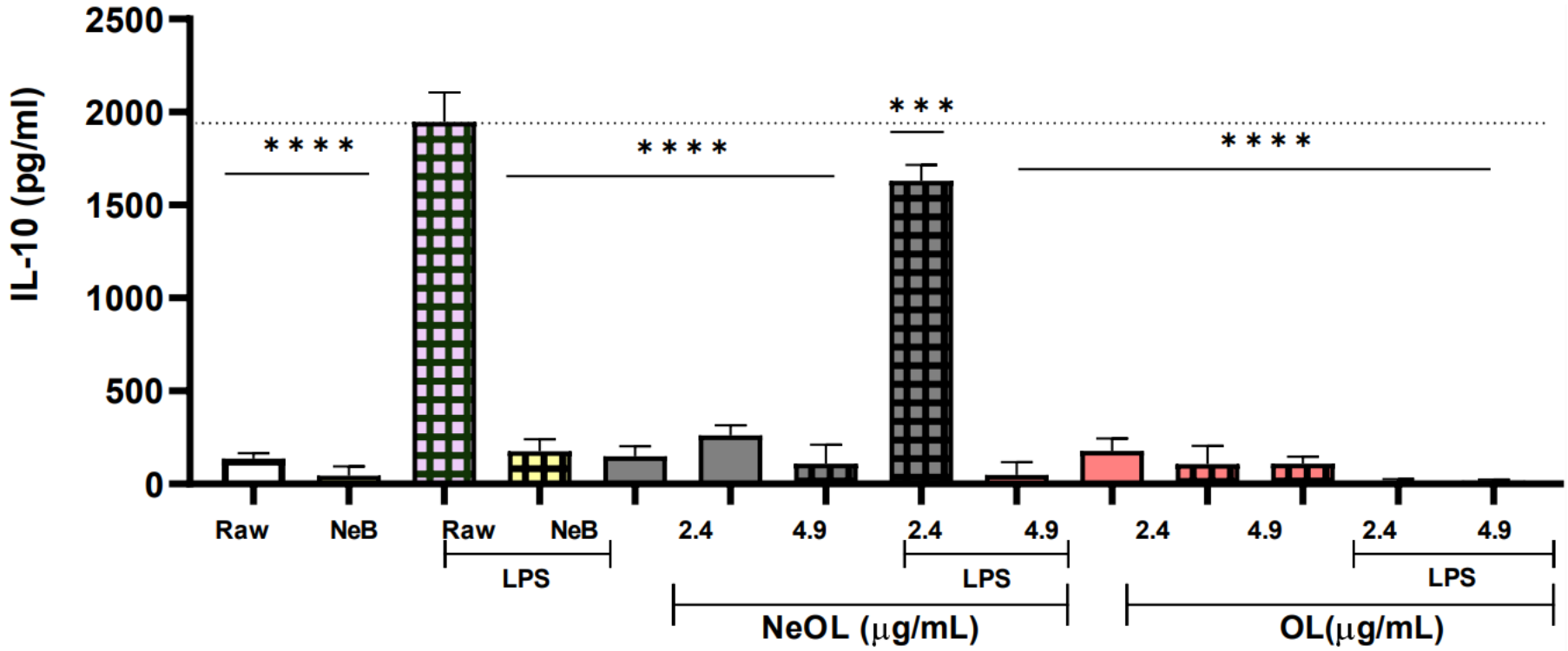

Figure 2.17. IL IL-10 levels (pg/mL) in RAW 264.7 macrophages after 24 h of treatment with annatto oil (Ol) or annatto nanoemulsion (NeOl), under irradiated conditions. Data are presented as mean ± SD (n = 3). Statistical analysis: one-way ANOVA followed by Tukey's post hoc test; ****$p < 0.0001$.

As shown in Figures 2.10-2.13, LPS stimulation led to a significant increase in TNF-α secretion, confirming the activation of the inflammatory pathway. Treatment with either nanoencapsulated curcumin (NeC) or free curcumin (C) at 2.4 or 4.9 μg/mL did not significantly reduce TNF-α levels under non-irradiated conditions. However, under LED irradiation, a significant reduction was observed in the group treated with free curcumin at 4.9 μg/mL, suggesting a potential photoenhanced effect (Figure 2.11). Moreover, both irradiated curcumin- and annatto-based formulations showed a visible tendency toward reduced TNF-α levels when compared to their non-irradiated counterparts.

In the case of annatto oil-based formulations, neither nanoencapsulated annatto oil (NeOl) nor free annatto oil (Ol) significantly reduced TNF-α production in LPS-stimulated macrophages under either irradiated or non-irradiated conditions (Figures 2.12 and 2.13). Despite a trend toward lower cytokine levels compared to LPS-only controls, statistical significance was not achieved at either concentration tested (2.4 or 4.9 μg/mL). These results suggest that, under the conditions evaluated, annatto oil does not exert a substantial inhibitory effect on TNF-α secretion, regardless of nanoencapsulation or photoactivation.

IL-10 levels remained low across all tested conditions (Figures 2.14-2.17). No significant increase in IL-10 secretion was detected in response to treatment with either NeC or C, nor with NeOl or Ol, under LPS-stimulated conditions, regardless of irradiation. Still, under blue LED exposure, a reproducible upward trend in IL-10 secretion was observed across nanoemulsion-treated groups, reinforcing a tendency toward an anti-inflammatory profile despite the absence of statistical significance. Overall, the absence of IL-10 upregulation reinforces that the observed anti-inflammatory effects were not mediated by a compensatory increase in this cytokine.

Taking together, these cytokine profiles indicate that the tested formulations did not exert their effects through IL-10 induction or consistent TNF-α suppression. The only significant decrease in TNF-α levels was observed with irradiated free curcumin at the highest concentration, while no substantial modulation was seen with the nanoemulsions or annatto-based treatments. Nevertheless, the overall pattern under irradiation suggests a shift toward reduced TNF-α and increased IL-10, supporting a tendency toward an anti-inflammatory profile.

These findings, combined with the marked inhibition of NO_2^- production (Figure 3.1-3.4), suggest that the partial anti-inflammatory activity observed may be primarily associated with the downregulation of nitric oxide pathways rather than cytokine modulation.

These findings are consistent with previous studies reporting that curcumin nanoformulations can enhance cellular uptake and bioactivity compared to the free compound [33,34] Although the modulation of TNF-α and IL-10 was limited, the strong suppression of nitric oxide aligns with reports indicating that nitrite quantification is a reliable indicator of inducible nitric oxide synthase (iNOS) inhibition in RAW 264.7 macrophages [35]. Furthermore, the improved response observed under blue LED exposure with free curcumin supports the hypothesis of photoenhanced anti-inflammatory action, as demonstrated in photodynamic therapy models applied to wound healing [36]. Notably, our results expand upon the work of Santana et al. (2023), who demonstrated the therapeutic efficacy of latex-based curcumin delivery systems by providing in vitro mechanistic evidence of nitric oxide pathway modulation [26]. To our knowledge, this is the first report demonstrating such effects for nanoemulsions containing annatto oil, highlighting their potential as novel phytotherapeutic agents in photoresponsive therapies.

4.4 CONCLUSION

The present study demonstrated that nanoemulsions containing curcumin and annatto oil are biocompatible with RAW 264.7 macrophages, as confirmed by MTT assays showing no reduction in cell viability at tested concentrations. Physicochemical characterization revealed particle sizes compatible with nano-scale delivery; however, the relatively high polydispersity index (PDI) suggests heterogeneity in particle distribution, which may compromise formulation stability and reproducibility in future applications.

Notably, a marked reduction in nitrite (NO_2^-) levels was observed in both irradiated and non-irradiated conditions, particularly with curcumin-based nanoemulsions. This effect is consistent with partial inhibition of inducible nitric oxide synthase (iNOS), a key pro-inflammatory enzyme activated by LPS in macrophages. These findings point toward a potential anti-inflammatory mechanism mediated via NO modulation.

Under photoactivation with blue LED irradiation, the formulations showed a trend toward reduced TNF-α secretion and increased IL-10 release when compared to their non-irradiated counterparts. This tendency suggests that light exposure may potentiate the immunomodulatory effects of the formulations, favoring a shift in macrophage responses toward a more anti-inflammatory profile.

Taken together, these results indicate that although the formulations show promise in reducing nitric oxide production — a critical mediator of oxidative stress — further optimization of composition and nanoemulsion homogeneity is necessary. Future studies should explore alternative surfactant ratios, extended dose ranges, and additional inflammatory markers (e.g., IL-6, COX-2, iNOS protein levels) to fully characterize the immunomodulatory potential of these photoresponsive phytotherapeutic systems.

4.5 REFERENCES

[1] R. L. Thomas, S. Halim, S. Gurudas, S. Sivaprasad, and D. R. Owens, “IDF Diabetes Atlas: A review of studies utilising retinal photography on the global prevalence of diabetes related retinopathy between 2015 and 2018,” *Diabetes Res Clin Pract*, vol. 157, p. 107840, 2019, doi: 10.1016/j.diabres.2019.107840.

[2] L. P. Araújo, A. V. Carvalho, A. G. Carneiro, C. R. Oliveira, M. L. da Silva, and G. F. Ghesti, “Avaliação Tecnológica de Dispositivo Cicatrizante para Pés Diabéticos com Capacidade de Neoformação Tecidual,” *Cadernos de Prospecção*, vol. 11, no. 3, p. 910, 2018, doi: 10.9771/cp.v11i3.27101.

[3] T. Fernandes Santana Gomes *et al.*, “A Natural Latex-Based Smart Dressing for Curcumin Delivery Combined with LED Phototherapy in Diabetic Foot Ulcers: A Pilot Clinical Study,” *Pharmaceutics*, vol. 17, p. 772, 2025, doi: 10.3390/pharmaceutics17060772.

[4] L. S. FERREIRA, “Efeito Terapêutico Do Uso Combinado De Biomembrana De Látex Natural Contendo Curcumina E Ledterapia (Dispositivo Terapêutico Rapha®) Em Portadores De Úlcera Diabética Luzia Sousa Ferreira,” 2021.

[5] J. E. P. de Oliveira and S. Vencio, “Diretrizes da sociedade brasileira de diabetes. São Paulo: Sociedade Brasileira de Diabetes, 2014. v. 2015,” *Nhk技研*, vol. 151, pp. 10–17, 2015.

[6] M.F. F. Rosa, S. M. F. Guimarães, A. G. Dominguez, Duarte, R. S. Assis, C. B. Reis, and S. de S. R. F. Rosa, “Desenvolvimento de tecnologia dura para tratamento do pé diabético: um estudo de caso na perspectiva da saúde coletiva,” pp. 87–100, 2019, doi: 10.1590/0103-11042019S207.

[7] T. F. Santana *et al.*, “Effect of exposure to a light-emitting diode (LED) on the physicochemical characteristics of natural latex biomembranes used to treat diabetic ulcers,” *Research on Biomedical Engineering*, vol. 38, no. 3, pp. 901–911, 2022, doi: 10.1007/s42600-022-00226-y.

[8] F. M. Silva *et al.*, “Curcumin and Papain-Loaded Liposomal Natural Latex Dressings with Phototherapy : A Synergistic Approach to Diabetic Wound Healing,” no. Dm, pp. 1–21, 2025.

[9] Y. Taniyama and K. K. Griendling, “Reactive Oxygen Species in the Vasculature: Molecular and Cellular Mechanisms,” *Hypertension*, vol. 42, no. 6, pp. 1075–1081, 2003, doi: 10.1161/01.HYP.0000100443.09293.4F.

[10] A. C. PINHEIRO, “AVALIAÇÃO DO EFEITO ANTI-INFLAMATÓRIO DE NANOEMULSÃO À BASE DE ÓLEO DE PEQUI (Caryocar brasiliense) EM MACRÓFAGOS in vitro,” 2023.

[11] J. L. Burgess, W. A. Wyant, B. A. Abujamra, R. S. Kirsner, and I. Jozic, “Diabetic Wound-Healing Science,” 2021.

[12] E. Tsourdi, A. Barthel, H. Rietzsch, A. Reichel, and S. R. Bornstein, “Current aspects in the pathophysiology and treatment of chronic wounds in diabetes mellitus,” 2013. doi: 10.1155/2013/385641.

[13] L. I. F. Moura, A. M. A. Dias, E. Carvalho, and H. C. De Sousa, “Recent advances on the development of wound dressings for diabetic foot ulcer treatment - A review,” *Acta Biomater*, vol. 9, no. 7, pp. 7093–7114, 2013, doi: 10.1016/j.actbio.2013.03.033.

[14] M. Piipponen, D. Li, and N. X. Landén, “The immune functions of keratinocytes in skin wound healing,” *Int J Mol Sci*, vol. 21, no. 22, pp. 1–26, 2020, doi: 10.3390/ijms21228790.

[15] T. Angela Maria Vicente, *Estratégias para o cuidado da pessoa com doença crônica: diabetes mellitus*, vol. 11, no. 1. 2013. [Online]. Available: http://scioteca.caf.com/bitstream/handle/123456789/1091/RED2017-Eng-8ene.pdf?sequence=12&isAllowed=y%0Ahttp://dx.doi.org/10.1016/j.regsciurbeco.2008.06.005%0Ahttps://www.researchgate.net/publication/305320484_SISTEM_PEMBETUNGAN_TERPUSAT_STRATEGI_MELESTARI

[16] L. G. Bertonhi and J. C. R. Dias, "Diabetes mellitus tipo 2 : aspectos clínicos , tratamento e conduta dietoterápica Type 2 Diabetes mellitus : clinical aspects , treatment and dietary management," *Revista Ciências Nutricionais Online*, vol. 2, pp. 1–10, 2018.

[17] S. S. R. F. Rosa *et al.*, "Regeneration of Diabetic Foot Ulcers Based on Therapy with Red LED Light and a Natural Latex Biomembrane," *Ann Biomed Eng*, vol. 47, no. 4, pp. 1153–1164, 2019, doi: 10.1007/s10439-019-02220-5.

[18] A. López-Delis *et al.*, "Characterization of the Cicatrization Process in Diabetic Foot Ulcers Based on the Production of Reactive Oxygen Species," *J Diabetes Res*, vol. 2018, no. Dm, 2018, doi: 10.1155/2018/4641364.

[19] M. Eugenia and R. Diaz, "Prevalencia de Neuropatía Periférica en una Unidad de Diabetes," *Revista Uruguaya de Medicina Interna*, vol. 05, no. 03, pp. 17–27, 2020, doi: 10.26445/05.02.3.

[20] S. S. R. F. Rosa *et al.*, "Regeneration of Diabetic Foot Ulcers Based on Therapy with Red LED Light and a Natural Latex Biomembrane," *Ann Biomed Eng*, vol. 47, no. 4, pp. 1153–1164, 2019, doi: 10.1007/s10439-019-02220-5.

[21] N. Somchit *et al.*, "Curcumin pyrazole blocks lipopolysaccharide-induced inflammation via suppression of JNK activation in RAW 264.7 macrophages," *Asian Pac J Allergy Immunol*, vol. 36, no. 3, pp. 184–190, 2018, doi: 10.12932/AP-130417-0073.

[22] M. K. Trivedi, S. C. Mondal, M. Gangwar, and S. Jana, "Immunomodulatory potential of nanocurcumin-based formulation," *Inflammopharmacology*, vol. 25, no. 6, pp. 609–619, 2017, doi: 10.1007/s10787-017-0395-3.

[23] V. A. Franklin, E. M. Bach Hi, N. S. Y. Wadt, and E. E. Bach, "Aqueous extract from urucum (Bixa orellana L.): antimicrobial, antioxidant, and healing activity," *Porto Biomed J*, vol. 8, no. 1, p. e183, Jan. 2023, doi: 10.1097/j.pbj.0000000000000183.

[24] Shahid-ul-Islam, L. J. Rather, and F. Mohammad, “Phytochemistry, biological activities and potential of annatto in natural colorant production for industrial applications – A review,” *J Adv Res*, vol. 7, no. 3, pp. 499–514, May 2016, doi: 10.1016/j.jare.2015.11.002.

[25] I. D. S. MONTEIRO, “Avaliação do potencial cicatrizante de nanoemulsões a base de andiroba (Carapa guianensis Aublet) in vitro.,” pp. 1–23, 2016.

[26] T. Fernandes Santana Gomes *et al.*, “A Natural Latex-Based Smart Dressing for Curcumin Delivery Combined with LED Phototherapy in Diabetic Foot Ulcers: A Pilot Clinical Study,” *Pharmaceutics*, vol. 17, p. 772, 2025, doi: 10.3390/pharmaceutics17060772.

[27] R. B. Silva, C. R. Almeida, J. M. Chavasco, and J. K. Chavasco, “Antimycobacterial activity evaluation and MIC determination of liophilizated hydroalcoholic extracts of Bixa orellana L., Bixaceae,” 2009.

[28] X. Lin *et al.*, “Curcumin attenuates oxidative stress in RAW264.7 cells by increasing the activity of antioxidant enzymes and activating the Nrf2-Keap1 pathway,” *PLoS One*, vol. 14, no. 5, pp. 1–13, 2019, doi: 10.1371/journal.pone.0216711.

[29] Y. Wu *et al.*, “Effects of FM0807, a novel curcumin derivative, on lipopolysaccharide-induced inflammatory factor release via the ROS/JNK/p53 pathway in RAW264.7 cells,” *Biosci Rep*, vol. 38, no. 5, pp. 1–10, 2018, doi: 10.1042/BSR20180849.

[30] B. N. Nayak, G. Kaur, and H. S. Buttar, “TNF-α modulation by natural bioactive molecules in mouse RAW 264.7 macrophage cells,” *J Complement Integr Med*, vol. 13, no. 1, pp. 1–7, 2016, doi: 10.1515/jcim-2015-0024.

[31] J. C. Barry *et al.*, “Hyporesponsiveness to the anti-inflammatory action of interleukin-10 in type 2 diabetes,” *Sci Rep*, vol. 6, pp. 1–9, 2016, doi: 10.1038/srep21244.

[32] J. Y. Lin and C. Y. Tang, “Interleukin-10 administration inhibits TNF-α and IL-1β, but not IL-6, secretion of LPS-stimulated peritoneal macrophages,” *J Food Drug Anal*, vol. 15, no. 1, pp. 48–54, 2007, doi: 10.38212/2224-6614.2441.

[33] W. Zhang *et al.*, “Effects of morphology and size of nanoscale drug carriers on cellular uptake and internalization process: a review,” *RSC Adv*, vol. 13, no. 1, pp. 80–114, 2022, doi: 10.1039/d2ra06888e.

[34] U. Gandapu, R. K. Chaitanya, G. Kishore, R. C. Reddy, and A. K. Kondapi, “Curcumin-loaded apotransferrin nanoparticles provide efficient cellular uptake and effectively inhibit HIV-1 replication In Vitro,” *PLoS One*, vol. 6, no. 8, 2011, doi: 10.1371/journal.pone.0023388.

[35] W. Punfa, S. Yodkeeree, P. Pitchakarn, C. Ampasavate, and P. Limtrakul, “Enhancement of cellular uptake and cytotoxicity of curcumin-loaded PLGA nanoparticles by conjugation with anti-P-glycoprotein in drug resistance cancer cells,” *Acta Pharmacol Sin*, vol. 33, no. 6, pp. 823–831, 2012, doi: 10.1038/aps.2012.34.

[36] S. Cheenpracha, E. J. Park, B. Rostama, J. M. Pezzuto, and L. C. Chang, “Inhibition of nitric oxide (NO) production in lipopolysaccharide (LPS)-activated murine macrophage RAW 264.7 cells by the norsesterterpene peroxide, epimuqubilin A,” *Mar Drugs*, vol. 8, no. 3, pp. 429–437, 2010, doi: 10.3390/md8030429.

[37] T. Niu, Y. Tian, Q. Cai, Q. Ren, and L. Wei, “Red light combined with blue light irradiation regulates proliferation and apoptosis in skin keratinocytes in combination with low concentrations of curcumin,” *PLoS One*, vol. 10, no. 9, pp. 1–18, 2015, doi: 10.1371/journal.pone.0138754.

This chapter presents a scientific article for submission to a journal in the Engineering IV area (CAPES). It describes the development of a 3D bioprinted triculture model of PDAC, aiming to improve tumor modeling and support future integration with a microfluidic platform.

3 PAPER 2

3D Bioprinting of a Triculture Pancreatic Tumor Model for Organ-on-a-Chip Applications

Lucas Meyer Syllos[1]*, Marcella Lemos Brettas Carneiro[2], Halima Alem-Marchand[3].

[1] Postgraduate Program in Bioengineering, University of Brasília, Brazil.

[2] Laboratory of Bioactive Compounds and Nanobiotechnology (LBCNano), Faculty of Ceilândia, University of Brasilia.

[3] Université de Lorraine, CNRS, Institut Jean Lamour, Nancy, France.

*Corresponding author: halima.alem@univ-lorraine.fr

Abstract

Pancreatic ductal adenocarcinoma (PDAC) remains one of the most lethal malignancies worldwide, with limited therapeutic options and a highly immunosuppressive tumor microenvironment that contributes to drug resistance. Given the limitations of conventional 2D cultures in replicating the complexity of the PDAC tumor microenvironment, we developed a 3D bioprinted triculture model of PDAC incorporating epithelial tumor cells (Panc-1), cancer-associated fibroblasts (MeWo), and THP-1-derived macrophages embedded in a gelatin–alginate hydrogel. The constructs were fabricated using extrusion-based bioprinting and maintained in culture for five days, a period selected to match the cytotoxic window of standard chemotherapeutics such as FOLFIRINOX and gemcitabine. Cell viability was assessed using live/dead assays and confocal imaging. There was a gradual decline from 73.4% on day 1 to 57.2% on day 5, with the formation of cell aggregates that favor more realistic tumor-stroma-immune interactions. This approach demonstrated high reproducibility and low cost, generating 48 constructs in under four hours without requiring specialized supplements. The inclusion of immune-like cells and the feasibility of maintaining the constructs with standard media highlight the potential of this model as a platform for high-throughput drug screening and disease modeling. Future

integration with organ-on-chip microfluidic systems could further enhance its physiological relevance and accelerate translational pancreatic cancer research.

Keywords: 3D bioprinting; pancreatic ductal adenocarcinoma (PDAC); tumor microenvironment; triculture model; macrophages; bioink.

3.1 INTRODUCTION

Pancreatic ductal adenocarcinoma (PDAC) is one of the most lethal malignancies worldwide, ranking among the leading causes of cancer-related mortality[1,2]. Its poor prognosis is mainly due to aggressive growth, resistance to conventional therapies, and late-stage diagnosis, which collectively limit treatment efficacy [3]. The tumor microenvironment in PDAC is particularly complex and immunosuppressive [4], characterized by a dense desmoplastic stroma and extensive cellular heterogeneity, including cancer-associated fibroblasts (CAFs) and tumor-associated macrophages (TAMs) [5,6]. These features strongly contribute to therapeutic failure and disease progression [5,7]. While fibroblasts have been increasingly incorporated into PDAC models, immune-like components remain underrepresented in current bioprinting approaches [4]. Their inclusion is critical to recapitulate early immune–stromal–epithelial interactions.

Traditional two-dimensional (2D) culture models fail to reproduce the complex architecture and cell–cell interactions of the pancreatic tumor microenvironment [8], often leading to poor predictivity in drug screening and translational studies [9]. In contrast, three-dimensional (3D) culture systems, including bioprinted constructs, can better mimic in vivo conditions by supporting more realistic spatial organization, extracellular matrix interactions, and nutrient or oxygen gradients [10,11]. Incorporating multiple cell types into 3D models, such as CAFs and immune cells, further enhances their physiological relevance, enabling a more faithful recapitulation of tumor behavior and drug response [12]. In this context, extrusion-based bioprinting emerges as a versatile technology for fabricating complex tumor models suitable for integration with organ-on-a-chip platforms, with technical parameters such as pressure, speed, and crosslinking still requiring optimization [13].

Based on these considerations, we developed an advanced preclinical 3D tumor model using extrusion-based bioprinting to co-culture three key cell types: (i) pancreatic cancer cells (Panc-1), (ii) MeWo fibroblasts, used here as cancer-associated fibroblasts (CAFs), and (iii) human monocyte leukemia THP-1-derived macrophages. These cells were embedded in a gelatin–alginate hydrogel, printed at 37 °C to better replicate the PDAC tumor microenvironment. The gelatin–alginate bioink was chosen over GelMA for its biocompatibility — eliminating the need for UV cross-linking — and for supporting cell viability, formulation versatility, and cost-effectiveness [14]. This 3D bioprinted triculture model represents a significant step toward the development of preclinical platforms for testing novel therapeutic strategies against pancreatic and other types of cancer. In the following sections, we present its preparation, printing process, and preliminary characterization over a five-day culture period.

3.2 MATERIALS AND METHODS

3.2.1 Reagents and Cell Lines

The extrusion-based 3D bioprinter BioX, equipped with three interchangeable printheads (Cellink, USA), was used for all experiments. Sodium alginate, gelatin (type B, bovine origin), calcium chloride, and sodium citrate were obtained from Sigma-Aldrich (St. Louis, MO, USA). Three different cell lines were employed: Panc-1 (pancreatic ductal adenocarcinoma, ATCC CRL-1469), MeWo fibroblasts derived from human melanoma (ATCC HTB-65™), and THP-1 human monocytic leukemia cells (ATCC TIB-202™).

Culture media and supplements, including Dulbecco's Modified Eagle Medium (DMEM), Minimum Essential Medium (MEM), Roswell Park Memorial Institute 1640 Medium (RPMI-1640), fetal bovine serum (FBS, Cat. No. F7524), Trypsin-EDTA, penicillin–streptomycin, amphotericin B, L-glutamine, Dulbecco's phosphate-buffered saline (DPBS), and sodium pyruvate, were purchased from Sigma-Aldrich. The Live/Dead Viability/Cytotoxicity Kit and Accutase detachment solution were purchased from Thermo Fisher Scientific. Phorbol 12-myristate 13-acetate (PMA) was also obtained from Sigma-Aldrich.

3.2.2 Cell Culture

Panc-1 cells were maintained in DMEM supplemented with 10% (v/v) fetal bovine serum (FBS), 2 mM L-glutamine, 1% penicillin–streptomycin, 0.05% amphotericin B, and 1 mM sodium pyruvate, and seeded at an initial density of 1–2 × 10^6 cells per T75 flask. MeWo cells were maintained in MEM with identical supplementation and seeded at 1–2 × 10^6 cells per T75 flask. THP-1 cells were cultured in RPMI-1640 supplemented with 10% (v/v) FBS, 2 mM L-glutamine, 1% penicillin–streptomycin, and 0.05% amphotericin B, and seeded at 0.5–1 × 10^6 cells per T75 flask. All cell lines were expanded in T75 culture flasks (Corning, USA) at 37 °C in a humidified 5% CO_2 atmosphere and subcultured twice per week at a split ratio of 1:3, corresponding to an approximate density of 5 × 10^4 cells/mL after each passage. For 3D bioprinting experiments, cells were used between passages 5 and 10 to ensure consistent growth and phenotype.

3.2.3 THP-1 Differentiation

THP1 cells were seeded at an initial density of 6–10 × 10^6 cells per T75 flask in RPMI-1640 medium supplemented as described above. Differentiation into macrophage-like phenotype (M0) was induced by adding 100 ng/mL phorbol 12-myristate 13-acetate (PMA) to the culture medium, followed by incubation for 48 hours at 37 °C in a humidified 5% CO_2 atmosphere. After differentiation, cells were gently detached using Accutase (Thermo Fisher Scientific) for 10–15 minutes at 37 °C, with mild pipetting to ensure complete detachment. The collected macrophages were resuspended in fresh medium and immediately used for bioink preparation.

3.2.4 Tumor Mass Design

The tumor model was designed as cylindrical constructs with a diameter of 6 mm and a height of 1.5 mm. The geometry was created using the One Shape online CAD software (One Shape, France) for precise digital modeling and subsequently exported to the BioX bioprinter's G-code database to guide the layer-by-layer fabrication process. This cylindrical shape was chosen to favor uniform nutrient and oxygen diffusion, while also facilitating downstream histological analysis. The complete set of bioprinting parameters applied in this study — including nozzle gauge, temperature, pressure, and printing speed — were selected in line with the work of Baka et al. (2023) on multicellular tumor constructs [14], and are summarized in Table 3.1 below.

Table 3.1. Parameters for the Bioprinting Process.

Parameter	Corresponding Value
Internal diameter of the printed needle	23 G (0.66mm)
Printhead temperature	37 ºC
Printing bed temperature	8 ºC
Extrusion pressure	10-20 kPa
Printhead movement speed	5-10 $mm.s^{-1}$

3.2.5 Bioink Preparation and Bioprinting

Herein, the term "bioink" refers to the hydrogel supplemented with cells. For preparation, gelatin (0.75 g) and sodium alginate (0.1 g) were weighed, sterilized under UV light (254 nm) for 60 minutes, and dissolved in the appropriate culture medium to reach a final concentration of 15% (w/v) gelatin and 2% (w/v) sodium alginate. The hydrogel solution was maintained under sterile conditions with magnetic stirring at 37 °C overnight.

On the following day, Panc-1, MeWo, and THP-1-derived macrophages were trypsinized, resuspended in their respective media, and incorporated into the hydrogel in a 1:2:4 ratio, resulting in approximately 2.2 million Panc-1 cells, 4.4 million THP-1 macrophages, and 8.8 million MeWo cells in a total bioink volume of 5 mL. The bioink was gently mixed to ensure homogeneous cell distribution while avoiding air bubble formation.

For bioprinting, the prepared bioink was loaded into sterile 3 mL cartridges and rested at room temperature for 15–20 minutes prior to printing. Extrusion-based bioprinting was performed using the BioX system with the following parameters, inspired by protocols described by Godier et al. (2024): nozzle gauge 23 G (0.66 mm), printhead temperature 37 °C, printbed temperature 8 °C, extrusion pressure 10–20 kPa, and printing speed 5–10 mm/s [15]. Printed constructs were deposited directly onto 24-well plates and crosslinked with 1 mL of 100 mM $CaCl_2$ solution for 10 minutes. After crosslinking, the $CaCl_2$ solution was removed and each construct was supplemented with 1 mL of complete culture medium before incubation at 37 °C in 5% CO_2 until further analyses. The complete bioprinting process, including cell harvesting, bioink preparation, printing, crosslinking,

and incubation, is illustrated in Figure 3.1, following the same schematic style as described by Godier et al. (2024) [15].

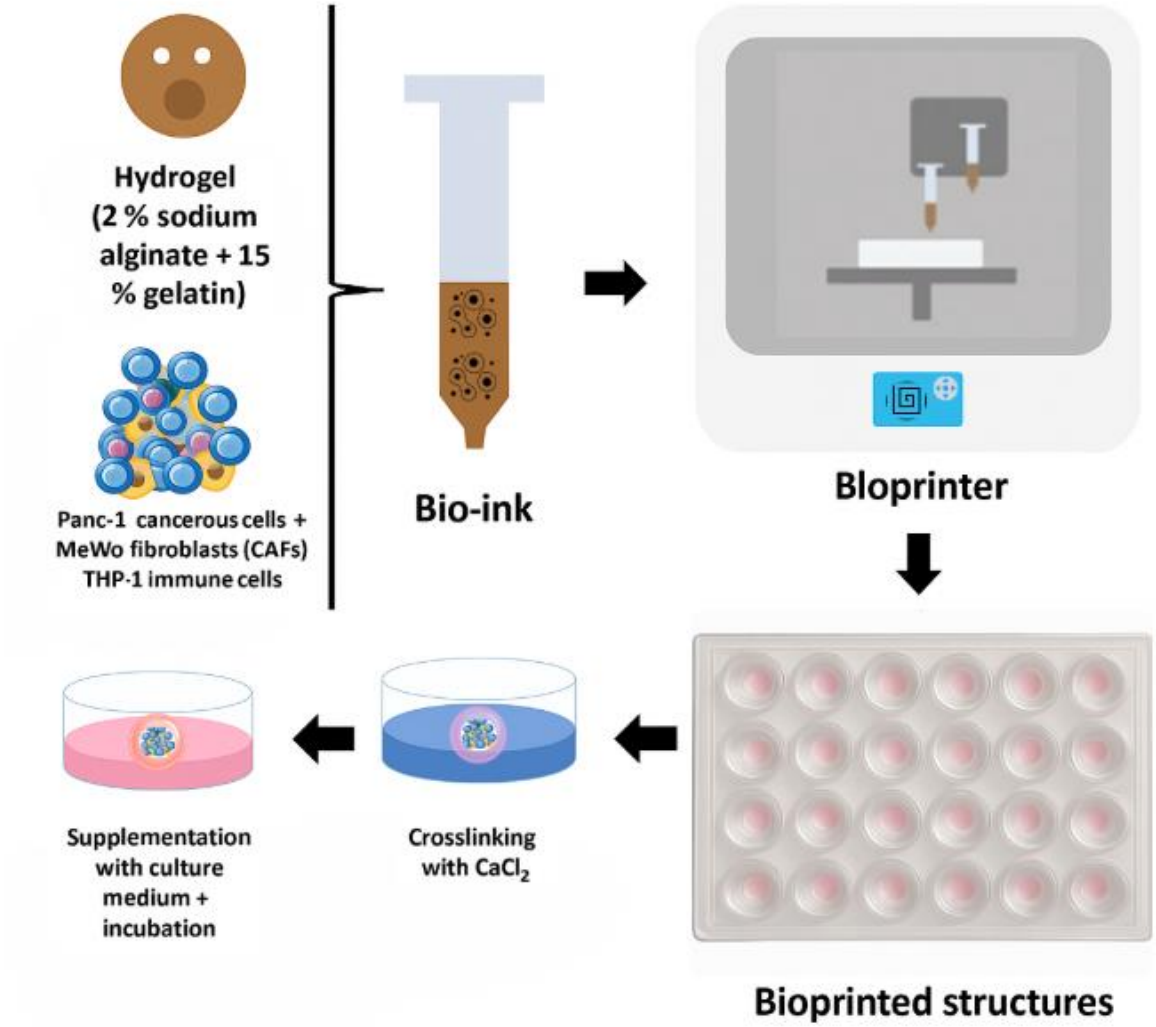

Figure 3.1. Schematic representation of the bioprinting process for the triculture tumor model. Cells were trypsinized and embedded in a 2% (w/v) sodium alginate + 15% (w/v) gelatin hydrogel to form the bioink. Cylindrical tumor constructs (6 mm diameter, 1.5 mm height) were then printed, crosslinked with 100 mM $CaCl_2$ for 10 minutes, supplemented with complete culture medium, and incubated at 37 °C in 5% CO_2 until further experiments.

3.2.6 Cell Viability Assay

Live/Dead Viability/Cytotoxicity assays were performed on the 3D bioprinted structures following the manufacturer's protocol (Thermo Fisher Scientific, Live/Dead Viability/Cytotoxicity Kit, Cat. No. L3224). After removal of the culture medium, each construct was washed with 1 mL of DPBS and incubated with a staining solution containing 1.6 µM calcein-AM and 12.8 µM ethidium homodimer-1 (EthD-1) in DPBS (400 µL per

sample) for 30 minutes at 37 °C, protected from light. Fluorescence imaging was performed using a Zeiss LSM 710 confocal microscope (Zeiss, Heidelberg, Germany) with appropriate filter settings summarized in Table 3.1.

Table 3.2. Parameters of Confocal Observation During the Live/Dead assay.

Reagent	Calcein	Ethidium Homo-Dimer 1
Excitation/emission wavelength [nm]	494/517	528/617
Standard set filter	Green channel: (Ex/EM = 488/520 nm)	Red channel: (Ex/EM = 561/596 nm)

Cell viability assays were carried out on days 1, 2, 3, 4, and 5 after printing to confirm the stability and structural integrity of the bioprinted constructs over a clinically relevant time frame. This five-day monitoring window was selected to align with cytotoxicity profiles of chemotherapies commonly used in pancreatic ductal adenocarcinoma, such as gemcitabine and FOLFIRINOX, which have demonstrated significant apoptotic or anti-proliferative effects in PDAC models within 48 to 120 h [16-18]. This ensures that the tumor model can sustain viability long enough for potential drug testing protocols. Image analysis and quantification of live (green) versus dead (red) cells were performed using the ImageJ 1.53c software package (NIH, USA).

3.3 Results and Discussion

3.3.1 THP-1 Differentiation Efficiency

Although the differentiation protocol using PMA applied to our study, THP-1 cell differentiation proved to be a relatively inefficient process. Across 10 replicates, PMA-induced differentiation yielded an average efficiency of only 20 ± 5% (mean ± SD). This relatively low yield may be attributed to intrinsic heterogeneity in the THP-1 cell line and variable responsiveness to PMA stimulation, as previously reported [19]. Additionally, the cell harvesting step posed technical challenges: while Accutase was initially employed for detachment, a significant proportion of differentiated THP-1 cells remained strongly adherent to the culture surface, potentially affecting their recovery and thus the final yield. Literature supports the use of mechanical cell scraping (e.g., rubber policeman) as an

alternative or complementary method to maximize the recovery of differentiated THP-1 macrophages, similarly to what is described for RAW 264.7 cells [20].

These technical factors may have contributed to the overall lower differentiation efficiency observed in our model. Although differentiation efficiency was modest, incorporating macrophages is an advantage compared to standard PDAC models, since immune components remain underrepresented [4]. Their presence likely enhanced tumor–stroma–immune interactions, as also suggested by the formation of cellular aggregates [15,16,18].

Figure 3.2 illustrates the total number of THP-1 cells (×10⁶) on the y-axis, alongside the corresponding proportion of M0-like macrophages achieved in each replicate.

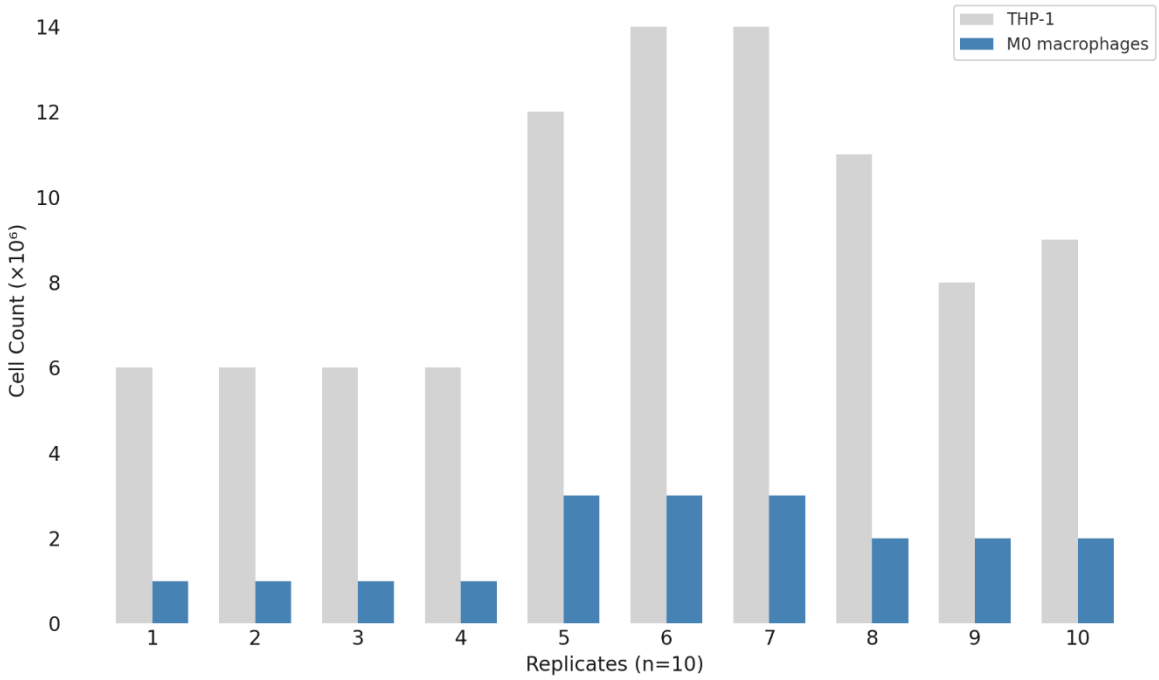

Figure 3.2. Percentage of THP-1 cells differentiated into M0-like macrophages after 48 h of PMA stimulation across 10 replicates (mean ± SD).

3.3.2 Bioprinting Performance

The bioprinting process (Figure 3.1) employed a total volume of 3 mL of bioink, sufficient to produce approximately 48 individual tumor constructs in about 4 h of processing. This workflow demonstrated high reproducibility and scalability, highlighting its cost-effectiveness when compared to organoid-based platforms. Each printed construct was designed as a cylinder measuring 6 mm in diameter and 1.5 mm in height,

corresponding to a volume of 62.5 µL of bioink per unit. The geometric design of the tumor model was generated using OneShape CAD software to ensure precision and reproducibility. The final bioink contained Panc-1, MeWo, and differentiated THP-1 cells at a ratio of 1:2:4, corresponding to a total cell density of 3×10^6 cells/mL, homogeneously dispersed within a gelatin–alginate hydrogel. However, the gelatin–alginate hydrogel showed moderate fragility during handling, a limitation previously reported for similar matrices [13]. Alternative reinforcement strategies may improve mechanical stability without compromising cell viability.

3.3.3 Cell Viability

Cell viability was assessed using the Live/Dead assay as described in section 2.6. Constructs were imaged by confocal microscopy, and viability was quantified with ImageJ based on the ratio of live (green) to dead (red) cells. Representative confocal images for days 1 through 5 and the quantitative viability data are shown in Figure 3, where an average viability of 73.4% was observed on day 1, followed by a decline to 62.4% on day 2, with slight recovery on day 3 (65.6%) and subsequent decreases on days 4 and 5 (60.6% and 57.2%, respectively). These viability patterns may be associated with the establishment of nutrient and oxygen gradients within the hydrogel constructs over time, as reported in previous studies with similar 3D bioprinted tumor models [21-23]. This observation highlights the importance of optimizing nutrient perfusion and construct geometry in future designs. Despite the progressive decline, viability remained above 50% over 5 days, which is consistent with the typical exposure windows of chemotherapeutics such as FOLFIRINOX and gemcitabine–nab-paclitaxel [24,25].

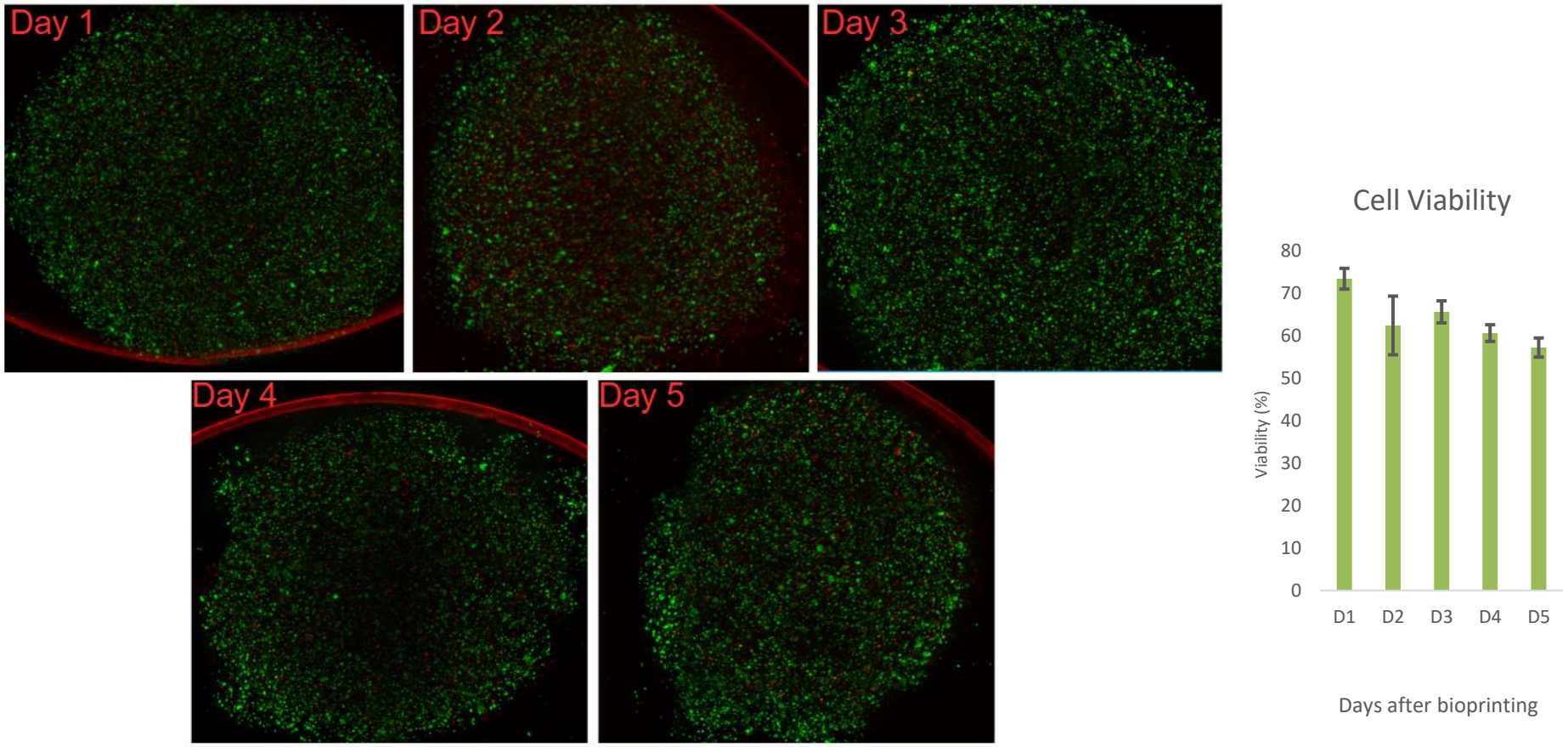

Figure 3. Representative Live/Dead confocal microscopy images of 3D bioprinted triculture constructs from day 1 to day 5 of culture (green: live cells; red: dead cells), alongside quantitative analysis of cell viability (%), presented as mean ± SD (n = 4)

3.4 CONCLUSION

This work demonstrates the feasibility of an accessible and reproducible 3D bioprinted PDAC model incorporating immune components, suitable for short-term applications. By enabling integration with organ-on-chip technologies, it offers a promising pathway to increase physiological relevance and to bridge the gap between in vitro experimentation and clinically relevant PDAC research.

3.5 REFERENCES

[1] J. Ushio *et al.*, "Pancreatic ductal adenocarcinoma: Epidemiology and risk factors," *Diagnostics*, vol. 11, no. 3, pp. 1–13, 2021, doi: 10.3390/diagnostics11030562.

[2] J. D. Mizrahi, R. Surana, J. W. Valle, and R. T. Shroff, "Pancreatic cancer," *The Lancet*, vol. 395, no. 10242, pp. 2008–2020, 2020, doi: 10.1016/S0140-6736(20)30974-0.

[3] L. Buscail, B. Bournet, and P. Cordelier, "Cancer of the pancreas," *Bull Acad Natl Med*, vol. 196, no. 9, pp. 1819–1828, 2012, doi: 10.1016/s0001-4079(19)31657-7.

[4] S. Upadhrasta and L. Zheng, "Strategies in developing immunotherapy for pancreatic cancer: Recognizing and correcting multiple immune 'defects' in the tumor microenvironment," *J Clin Med*, vol. 8, no. 9, pp. 1–10, 2019, doi: 10.3390/jcm8091472.

[5] D. P. Ryan, T. S. Hong, and N. Bardeesy, "Pancreatic Adenocarcinoma," pp. 1039–1049, 2014, doi: 10.1056/NEJMra1404198.

[6] M. Orth *et al.*, "Pancreatic ductal adenocarcinoma : biological hallmarks , current status , and future perspectives of combined modality treatment approaches," pp. 1–20, 2019.

[7] C. Feig, A. Gopinathan, A. Neesse, D. S. Chan, N. Cook, and D. A. Tuveson, "The Pancreas Cancer Microenvironment," vol. 18, no. 16, pp. 4266–4277, 2012, doi: 10.1158/1078-0432.CCR-11-3114.

[8] D. et al. HAKOBYAN, "Laser-assisted 3D bioprinting of exocrine pancreas spheroid models for cancer initiation study," *Mater Today Proc*, vol. 27, no. xxxx, pp. 0–31, 2019, [Online]. Available: https://doi.org/10.1016/j.matpr.2019.12.188%0Ahttps://doi.org/10.1016/j.matpr.2019.09.090%0Ahttps://doi.org/10.1080/14484846.2018.1432089

[9] C. Biosensors, R. Edmondson, J. J. Broglie, A. F. Adcock, and L. Yang, "Three-Dimensional Cell Culture Systems and Their Applications in Drug Discovery and Cell-Based Biosensors," vol. 12, no. 4, pp. 207–218, 2014, doi: 10.1089/adt.2014.573.

[10] R. Augustine *et al.*, "3D Bioprinted cancer models: Revolutionizing personalized cancer therapy," *Transl Oncol*, vol. 14, no. 4, 2021, doi: 10.1016/j.tranon.2021.101015.

[11] A. E. and S. F. D. P. Maddaly Ravi*, Paramesh V, Kaviya SR, "3D Cell Culture Systems - Advantages and Applications," no. May 2014, doi: 10.1002/jcp.24683.

[12] A. Fatehullah, S. H. Tan, and N. Barker, "Organoids as an in vitro model of human development and disease," *Nature Publishing Group*, vol. 18, no. 3, pp. 246–254, 2016, doi: 10.1038/ncb3312.

[13] B. Tan, S. Gan, X. Wang, W. Liu, and X. Li, "Applications of 3D bioprinting in tissue engineering: advantages, deficiencies, improvements, and future perspectives," *J Mater Chem B*, vol. 9, no. 27, pp. 5385–5413, 2021, doi: 10.1039/d1tb00172h.

[14] Z. Baka *et al.*, "A Coculture Based, 3D Bioprinted Ovarian Tumor Model Combining Cancer Cells and Cancer Associated Fibroblasts," *Macromol Biosci*, vol. 23, no. 3, pp. 1–13, 2023, doi: 10.1002/mabi.202200434.

[15] C. Godier *et al.*, "A 3D Bio-Printed-Based Model for Pancreatic Ductal Adenocarcinoma," pp. 1–19, 2024.

[16] E. L. and L. L. del M. * Anna Chiara Sicilianoa,b 1, Stefania Forcinitia 1, Valentina Onestoa, Helena Iuelea, Donatella Delle Cavec, Federica Carnevalia,b, Giuseppe Giglia,d, "A 3D pancreatic cancer model with integrated optical sensors for non-invasive metabolism monitoring and drug screening," vol. 2401138, pp. 1–22, 2024, doi: 10.1002/adhm.202401138.

[17] C. Panebianco *et al.*, "Improving Gemcitabine Sensitivity in Pancreatic Cancer Cells by Restoring miRNA-217 Levels," pp. 1–18, 2021.

[18] J. U. N. Yu, J. Drisko, and Q. I. Chen, "Inhibition of pancreatic cancer and potentiation of gemcitabine effects by the extract of Pao Pereira," pp. 149–156, 2013, doi: 10.3892/or.2013.2461.

[19] M. Daigneault, J. A. Preston, H. M. Marriott, M. K. B. Whyte, and D. H. Dockrell, "The Identification of Markers of Macrophage Differentiation in PMA-Stimulated THP-1 Cells and," vol. 5, no. 1, 2010, doi: 10.1371/journal.pone.0008668.

[20] B. Taciak *et al.*, “Evaluation of phenotypic and functional stability of RAW 264 . 7 cell line through serial passages,” pp. 1–13, 2018.

[21] A. Persaud, A. Maus, L. Strait, and D. Zhu, “3D Bioprinting with Live Cells,” *Engineered Regeneration*, vol. 3, no. 3, pp. 292–309, 2022, doi: 10.1016/j.engreg.2022.07.002.

[22] S. Hong and J. M. Song, “3D bioprinted drug-resistant breast cancer spheroids for quantitative in situ evaluation of drug resistance,” *Acta Biomater*, vol. 138, pp. 228–239, 2022, doi: 10.1016/j.actbio.2021.10.031.

[23] P. Sokolowska, K. Zukowski, J. Janikiewicz, E. Jastrzebska, A. Dobrzyn, and Z. Brzozka, “Islet-on-a-chip: Biomimetic micropillar-based microfluidic system for three-dimensional pancreatic islet cell culture,” *Biosens Bioelectron*, vol. 183, no. April, p. 113215, 2021, doi: 10.1016/j.bios.2021.113215.

[24] T. Jiang, J. G. Munguia-Lopez, S. Flores-Torres, J. Kort-Mascort, and J. M. Kinsella, “Extrusion bioprinting of soft materials: An emerging technique for biological model fabrication,” *Appl Phys Rev*, vol. 6, no. 1, 2019, doi: 10.1063/1.5059393.

[25] I. T. Ozbolat and M. Hospodiuk, “Current advances and future perspectives in extrusion-based bioprinting,” *Biomaterials*, vol. 76, pp. 321–343, 2016, doi: 10.1016/j.biomaterials.2015.10.076.

4 PERSPECTIVES FOR TRANSLATIONAL INTEGRATION: FROM TUMOR MODELS TO CHRONIC INFLAMMATORY WOUNDS

The studies presented in this dissertation address distinct but converging challenges in biomedical research: modeling the tumor microenvironment and modulating chronic inflammation in non-healing wounds. In both pancreatic ductal adenocarcinoma (PDAC) and diabetic foot ulcers (DFUs), dysregulated immune responses, arising from complex interactions between stromal, epithelial, and immune cells, drive disease progression.

From a translational perspective, the two approaches developed here —the 3D bioprinted PDAC model and the nanoemulsion-based anti-inflammatory strategy —offer complementary tools for studying and intervening in inflammation-driven pathologies. The tumor constructs reproduced a heterocellular PDAC niche with potential for integration into organ-on-a-chip (OoC) systems, while the curcumin- and annatto-based nanoemulsions, under blue LED irradiation, demonstrated partial modulation of nitric oxide production, providing a foundation for future immunomodulatory therapies in chronic wounds.

This convergence aligns with emerging efforts to establish DFU-on-a-chip platforms. Ejiugwo et al. (2021) emphasize the integration of disease-derived cells, immune elements, and microfluidic scaffolds to create physiologically relevant drug-testing environments [42]. Looking forward, the modularity of bioprinting and nanobiotechnology could enable unified microfluidic platforms bridging cancer and wound models, advancing personalized therapy development while reducing reliance on animal experimentation.

Limitations remain in both approaches. The structural fragility of tumor constructs highlights the need for optimized bioinks, with potential alternatives summarized in Table 6.1. Likewise, the selective nitric oxide modulation by nanoemulsions points to the importance of broadening immunological endpoints—such as cytokine panels and macrophage polarization assays—to clarify therapeutic mechanisms.

Together, these findings underscore the potential of integrating 3D bioprinting and photoresponsive nanotechnologies into next-generation OoC platforms. By enabling the study of inflammation-driven mechanisms across distinct diseases, such systems may accelerate

translational research and foster targeted therapies for pathologies characterized by persistent inflammation.

5 CONCLUSION

This dissertation presented two complementary strategies: a 3D bioprinted PDAC model and photoactivated nanoemulsions for chronic inflammation. The tumor model successfully recreated a heterocellular microenvironment with potential for integration into organ-on-a-chip systems.

The nanoformulations demonstrated biocompatibility and significant immunomodulatory effects in activated macrophages, including nitric oxide suppression and, under blue light, increased IL-10 release and reduced TNF-α levels.

Together, these approaches exemplify how advanced modeling an nanobiotechnological interventions could converge to address unresolved clinical challenges. By bridging fundamental mechanisms and therapeutic innovation, this work outlines a translational path with potential applications in both oncology and chronic wound management.

6 REFERENCES

[1] A. M. Brokowski C, "Organ-on-a-Chip: A new paradigm for drug development," *Physiol Behav*, vol. 176, no. 5, pp. 139–148, 2019, doi: 10.1016/j.tips.2020.11.009.Organ-on-a-Chip.

[2] J. Saji Joseph, S. Tebogo Malindisa, and M. Ntwasa, "Two-Dimensional (2D) and Three-Dimensional (3D) Cell Culturing in Drug Discovery," *Cell Culture*, 2019, doi: 10.5772/intechopen.81552.

[3] D. Cook *et al.*, "Lessons learned from the fate of AstraZeneca's drug pipeline: A five-dimensional framework," *Nat Rev Drug Discov*, vol. 13, no. 6, pp. 419–431, 2014, doi: 10.1038/nrd4309.

[4] K. Fetah *et al.*, "The emergence of 3D bioprinting in organ-on-chip systems," *Progress in Biomedical Engineering*, vol. 1, no. 1, 2019, doi: 10.1088/2516-1091/ab23df.

[5] A. Abbott, “Biology’s new dimension,” *Nature*, vol. 424, no. 6951, pp. 870–872, 2003, doi: 10.1038/424870a.

[6] J. C. Fontoura *et al.*, “Comparison of 2D and 3D cell culture models for cell growth, gene expression and drug resistance,” *Materials Science and Engineering C*, vol. 107, no. September 2019, p. 110264, 2020, doi: 10.1016/j.msec.2019.110264.

[7] R. Edmondson, J. J. Broglie, A. F. Adcock, and L. Yang, “Three-dimensional cell culture systems and their applications in drug discovery and cell-based biosensors,” *Assay Drug Dev Technol*, vol. 12, no. 4, pp. 207–218, 2014, doi: 10.1089/adt.2014.573.

[8] S. Breslin and L. O’Driscoll, “Three-dimensional cell culture: The missing link in drug discovery,” *Drug Discov Today*, vol. 18, no. 5–6, pp. 240–249, 2013, doi: 10.1016/j.drudis.2012.10.003.

[9] B. M. Baker and C. S. Chen, “Deconstructing the third dimension-how 3D culture microenvironments alter cellular cues,” *J Cell Sci*, vol. 125, no. 13, pp. 3015–3024, 2012, doi: 10.1242/jcs.079509.

[10] M. W. Dewhirst, Y. Cao, and B. Moeller, “Cycling hypoxia and free radicals regulate angiogenesis and radiotherapy response,” *Nat Rev Cancer*, vol. 8, no. 6, pp. 425–437, 2008, doi: 10.1038/nrc2397.

[11] S. Abizanda-Campo *et al.*, “Microphysiological systems for solid tumor immunotherapy: opportunities and challenges,” *Microsyst Nanoeng*, vol. 9, no. 1, 2023, doi: 10.1038/s41378-023-00616-x.

[12] F. Pampaloni, E. G. Reynaud, and E. H. K. Stelzer, “The third dimension bridges the gap between cell culture and live tissue,” *Nature Review - Molecular Cell Biology*, vol. 8, no. october, pp. 839–845, 2007, [Online]. Available: www.nature.com/reviews/molcellbio

[13] E. M. Tosca, D. Ronchi, D. Facciolo, and P. Magni, “Replacement, Reduction, and Refinement of Animal Experiments in Anticancer Drug Development: The Contribution of 3D In Vitro Cancer Models in the Drug Efficacy Assessment,” *Biomedicines*, vol. 11, no. 4, 2023, doi: 10.3390/biomedicines11041058.

[14] G. A. Van Norman, “Limitations of Animal Studies for Predicting Toxicity in Clinical Trials: Is it Time to Rethink Our Current Approach?,” *JACC Basic Transl Sci*, vol. 4, no. 7, pp. 845–854, 2019, doi: 10.1016/j.jacbts.2019.10.008.

[15] S. A. Langhans, “Three-dimensional in vitro cell culture models in drug discovery and drug repositioning,” *Front Pharmacol*, vol. 9, no. JAN, pp. 1–14, 2018, doi: 10.3389/fphar.2018.00006.

[16] A. Gomes, L. Guillaume, D. R. Grimes, J. Fehrenbach, V. Lobjois, and B. Ducommun, “Oxygen partial pressure is a rate-limiting parameter for cell proliferation in 3D spheroids grown in physioxic culture condition,” *PLoS One*, vol. 11, no. 8, pp. 1–11, 2016, doi: 10.1371/journal.pone.0161239.

[17] D. van den Brand, C. Veelken, L. Massuger, and R. Brock, “Penetration in 3D tumor spheroids and explants: Adding a further dimension to the structure-activity relationship of cell-penetrating peptides,” *Biochim Biophys Acta Biomembr*, vol. 1860, no. 6, pp. 1342–1349, 2018, doi: 10.1016/j.bbamem.2018.03.007.

[18] P. A. J. Sant, Shilpa, S. Sant, and P. A. Johnston, “The Production of 3D Tumor Spheroids for Cancer Drug Discovery - HHS Public Access,” *Physiol Behav*, vol. 176, no. 1, pp. 139–148, 2017, doi: 10.1016/j.ddtec.2017.03.002.The.

[19] L. B. Weiswald, D. Bellet, and V. Dangles-Marie, “Spherical Cancer Models in Tumor Biology,” *Neoplasia (United States)*, vol. 17, no. 1, pp. 1–15, 2015, doi: 10.1016/j.neo.2014.12.004.

[20] X. Zhuang *et al.*, “Recent advances of three-dimensional bioprinting technology in hepato-pancreato-biliary cancer models,” *Front Oncol*, vol. 13, no. April, pp. 1–13, 2023, doi: 10.3389/fonc.2023.1143600.

[21] M. Kim, D. G. Hwang, and J. Jang, “3D Pancreatic Tissue Modeling in vitro: Advances and Prospects,” *Biochip J*, vol. 14, no. 1, pp. 84–99, 2020, doi: 10.1007/s13206-020-4108-4.

[22] Y. Nanki *et al.*, “Patient-derived ovarian cancer organoids capture the genomic profiles of primary tumours applicable for drug sensitivity and resistance testing,” *Sci Rep*, vol. 10, no. 1, pp. 1–11, 2020, doi: 10.1038/s41598-020-69488-9.

[23] Y. Dong, X. Zhou, Y. Ding, Y. Luo, and H. Zhao, “Advances in tumor microenvironment: Applications and challenges of 3D bioprinting,” *Biochem Biophys Res Commun*, vol. 730, no. January, p. 150339, 2024, doi: 10.1016/j.bbrc.2024.150339.

[24] B. X. Wu *et al.*, “Application of three-dimensional (3D) bioprinting in anti-cancer therapy,” *Heliyon*, vol. 9, no. 10, p. e20475, 2023, doi: 10.1016/j.heliyon.2023.e20475.

[25] L. Fang, Y. Liu, J. Qiu, and W. Wan, “Bioprinting and its Use in Tumor-On-A-Chip Technology for Cancer Drug Screening: A Review,” *Int J Bioprint*, vol. 8, no. 4, pp. 46–64, 2022, doi: 10.18063/ijb.v8i4.603.

[26] E. K. Sackmann, A. L. Fulton, and D. J. Beebe, “The present and future role of microfluidics in biomedical research,” *Nature*, vol. 507, no. 7491, pp. 181–189, 2014, doi: 10.1038/nature13118.

[27] S. David, R. Walt, J. Stubbs, H. Andersson-svahn, M. Gilligan, and E. Wilson, “Lab on a Chip Lab on a Chip,” *Lab Chip*, no. 207890, pp. 1037–1043, 2014, [Online]. Available: http://dx.doi.org/10.1039/C4LC00803K

[28] P. Hyochol Ahn, PhD, Michael Weaver, PhD, Debra Lyon, PhD, Eunyoung Choi, RN, and Roger B. Fillingim, “The upcoming 3D-printing revolution in microfluidics HHS Public Access,” *Physiol Behav*, vol. 176, no. 10, pp. 139–148, 2017, doi: 10.1039/c6lc00163g.The.

[29] J. D. Mizrahi, R. Surana, J. W. Valle, and R. T. Shroff, “Pancreatic cancer,” *The Lancet*, vol. 395, no. 10242, pp. 2008–2020, 2020, doi: 10.1016/S0140-6736(20)30974-0.

[30] L. I. F. Moura, A. M. A. Dias, E. Carvalho, and H. C. De Sousa, “Recent advances on the development of wound dressings for diabetic foot ulcer treatment - A review,” *Acta Biomater*, vol. 9, no. 7, pp. 7093–7114, 2013, doi: 10.1016/j.actbio.2013.03.033.

[31] J. L. Burgess, W. A. Wyant, B. A. Abujamra, R. S. Kirsner, and I. Jozic, “Diabetic Wound-Healing Science,” 2021.

[32] S. Upadhrasta and L. Zheng, “Strategies in developing immunotherapy for pancreatic cancer: Recognizing and correcting multiple immune ‘defects’ in the tumor microenvironment,” *J Clin Med*, vol. 8, no. 9, pp. 1–10, 2019, doi: 10.3390/jcm8091472.

[33] C. Godier *et al.*, “A 3D Bio-Printed-Based Model for Pancreatic Ductal Adenocarcinoma,” pp. 1–19, 2024.

[34] E. Tsourdi, A. Barthel, H. Rietzsch, A. Reichel, and S. R. Bornstein, “Current aspects in the pathophysiology and treatment of chronic wounds in diabetes mellitus,” 2013. doi: 10.1155/2013/385641.

[35] L. Deng *et al.*, “The Role of Oxidative Stress and Antioxidants in Diabetic Wound Healing,” vol. 2021, no. Figure 1, 2021.

[36] J. Ushio *et al.*, “Pancreatic ductal adenocarcinoma: Epidemiology and risk factors,” *Diagnostics*, vol. 11, no. 3, pp. 1–13, 2021, doi: 10.3390/diagnostics11030562.

[37] V. Rebours *et al.*, “Obesity and fatty pancreatic infiltration are risk factors for pancreatic precancerous lesions (PanIN),” no. 4.

[38] R. Augustine *et al.*, “3D Bioprinted cancer models: Revolutionizing personalized cancer therapy,” *Transl Oncol*, vol. 14, no. 4, 2021, doi: 10.1016/j.tranon.2021.101015.

[39] K. F. Rezende *et al.*, “Predicted annual costs for inpatients with diabetes and foot ulcers in a developing country — a simulation of the current situation in Brazil,” pp. 109–112, 2010, doi: 10.1111/j.1464-5491.2009.02871.x.

[40] C. M. Toscano, T. H. Sugita, M. Q. M. Rosa, H. C. Pedrosa, R. dos S. Rosa, and L. R. Bahia, “Annual direct medical costs of diabetic foot disease in brazil: A cost of illness study,” *Int J Environ Res Public Health*, vol. 15, no. 1, Jan. 2018, doi: 10.3390/ijerph15010089.

[41] S. A. Eming, T. Krieg, and J. M. Davidson, “Inflammation in wound repair: Molecular and cellular mechanisms,” *Journal of Investigative Dermatology*, vol. 127, no. 3, pp. 514–525, 2007, doi: 10.1038/sj.jid.5700701.

[42] M. Ejiugwo, Y. Rochev, G. Gethin, and G. O’Connor, “Toward Developing Immunocompetent Diabetic Foot Ulcer-on-a-Chip Models for Drug Testing,” *Tissue Eng Part C Methods*, vol. 27, no. 2, pp. 77–88, 2021, doi: 10.1089/ten.tec.2020.0331.

[43] W. R. Inch, J. A. Credie, and R. M. Sutherland, “Growth of nodular carcinomas in rodents compared with multi-cell spheroids in tissue culture.,” 1970.

[44] Y. Ju *et al.*, “Barriers and opportunities in pancreatic cancer immunotherapy,” *NPJ Precis Oncol*, vol. 8, no. 1, pp. 1–18, 2024, doi: 10.1038/s41698-024-00681-z.

[45] A. Bulle and K. H. Lim, “Beyond just a tight fortress: contribution of stroma to epithelial-mesenchymal transition in pancreatic cancer,” *Signal Transduct Target Ther*, vol. 5, no. 1, 2020, doi: 10.1038/s41392-020-00341-1.

[46] T. Angela Maria Vicente, *Estratégias para o cuidado da pessoa com doença crônica: diabetes mellitus*, vol. 11, no. 1. 2013. [Online]. Available: http://scioteca.caf.com/bitstream/handle/123456789/1091/RED2017-Eng-8ene.pdf?sequence=12&isAllowed=y%0Ahttp://dx.doi.org/10.1016/j.regsciurbeco.2008.06.005%0Ahttps://www.researchgate.net/publication/305320484_SISTEM_PEMBETUNGAN_TERPUSAT_STRATEGI_MELESTARI

[47] C. Fajardo, “A importância do cuidado com o pé diabético: ações de prevenção e abordagem clínica,” *Revista Brasileira de Medicina de Família e Comunidade*, vol. 2, no. 5, pp. 43–58, 2006, doi: 10.5712/rbmfc2(5)25.

[48] P. L. N. da Silva *et al.*, “Importância da comissão de curativos no tratamento das lesões cutâneas: um relato de experiência,” *Revista Eletrônica Acervo Saúde/ Electronic Journal Collection Health*, pp. 310–315, 2017.

[49] T. F. Cestari, S. Pessato, and G. P. Corrêa, “Fototerapia: aplicações clínicas,” *An Bras Dermatol*, vol. 82, no. 1, pp. 7–21, 2007, doi: 10.1590/s0365-05962007000100002.

[50] J.-H. Lee, S.-J. Jekal, and P.-S. Kwon, “630 nm Light Emitting Diode Irradiation Improves Dermal Wound Healing in Rats,” vol. 27, no. 3, pp. 140–146, 2015.

[51] P. Sokolowska, A. Zuchowska, and Z. Brzozka, “Why Can Organoids Improve Current Organ-on-Chip Platforms?,” *Organoids*, vol. 1, no. 1, pp. 69–84, 2022, doi: 10.3390/organoids1010007.

[52] D. Szűcs *et al.*, “Toward better drug development: Three-dimensional bioprinting in toxicological research,” *Int J Bioprint*, vol. 9, no. 2, pp. 197–218, 2022, doi: 10.18063/IJB.V9I2.663.

[53] A. Dellaquila, C. Le Bao, D. Letourneur, and T. Simon-Yarza, “In Vitro Strategies to Vascularize 3D Physiologically Relevant Models,” *Advanced Science*, vol. 8, no. 19, 2021, doi: 10.1002/advs.202100798.

[54] A. Persaud, A. Maus, L. Strait, and D. Zhu, “3D Bioprinting with Live Cells,” *Engineered Regeneration*, vol. 3, no. 3, pp. 292–309, 2022, doi: 10.1016/j.engreg.2022.07.002.

[55] T. Fernandes Santana Gomes *et al.*, “A Natural Latex-Based Smart Dressing for Curcumin Delivery Combined with LED Phototherapy in Diabetic Foot Ulcers: A Pilot Clinical Study,” *Pharmaceutics*, vol. 17, p. 772, 2025, doi: 10.3390/pharmaceutics17060772.

[56] K. Berthelot, S. Lecomte, Y. Estevez, and F. Peruch, “Hevea brasiliensis REF (Hev b 1) and SRPP (Hev b 3): An overview on rubber particle proteins,” *Biochimie*, vol. 106, pp. 1–9, 2014, doi: 10.1016/j.biochi.2014.07.002.

[57] S. S. R. F. Rosa *et al.*, “Regeneration of Diabetic Foot Ulcers Based on Therapy with Red LED Light and a Natural Latex Biomembrane,” *Ann Biomed Eng*, vol. 47, no. 4, pp. 1153–1164, 2019, doi: 10.1007/s10439-019-02220-5.

[58] A. López-Delis *et al.*, “Characterization of the Cicatrization Process in Diabetic Foot Ulcers Based on the Production of Reactive Oxygen Species,” *J Diabetes Res*, vol. 2018, no. Dm, 2018, doi: 10.1155/2018/4641364.

[59] M. F. F. Rosa, S. M. F. Guimarães, A. G. Dominguez, Duarte, R. S. Assis, C. B. Reis, and S. de S. R. F. Rosa, "Desenvolvimento de tecnologia dura para tratamento do pé diabético: um estudo de caso na perspectiva da saúde coletiva," pp. 87–100, 2019, doi: 10.1590/0103-11042019S207.

[60] S. Rodrigues *et al.*, "a Tecnologia Rapha E Sua Incorporação No Sistema Único De Saúde-Sus : Inovação De Baixo," 2018.

[61] F. M. Silva *et al.*, "Curcumin and Papain-Loaded Liposomal Natural Latex Dressings with Phototherapy : A Synergistic Approach to Diabetic Wound Healing," no. Dm, pp. 1–21, 2025.

[62] W. Punfa, S. Yodkeeree, P. Pitchakarn, C. Ampasavate, and P. Limtrakul, "Enhancement of cellular uptake and cytotoxicity of curcumin-loaded PLGA nanoparticles by conjugation with anti-P-glycoprotein in drug resistance cancer cells," *Acta Pharmacol Sin*, vol. 33, no. 6, pp. 823–831, 2012, doi: 10.1038/aps.2012.34.

[63] N. Somchit *et al.*, "Curcumin pyrazole blocks lipopolysaccharide-induced inflammation via suppression of JNK activation in RAW 264.7 macrophages," *Asian Pac J Allergy Immunol*, vol. 36, no. 3, pp. 184–190, 2018, doi: 10.12932/AP-130417-0073.

[64] A. Venugopalan and P. Giridhar, "Bacterial growth inhibition potential of annatto plant parts," *Asian Pac J Trop Biomed*, vol. 2, no. 3 SUPPL., pp. S1879–S1882, 2012, doi: 10.1016/S2221-1691(12)60513-9.

[65] D. Coelho dos Santos, A. da Silva Barboza, J. S. Ribeiro, S. A. Rodrigues Junior, Â. D. Campos, and R. G. Lund, "Bixa orellana L. (Achiote, Annatto) as an antimicrobial agent: A scoping review of its efficiency and technological prospecting," *J Ethnopharmacol*, vol. 287, no. December 2021, 2022, doi: 10.1016/j.jep.2021.114961.

[66] S. O. Capella *et al.*, "Potencial cicatricial da Bixa orellana L. em feridas cutâneas: Estudo em modelo experimental," *Arq Bras Med Vet Zootec*, vol. 68, no. 1, pp. 104–112, 2016, doi: 10.1590/1678-4162-8374.

[67] L. Wu *et al.*, "Research progress of 3D-bioprinted functional pancreas and in vitro tumor models," *Int J Bioprint*, vol. 10, no. 1, pp. 124–142, 2023, doi: 10.36922/ijb.1256.